GEOPHYSICAL AND REMOTE SENSING STUDY OF TERRESTRIAL PLANETS

A Dissertation
Presented to
The Academic Faculty

By

Lujendra Ojha

In Partial Fulfillment
Of the Requirements for the Degree
Doctor of Philosophy in Earth and Atmospheric Sciences

Georgia Institute of Technology

August, 2016

GEOPHYSICAL AND REMOTE SENSING STUDY OF TERRESTRIAL PLANETS

Approved by:

Dr. James Wray, Advisor
School of Earth and Atmospheric Sciences
Georgia Institute of Technology

Dr. Joseph Dufek
School of Earth and Atmospheric Sciences
Georgia Institute of Technology

Dr. Britney Schmidt
School of Earth and Atmospheric Sciences
Georgia Institute of Technology

Dr. Ken Ferrier
School of Earth and Atmospheric Sciences
Georgia Institute of Technology

Dr. Suzanne Smrekar
Jet Propulsion laboratory
California Institute of Technology

Date Approved: June 27th, 2016.

To Rama, Tank, Jaika, Manjesh, Reeyan, and Kali.

ACKNOWLEDGEMENTS

Thanks Mom, Dad and Jaika for putting up with me and always being there. Thank you Kali for being such an awesome girl and being there when I needed you. Kali, you are the most beautiful girl in the world. Never forget that! Thanks Midtown Tavern for the hangovers. Thanks Waffle House for curing my hangovers. Thanks Sarah Sutton for guiding me into planetary science. Thanks Alfred McEwen for the continued support and mentoring since 2008. Thanks Sue Smrekar for taking me under your wings and teaching me about planetary geodynamics. Thanks Dan Nunes for guiding me in the gravity world. Thanks Ken Ferrier for helping me study my favorite planet. Thanks Scott Murchie for helping me become a better scientist. Thanks Marion Masse for being such a good friend and a mentor. Thank you HiRISE operations; no other mission will ever be as organized and efficient. Thank you CRISM operation team for providing such an incredible data set. Thank you NASA and NSF for continually supporting my scientific endeavors. I could not have done it without you. Thank you Britney Schmidt for always being there when needed. Thank you Ryan Cahalan and Lucas Liuzzo for the good times. Thank you George McDonald for being such an awesome lab mate and for introducing me to the world of board games. Thanks MB for the good times. Thank you my friends from MegaRock, Vipera and Gorkha band for some of the best times I had on this planet. Dudes, I couldn't have asked for better friends. Thank you EAS/GATech for letting me do my research with complete freedom. Last but not the least, thank you James Wray for everything you did. I wouldn't be in this position without you. Keep smiling, James!

This dissertation contains parts from two published manuscripts, two submitted manuscripts, and one manuscript in preparation:

1. Ojha, Lujendra, Mary Beth Wilhelm, Scott L. Murchie, Alfred S. McEwen, James J. Wray, Jennifer Hanley, Marion Massé, and Matt Chojnacki. "Spectral evidence for hydrated salts in recurring slope lineae on Mars." *Nature Geoscience* 8, no. 11 (2015): 829-832.
2. Ojha, Lujendra, James J. Wray, Scott L. Murchie, Alfred S. McEwen, Michael J. Wolff, and Suniti Karunatillake. "Spectral constraints on the formation mechanism of recurring slope lineae." *Geophysical Research Letters* 40, no. 21 (2013): 5621-5626.
3. Ojha, Lujendra, Suzanne E. Smrekar, and Daniel Nunes. "Geophysical Characterization of Elysium Planitia: Implications for the InSight mission." *Submitted to…*
4. Ojha, Lujendra, Scott L. Murchie, Marion Massé, Alfred S. McEwen, Colin Dundas, James J. Wray, Mary Beth Wilhelm, Jennifer Hanley. "Oxychlorine salts in the northern mid-latitudes of Mars: Implications for ice stability and habitability." *Submitted* (6/2016).
5. Ojha, Lujendra, Matt Chojnacki, Anthony Toigo, George McDonald, Timothy McConnochie, Scott Murchie, Alfred McEwen, Ken Ferrier, Christian Huber, James J. Wray. "Substantial surface erosion due to contemporary water activity on Mars." *In prep*

TABLE OF CONTENTS

PAGE

LIST OF TABLES

LIST OF FIGURES

SUMMARY

The overarching theme of this dissertation is the study of the evolution of terrestrial planets and its effect on surface processes and planetary habitability. In many regards, planetary habitability is an enthralling yet obscure topic because our understanding is limited by our terrestrial experience. The utmost necessity for habitability, based on terrestrial experience and general chemical principles, is water. The dissertation provides key spectroscopic evidence for contemporary liquid water on Mars. Pure water is highly unstable on Mars, so any water on the surface would likely be salty. The spectral data from Mars further provides evidence for hygroscopic salts called perchlorates that may be aiding in the formation of these present day brine streaks on Mars. Similar hygroscopic salts are found elsewhere on Mars; in every instance their presence occurs near known ice deposits, ancient sedimentary rocks or modern day brines. The important role of these hygroscopic salts in the present and past Martian water cycle and on habitability is discussed. Change is an inevitable part of natural processes, and nowhere is it manifested more exuberantly than in planetary landscapes. Planets evolve, and the corroboration of change is evident in surface features. An effort to understand the evolution of terrestrial planets in our own solar system, to better understand the formation and evolution of terrestrial planets elsewhere in the universe, is the second central theme of the dissertation. Specifically, by using the gravity data from the orbiters, a series of predictions about the InSight landing site is made. These predictions will test the validity of various methodologies and help constrain the radiogenic content of the Martian crust. In the long term, the measurements from InSight will help answer the evolutionary course Mars took, and what effect higher heat flow

during the early stage of its history may have had on the loss of liquid water from the surface.

CHAPTER 1

INTRODUCTION

1.1. FORMATION AND STABILITY OF WATER IN THE SOLAR SYSTEM

One of the simplest definitions of life is, "*a structure capable of auto-reproduction including errors that lead to evolution*" (*Brack,* 2006). As we understand it, the basic requirements for origin and proliferation of life are: (i) source(s) of energy, (ii) carbon, phosphorus, hydrogen, oxygen, nitrogen, sulfur (CPHONS), (iii) magnetic field for protection against the cosmic radiation and (iv) a liquid-medium that facilitates diffusion of nutrients in a cell and provides a pathway for diffusion of waste materials. Rocky planets can provide excellent sources of energy, whereby "life" can acquire energy from any geological process that has a net-negative Gibbs free energy. Carbon molecules and PHONS are ubiquitous in the universe and are frequently delivered to rocky planets by extraterrestrial sources (*Brown et al.,* 2000). In fact, eight of the amino acids that are used in living cells today have been identified in carbonaceous chondrites (*Southam et al.,* 2015). Although Mercury and Earth are the only planets to possess a magnetic field currently, both Mars and Venus show evidence for an intrinsic magnetic field in their early history (e.g. Connerney et al., 2001; *Stevenson et al.,* 1983). The chemical composition and stability of a liquid medium on a planet are dependent on the planet's position around the central star and its internal heat. Based on terrestrial experience and general chemical principles, water is seen as an excellent liquid medium for diffusion of nutrients and waste (e.g. *Pohorille,* 2008).

The combination of the most common element in the universe, hydrogen (H), and the third most common element, oxygen (O), results in the formation of one of the most

abundant molecules in our solar system: water ($H_2 + \frac{1}{2} O2 \leftrightharpoons H_2O$ + energy). Oxygen has 6 electrons in its outermost shell, so it covalently bonds with two hydrogen and shares a pair of electrons. The force exerted by the two lone pairs exerts a repulsive force on the bonding hydrogen atoms, which is the reason for their slightly bent (104°) molecular shape. This uneven distribution of electron density makes water a polar molecule, where a slight negative charge is present near the oxygen atoms due to the unshared pair of electrons, and slight positive charge present near the hydrogen atoms. This polarity is also the reason why many ions and molecules can easily dissolve in water, and why water plays a huge role in various geological, chemical and biological processes.

Water has a Gibbs free energy of -237.13kJ.mol^{-1}, which means it requires ~237kJ to form ~18 grams of water. As to when and where ices formed in the solar system remains an open question; water-ice could have formed in the cold molecular cloud of the interstellar medium before the sun's formation (e.g. *Cleeves et al.,* 2014), or through various reactions within the solar nebula. Regardless of the formation mechanism, the region at or beyond where water-ice can condense is called the *snowline*. Thermodynamically, water ice condenses when the partial pressure of water exceeds the saturation vapor pressure. A temperature range of 160-170 K is necessary for water-ice condensation, and depending on the age of the parent star, the distance to this snowline can vary between 1 to 5 AU (*Lunine,* 2006; *Sasselov and Lecar,* 2000). Since all terrestrial planets formed by collisions among planetesimals in the solar nebula, it is possible that some of the volatile inventory (including water) may have been acquired during this early period of planetary formation. However, *Lewis* (1972) asserted that the temperature in the planetary disk at less than 1 AU would have been too high for mineral hydration or ice

condensation. This rules out the acquisition of the primordial nebular water by planets like Mercury and Venus. In fact, *Prinn and Fegley* (1989) state that the gas-solid reactions are infeasible at typical nebular temperatures, concluding neither of the terrestrial planets' inventory of water could be explained this way. It is, however, possible that some of the water could have been deposited during the late stages of nebular evolution as the gas temperature plummeted (*Lunine,* 2006).

The physical state of water in a planet is controlled by the combination of the effective temperature and other internal sources of heat the planet may possess. Water is stable in liquid, gas and solid form in a wide range of temperature and pressure conditions (Figure 1.1). The **sublimation line** is the boundary that separates the solid and gas phase of water. As a function of temperature, the line indicates the vapor pressure of ice required for transformation into vapor and vice versa. The **saturation line** separates the liquid and vapor phase of water. The **critical point** on the saturation line occurs at ~640 K, and it marks the temperature above which, irrespective of the pressure, water cannot be liquefied. The **melting curve** marks the boundary between the solid and liquid phase of water, and has a negative slope, which means that melting occurs at lower temperatures as pressure increases. The **triple point** marks the point in which all three phases of water can coexist at equilibrium.

In the case of the solar system, temperature conducive to the formation of liquid water on a planetary surface lies between 0.95 to 1.37 AU (*Kasting et al.,* 1993). This is assuming that the planet has no other source of internal heating. Besides Earth, Mars is the only other planet in the solar system where water can exist in the liquid form, albeit transiently (Figure 1.1). Water does exist in the liquid form on the sub-surface of icy

moons, where a higher temperature is provided by the internal heating. Additionally, pressure plays a huge role in the stability of liquid water.

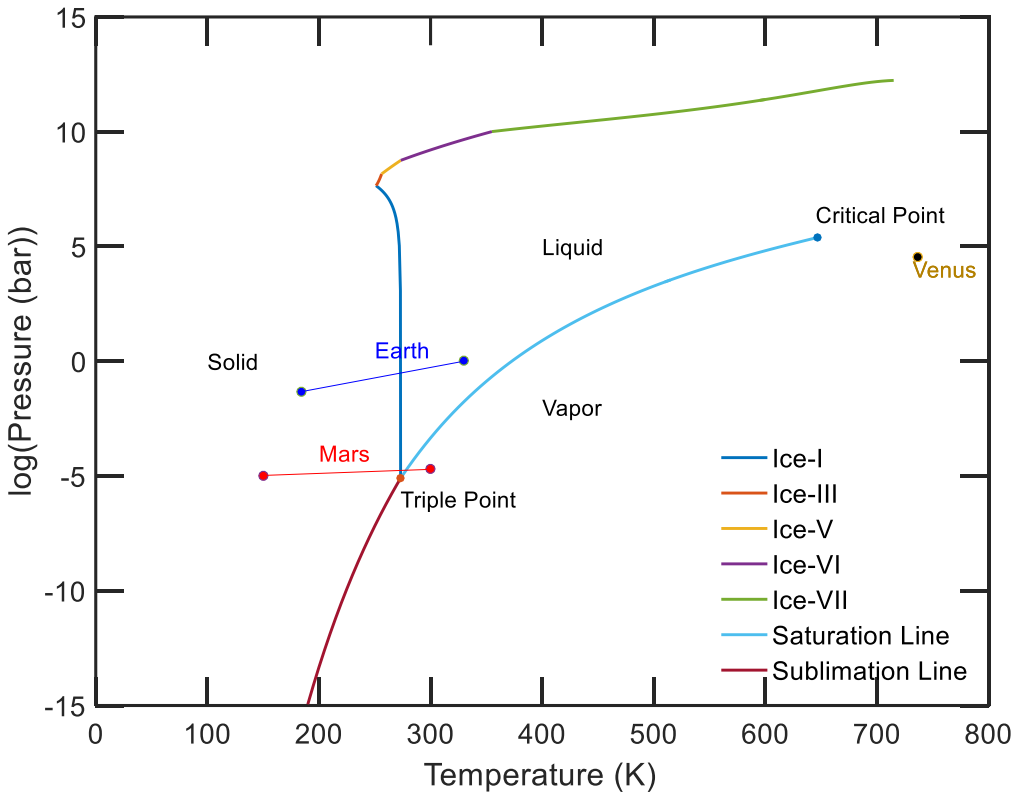

Figure 1. 1. Phase diagram of water, and range of temperature and pressure in various terrestrial planets with atmosphere.

The temperature and pressure conditions found in the solar system are much more favorable for water-ice (Figure 1.1). To date, water-ice has been discovered on the surface of Mercury, Moon, Earth, Mars, comets, asteroids, icy moons, and dwarf planets. The stability of water-ice on an atmosphere-less planetary body can be investigated by determining its sublimation rate. For an atmosphereless body like Mercury, Moon, various asteroids and icy moons, the sublimation of water-ice in vacuum (e.g. *Helbert et al.,* 2007) can be approximated by the following:

$$S = p_{sat,i}(T)\left[\frac{M_w}{2\pi RT}\right]^{1/2}$$

Where S is a mass flux due to sublimation in kg m^{-2} s^{-1} and $p_{sat,I}$ (T) is the saturation pressure in hPa as a function of temperature (T) in Kelvin, M_w is the molecular weight of water, and R is the universal gas constant. Furthermore, the saturation pressure as a function of temperature (*Andreas,* 2007) is given by the following:

$$p_{sat}(T) = 0.01\exp(9.550426 - \frac{5723.265}{T} + 3.3068\ln(T) - 0.00728332)$$

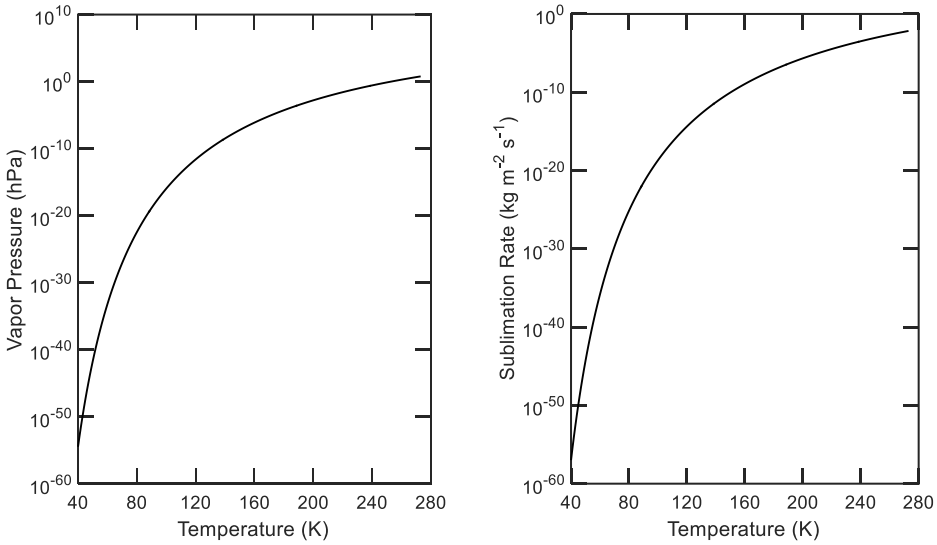

Figure 1. 2. (*Left*) Vapor pressure in hPa as a function of temperature (based on equation 1). (*Right*) Sublimation rate as a function of temperature using the vapor pressure from left, and equation 2.

In the case when another heating mechanism is absent or minor, bodies outside the snowline would, therefore, be able to host ice for a significantly long geological time, thereby explaining the ubiquitous distribution and stability of water ice in the solar system. On Mercury and Moon, ice would only be stable in regions with extremely low surface temperature such as the permanently shadowed craters and floors in the polar latitudes. On

Venus, the extremely high surface temperature exceeds the critical point of water; therefore, water cannot be liquefied. On Earth, water exists in all three forms. The only other planet in the solar system where water can exist in the liquid form is Mars (albeit for a short duration). A brief history of water on the interior planets and the Moon is presented in the following section.

1.2. Water in the Terrestrial Planets and the Moon

1.2.1. Water on Mercury:

Mercury has an axial tilt of 0.1° which means areas near the poles, especially the crater floors, are permanently shadowed from the sun. In these permanently shadowed regions of Mercury, the surface temperature never exceeds ~102 K (*Ingersoll,* 1992; *Paige et al.,* 1992), which gives a sublimation rate of water-ice at ~ 10 m per billion years (Figure 2.2; *Ingersoll,* 1992). Thermal models predict that over geological timescales, ice can remain relatively stable on the poles of Mercury, and detection of radar-bright areas by earth-based radar observation further corroborates this hypothesis (*Slade et al.,* 1992; *Harmon and Slade,* 1992). The radar reflection from Mercury's poles had similar characteristics to those of the reflections from the icy Galilean satellites (*Campbell et al.,* 1978). The source of the ice on Mercury's poles is not primordial and was likely delivered by asteroids and comets during the later stage of solar system evolution. An estimated 3 to 60E13 kg of water ice is estimated to have been deposited during the last 3.5 billion years in the permanently shadowed regions of Mercury's poles (*Moses et al.,* 1999), which would lead to ice deposits as thick as 20 m. Solar wind sputtering and meteorite impacts would lead to loss of about half of the estimated deposits. Additionally, it has also been proposed

that individual water molecules originating away from the poles could migrate to the poles and become cold-trapped (*Butler et al.*, 1993).

Measurement by the Neutron Spectrometer on NASA's Mercury Surface, Space Environment, Geochemistry and Ranging (MESSENGER) spacecraft found spectral evidence of water ice in the permanently shadowed regions of Mercury's North Polar Region (*Lawrence et al.*, 2013). MESSENGER found a pure ice buried layer under a regolith/ice mix layer that is 25 wt% water ice, with a total mass of ~2E16 to 2E18 grams. The origin of such an expansive amount of ice is consistent with delivery by comets and/or volatile-rich asteroids. Based on a surface erosion model, it is estimated that the water ice was likely emplaced within the last 18–70 My (*Lawrence et al.*, 2013).

1.2.2. Water on Venus:

The present day surface temperature on Venus exceeds 700 K, so neither liquid water nor ice can exist on the surface (e.g. Figure 1.1). Considering that terrestrial planets formed through collisions among planetesimals in the solar nebula, Venus and Earth should have had the same amount of primordial volatiles delivered. This delivery mechanism of volatiles should have been especially significant during the late heavy bombardment. During the 4 billion year timescale of evolution, it is likely that more volatiles were delivered to these planets from the outer solar system due to the intense gravitational scattering by Jupiter. The lower atmosphere of Venus has 30$\pm$10 ppm water, and the D/H ratio is 150$\pm$30 times that of terrestrial water (*de Bergh et al.*, 1995; *Donahue et al.*, 1997). It has been suggested that the enrichment of the ratio could be due to isotopic fractionation, where rapid heating of the surface led to the preferential escape of hydrogen through evaporation and or diffusion, consequently enriching the deuterium concentration. Based

on the high D/H ratio, a global ocean of at least 4 m-depth but not higher than 530-m has been suggested to once have existed on the surface of Venus (*Donahue et al.,* 1982; *Donahue et al.,* 1997). Although the present day surface is devoid of any water, the fate of water in the interior is unknown. It has been suggested that at least some of the atmospheric water may have been acquired due to outgassing from the interior (*Donahue et al.,* 1997).

1.2.3. Water on Moon:

Sinuous rilles on Moon were once thought to be water carved features (e.g. Urey, 1967), however, subsequent work proved that the features were volcanic in origin. Due to the low inclination of the Moon (similar to Mercury), the only areas around which water ice can survive are areas near the poles under permanent shadows. In these regions, temperature models and observation data show that ice would be stable for the entire lunar lifetime (e.g. Figure 1.2; *Andreas,* 2007). The first report of ice detection from the south-pole of the Moon was reported by the Clementine mission (*Nozette et al.,* 2001). Further evidence for the presence of ice on Moon was provided by the neutron data of Lunar Prospector, which showed enhanced abundances of hydrogen at both poles of the Moon (*Feldman et al.,* 1998). Near infrared absorbance of water vapor and ice, and ultraviolet emissions from hydroxyl radicals in the ejecta plume from the impact of Lunar Crater Observation and Sensing Satellite (LCROSS) in the south-pole crater Cabeus provided the most recent definitive evidence for Lunar ice (*Colaprete et al.,* 2010). The ice was inferred to be pore filling ice (i.e. accommodated within the pore space of the regolith) consistent with ice formation through atmospheric deposition.

1.2.4. Water on Earth:

Earth's current position within the "habitable" zone allows water to exist in solid, liquid and gaseous form (Figure 1.1). Liquid water on Earth (i.e. hydrosphere) comprises 0.02% of the planet's mass (*Williams et al.,* 2007), and based on oxygen isotope composition of the detrital zircons, its presence on the surface can be traced back to 4.3-4.4 Gy (*Mojzsis et al.,* 2001; *Wilde et al.,* 2001; *Valley et al.,* 2002, 2005). The exact mechanism and timing of the origin of Earth's hydrosphere is not understood, but based on the oxygen isotope in detrital zircons older than 4 Ga, it is understood that at least some of the Earth's water was deposited within a few hundred million years after the formation of solar system. The hydrosphere on earth could have been acquired through the (i) accretion of water delivered by asteroids and comets, (ii) degassing of volatiles due to impacts, or (iii) volatile degassing from the mantle.

Accretion is one of the most viable modes through which water could have been delivered to Earth and other terrestrial planets. During the late heavy bombardment, Earth and other inner planets were frequently bombarded by asteroids, comets, and planetesimals. Asteroids and comets can contain water ice and hydrated minerals in excess of 10 wt% and 50 % respectively, so at least some amount of Earth's water must be sourced from these bodies. Additionally, the present hydrosphere could have also been sourced from bodies with no existing analog left in the solar system. In the early stages of the solar system formation, most of the ice-bearing bodies formed outside the snowline (*Lunine,* 2006), and simulations designed to study the influx of water-bearing bodies that impacted Earth suggest their source to be beyond 2.5 AU from the sun (*Morbidelli et al.,* 2000; *Raymond et al.,* 2004). However, the entire inventory of Earth's water could not have been

acquired this way, because evidence for hydration of materials from depth is observed in the 4.3 Gy old detrital zircons (*Mojzsis et al.,* 2001; *Wilde et al.,* 2001; *Valley et al.,* 2002).

Besides the delivery of volatiles, large impacts could also have had a profound effect on the early atmosphere, life, and planetary evolution. Based on the size of the projectile, relatively giant impacts could have vaporized a significant amount (if not all) of the ocean water to steam. Rapid hydrodynamic escape of hydrogen inferred from the $^{22}Ne/^{20}Ne$ ratio supports this hypothesis (*Zahnle et al.,* 1990; *Pepin,* 1991). Deuterium/Hydrogen (D/H) ratio provides some constraints on the likely source of Earth's hydrosphere (e.g. *Robert,* 2001), but D/H ratios of comets are derived from only a handful of samples, and the D/H ratios of asteroids show significant variability, so there is no clear consensus on the origin of the hydrosphere based on the D/H ratio. Regardless of the source, Earth's hydrosphere has been present since at least the last 4 Gy, and it has played pivotal roles in myriads of geological, chemical, and biological processes. From the origin of life to the dynamics of volcanism, water has been the driving force for the evolution of life and the planet itself. It is, therefore, imperative for us to understand and study the possibility of liquid water elsewhere.

1.3. Conclusion

Besides Earth, the only other planet in the solar system where water may exist in a liquid state on the surface is Mars. In Chapter 2, I present various geomorphic and spectroscopic evidence for the presence of water in Mars' past. Chapter 3 details the morphological and initial spectral characteristics of dark streaks on Mars called recurring slope lineae (RSL). In chapter 4, I present spectral evidence for the role water plays in the formation of RSL. Chapter 4 also describes the discovery of a salt called perchlorate that

may be aiding in the formation of RSL. In Chapter 5, I provide evidence for how perchlorate salts may be playing a role in helping stabilize the presence of mid-latitude ice on Mars.

In addition to the delivery of volatiles, accretionary processes are also responsible for the formation of the 4 rocky planets in our solar system. The terrestrial planets share some rheological similarities such as a rocky crust, silicate mantle, and an iron-rich core, yet they have all clearly evolved very differently. The major driving force for planetary evolution is the thermal evolution of its interior. The temperature gradient in the mantle is capable of driving mantle-convection, which leads to surface stresses and deformation. Volcanism, plate recycling, and magnetic field evolution are all affected by the internal heat energy of a planet and they have significant implications for the stability of water and origin of life.

The main goal of Interior Exploration using Seismic Investigation, Geodesy and Heat Transport (InSight) mission is to understand the formation and evolution of terrestrial planets. Heat Flow and Physical Properties Probe (HP^3) is a heat flow probe on InSight that will measure the amount of heat currently escaping from the planet's interior. The measurement of current heat flow on Mars will not only help us understand the formation and evolution of terrestrial planets, but it will also help answer what if any effect heat flow may have had on the stability of water on early Mars. One of the proposed scenarios to explain the loss of water from the Martian surface is due to higher heat flow during the Noachian, which led to the evaporation of the surface water. By utilizing the gravity data from current orbiters on Mars, chapter 6 makes a series of predictions regarding the heat flow at the InSight landing site and predicts the local crustal thickness. Radiogenic

elements are the key heat producing mechanism on Mars currently, and accurate assessment of the total inventory of radiogenic elements will be dependent on our assumption of crustal thickness. While the chapter does not explicitly answer questions about the role of heat flow in the current or past inventory of water or planetary evolution, it provides key estimates and predictions that will help InSight answer those questions upon arrival on Mars.

CHAPTER 2

WATER ON MARS

2.1. Evidence for Liquid Water on Mars' Past

One of the first indicators that suggested the existence of liquid water on Mars' past was the observation of valley networks by Mariner-9 (*Marsursky,* 1973). Valley networks consist of dendritic systems that have an appearance similar to water drainage systems on Earth. They can reach lengths from a few kilometers to almost a thousand kilometers, and almost always show a dendritic pattern where tributaries converge downstream. Liquid water and alternative models including erosion by lava (*Carr,* 1974), liquid hydrocarbons (*Yung and Pinto,* 1978), wind (*Cutts and Blasius,* 1979), liquid CO_2 (*Sagan et al.,* 1973), liquefaction (*Nummedal,* 1978) and faulting (*Schumm,* 1974) have been proposed as formation hypotheses for valley networks. However, none of these non-water models appeared as plausible and liquid water was seen as the most likely erosional agent responsible for the creation of valleys and channels on Mars (*Carr,* 1981; *Baker,* 1982).

Most of these channels and valley networks occur on the ancient highlands of Mars (Figure 2.1), which is dated to be older than 3.7 Ga (*Pieri,* 1976; *Carr and Clow,* 1981). This led to a vision of ancient Mars that was much warmer and wetter than it is currently (e.g. *Squyres & Kasting,* 1994). The valley networks could have also formed under dry and cold climatic conditions. Proposed hypotheses for the formation of valley networks in such a climate include melting of dusty snowpacks by insolation (*Clow,* 1987), basal melting of snowpacks (*Carr and Head,* 2003), or melting of snowpacks by internal heat (*Zent,* 1999). There is also evidence for Amazonian-aged valleys on a few volcanoes (*Carr,* 1995; *Scott*

and Dohm, 1992; *Gulick and Baker,* 1990), but their formation mechanism is even more mysterious (e.g. Gulick, 2001).

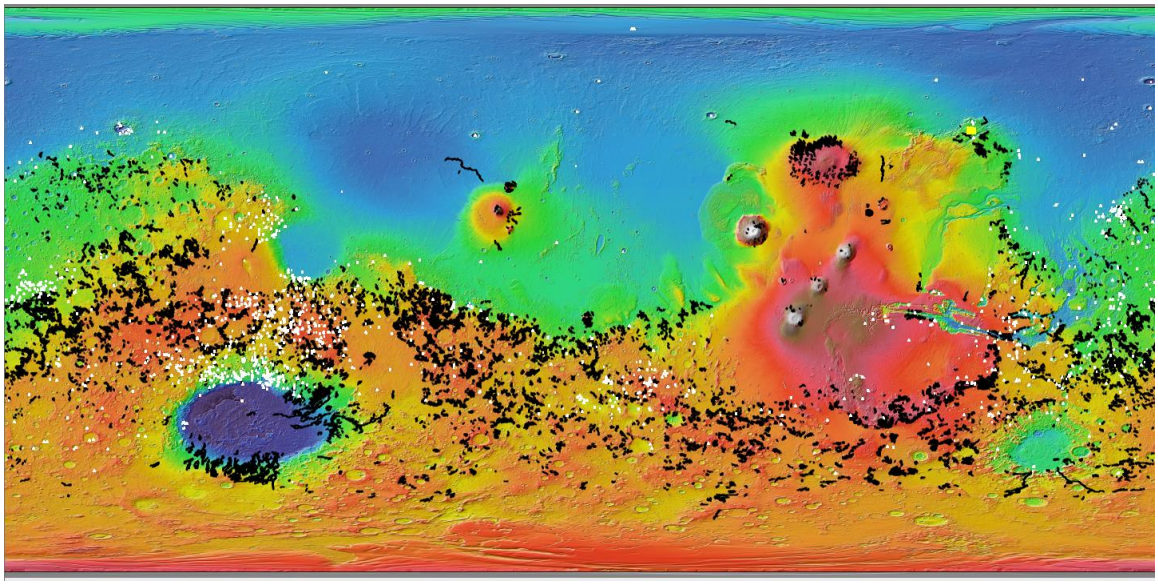

Figure 2.1. Distribution of valley networks (*Hynek et al.*, 2010) (in black) overlaid on a Mars Orbiter Laser Altimeter (MOLA) topographic shaded relief map. Brighter colors (red/yellow) are higher in elevation than the cooler (blue/green) colors. White dots outline areas where hydrous minerals have been detected via orbital spectroscopy (*Carter et al.*, 2013).

There are also numerous craters on Mars that present evidence for paleolakes (*Cabrol et al.,* 1996; *Cabrol and Grin,* 1999; *Wray et al.,* 2011; *Dehouck et al.,* 2010). Paleolakes on Mars are usually identified based on morphological indicators such as deltaic deposits (e.g. Figure 2.2), wave cut terraces, shorelines, and mineralogical identification of evaporites (*Cabrol and Grin,* 1999; *Wray et al.,* 2011). Hundreds of paleolakes have been discovered on the surface of Mars. Some of these craters even show channels feeding in or out of the craters, reminiscent of terrestrial open lakes. Eberswalde crater even shows a layered apron of debris that looks similar to deltaic deposits found on Earth (*Malin and Edgett,* 2003). Most identified paleolakes are estimated to have been active in the Hesperian (*Cabrol and Grin,* 1999).

The presence of widespread liquid water on Mars' past surface is also inferred from the inherent lack of impact craters less than 15 km (*Chapman and Jones,* 1977). The reduction in the number of craters less than 15 km is generally explained as due to degradation and eventual removal by flowing liquid water. Many of the larger craters that have survived from the ancient terrain also lack characteristic crater morphologies such as ejecta blankets, raised rims, and central peaks. These degraded craters are also generally much shallower than fresh craters at equivalent diameters, indicative of large-scale erosion (*Craddock and Howard, 2002*).

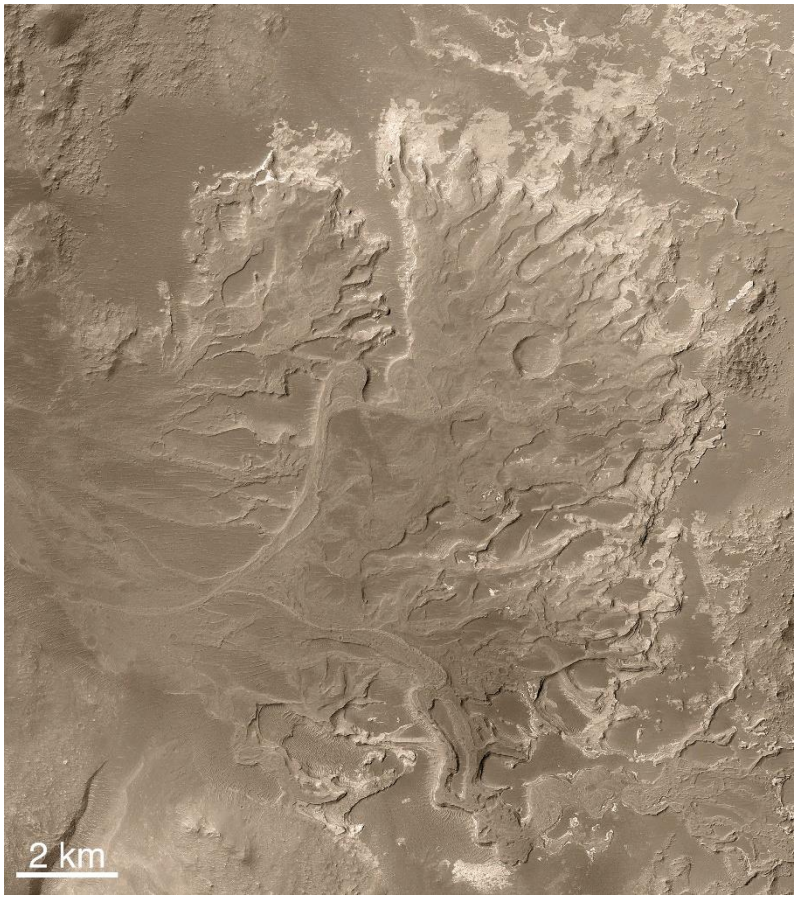

Figure 2.2. Deltaic deposits observed in Mars Orbiter Camera view of Eberswalde crater.

The most definite morphological evidence for running water on Mars' past surface are the outflow channels (*Marursky et al.,* 1973). Outflow channels are much larger than valley networks; their length can exceed thousands of kilometers, widths up to hundreds of kilometers and depths up to 1 km (Figure 2.3). This sort of large scale erosion on the surface of Mars requires the flow of a large volume of liquid water. Unlike the valley networks which are spread out throughout the ancient highlands of Mars, the outflow channels are localized to a few specific regions.

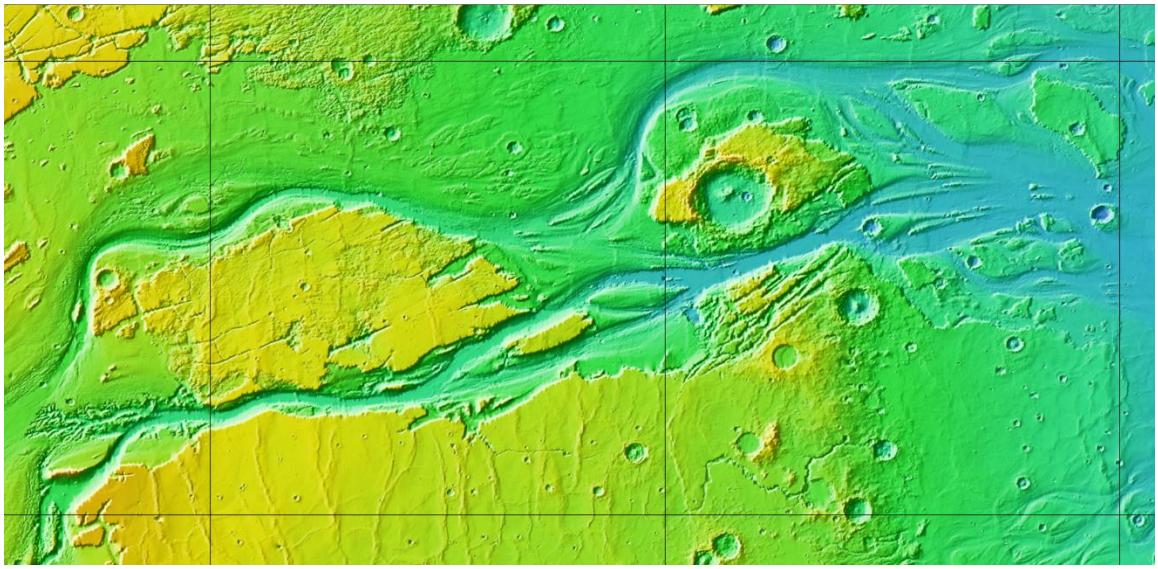

Figure 2.3. Outflow channels in Kasei Valles. The background is MOLA topographic shaded relief. The flow is from Southwest to North/Northeast. The black boxes represent boxes of 10°X10° in longitude and latitude.

Valley networks are concentrated around Tharsis, Elysium, and Hellas. It is assumed that the formation and evolution of valley networks took place from the Noachian (4.1 to 3.7 Gya) to Amazonian (3.0 Gya to present), although the peak activity is observed during the Hesperian (3.7Gya to 3.0 Gya) time period (*Clifford and Parker,* 2001; *Neukum and Hiller,* 1981; *Greeley and Guest,* 1987). Some studies have even attributed the valley networks feeding into the lowlands as the source of water that filled it to form an ancient Martian ocean (e.g. *Baker et al.,* 1991). The vast size of the outflow channels demands a

flow of high flux of water. Based on empirical models optimized for the Martian conditions, some of the biggest outflow channels on Mars would require a drainage in the outflow channel of ~E6 $m^3 s^{-1}$ (e.g. *Williams et al.,* 2010).

Aqueous alteration and spectroscopic evidence also exist and support the idea of ancient wet Mars. A plethora of mineralogical indicators indicative of aqueous alteration on Mars (including goethite, jarosite, kieserite, gypsum, sulfates, halides, phyllosilicates, hematite and nanophase iron oxide and secondary aluminosilicates such as smectite) has been discovered from orbital, lander, and telescopic observations (e.g. Figure 2.1). Thermal Emission Spectrometer (TES) on the Mars Global Surveyor (MGS) was the first to detect coarse-grained gray hematite (*Christensen et al.,* 2000), a mineral that typically requires liquid water for its formation. Observatoire pour la Mineralogie l'Eau, les glaces et l'Activitie (OMEGA) on the Mars Express spacecraft also found evidence for phyllosilicates on some of the most ancient terrains on Mars (*Poulet et al.,* 2005; *Bibring et al.,* 2006 and many others). Fe/Mg clays have been discovered within the deltaic deposits in multiple paleolakes including Jezero, Holden, and Eberswalde craters (*Ehlmann et al.,* 2008; *Murchie et al.,* 2009; *Dehouck et al.,* 2010; *Milliken & Bish,* 2010). Chloride minerals have also been found on multiple depressions across the southern highlands (*Osterloo et al.,* 2008, 2010). Sulfate minerals that most likely formed in wet acidic conditions are also found in many regions of Mars by OMEGA and Compact Reconnaissance Imaging Spectrometer for Mars (e.g. *Bibring et al.,* 2006; *Wray et al.,* 2009, 2010).

There are also multiple *in situ* lines of evidence for past flowing water on Mars. In Meridiani Planum, Opportunity observed layers of sandstone rocks that exhibited

geological structures indicative of sedimentary processes such as cross-bedding, cross-lamination, and polygonal forms (*Squyres et al.,* 2004; *Grotzinger et al.,* 2005). Curiosity also discovered Fe/Mg smectites in Yellowknife Bay at Gale crater (*Grotzinger et al.,* 2014; *Vaniman et al.,* 2014).

The geomorphic and spectral evidence of water led to a vision of wet and warm early Mars that had a thick (1-5 bars) CO_2 atmosphere (*Pollack & Kasting,* 1987). CO_2 was suggested as the most plausible greenhouse gas because the amounts required to raise the temperature to the melting point of ice, perhaps several bars, are consistent with the estimates of how much CO_2 might have been available on the planet. If Mars once did possess this thick atmosphere of CO_2, then only little of it remains to the present day. Early work suggested right after the wet and warm era of Mars, late heavy bombardment caused Mars to lose most of its CO_2 due to the formation of carbonates, and surface conditions changed to what we observe today (*Pollack,* 1979; *Pollack et al.,* 1987; *Fanale et al.,* 1992).

2.2. Present Day Water on Mars:

The notion of present-day liquid water on Mars has been controversial (e.g. *Zent et al*., 1990; *Hecht*, 2002). Viking data confirmed H_2O ice on the residual polar caps (e.g. *Kieffer et al.,* 1976; *Farmer et al.,* 1976). Spectral evidence for H_2O ice on the Southern Polar Cap was also detected by OMEGA and Planetary Fourier Spectrometer onboard Mars Express (*Bibring et al.,* 2004; *Hansen et al.,* 2005). Multiple lines of evidence also support the existence of H_2O ice on the mid-latitudes of Mars (see Chapter 5). The atmosphere of Mars is relatively dry, but during the summer months, the water vapor abundance can exceed ~100 precipitable-microns (pr-μm) in the north and ~50 pr-μm in the south (*Smith*, 2002).

The temperature and pressure conditions on the surface of Mars allow liquid water to be present transiently (e.g. *Haberle et al.,* 2001) (Fig. 1.1), and a variety of morphological features have been proposed to have formed due to the action of liquid water on present-day Mars. In the section below, I briefly describe various features on Mars that were once thought to have been formed by liquid water. Details about recurring slope lineae (RSL), which provide the best evidence for present-day liquid water on Mars, are discussed in chapter 3 and 4.

2.2.1. Gullies:

Gullies are distinctive features on Mars that were first observed by the Mars Orbiter Camera on board the Mars Global Surveyor (*Malin and Edgett*, 2000). Gullies on Mars resemble terrestrial debris flow channels, and consist of three distinct morphologic elements: (i) head alcove near their source region, (ii) channel that functions as a transport zone, and (iii) a debris apron where deposition occurs (*Malin and Edgett*, 2000). Their length can range from a few hundred meters to a few kilometers, and they can be a few tens of meter wide. The channels usually show levees, and they follow a sinuous path. The morphology of gullies on Mars suggests formation through a mass wasting process. The fluid medium and its source necessary for carving the gullies is controversial and proposed hypotheses include: (i) gas-lubricated flows due to CO_2 ice (*Hoffman,* 2000; *Musselwhite et al.,* 2001) (ii) dry granular flow (*Treiman,* 2003; *Shinbrot* et al., 2004) (iii) shallow subsurface reservoir of liquid water (*Malin and Edgett,* 2000), (iv) melting of near-surface ice by insolation (*Gilmore and Phillips,* 2002), (v) melting of ice by geothermal heat (*Gaidos,* 2001; *Hartmann,* 2001) (vi) melting of ice during periods of high obliquity (*Costard et al.,* 2002 *Christensen,* 2003; and many others).

Gullies are not observed to form in bedrock in the current climate; however, new deposits, and modification of gully channels and aprons have been observed (e.g. *Malin et al.,* 2006; *Dundas et al.,* 2010). *Harrison et al.* (2009) proposed the changes on gullies were due to liquid water activity, but the seasonality of the changes rules out the liquid water hypothesis. Instead, formation driven by CO_2 frost and dry granular flow is most consistent with the observed seasonality of gullies (*Dundas et al.,* 2010). The deposits observed near the terminus of the gullies are termed bright gully deposits (BGD) (Fig. 2.4). The first discovery of BGD was reported as a distinct light-toned flow, with relatively long, extended, digitate distal and marginal branches (*Malin et al.,* 2006). Based on photogrammetry data, the slopes where they formed were reported to be between 20° and 30°. Because the flow seemed to divert around obstacles and had relatively low relief, a very fluid-like material was suggested for their formation (*Malin et al.,* 2006). The bright-toned nature of the deposit retained over multiple mars years (MY) was attributed to replenishment of surface frost, elutriation of fine-grained sediment, or precipitation of salts (*Malin et al.,* 2006). *Pelletier et al.* (2008) conducted a 1-D and 2-D numerical flow modeling to test whether a wet or dry flow is most consistent with the deposit morphology of BGD. Dry granular flow models matched the observed run-out distance and the distal morphology the best. No spectral evidence for precipitated salts, frost or water has been found on BGD (*Ojha et al.,* 2014b).

2.2.2. Slope Streaks:

Slope streaks (SS) are ubiquitous features in the equatorial regions of Mars and are distinct from their surroundings due to their relatively lower albedo. SS were first observed in Viking data and debris weathering, stains from wet flows and erosional landslips were

suggested as formation mechanisms (*Morris, 1982; Ferguson and Lucchitta, 1983; Williams, 1991*). Observations from MGS data led to modern day brine hypotheses that included brine liquid flows, groundwater piping, mixed water-dust flows and ground wetting and/or wicking from salty liquids (*Ferris et al.*, 2002; *Motazedian*, 2003; *Miyamoto et al.*, 2004; *Head et al.*, 2007). They form in areas with relatively low thermal inertia and

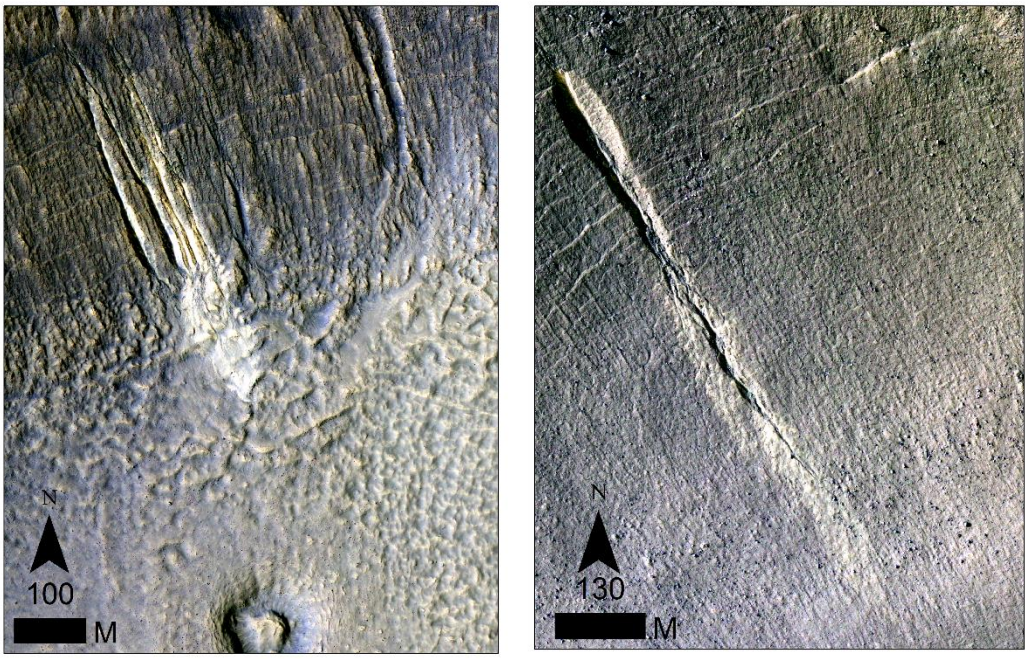

Figure 2.4. (left) HiRISE (ESP_030957_1435) (Infrared-Red-Blue/Green (IRB)) image of a bright gully deposit on a crater wall in the southern mid-latitudes of Mars (36.2°S, 198.3°E). (right) HiRISE ESP_029344_1415_IRB image of a bright gully deposit in southern mid-latitudes (38.1°S, 317.4°E) of Mars.

high dust cover index (*Schorghofer et al., 2007; Chuang et al., 2007*). The evidence of topographic relief within slope streaks based on HiRISE images has been cited as a clear indication of dry removal of grains as their formation mechanism (*Chuang et al.*, 2007). There is no evidence of seasonality in their formation, and no other requisite environmental parameters except relatively steep slopes and high dust cover are observed (Chuang et al., 2007; S*chorghofer et al., 2007).* Additionally, SS are spectrally bland and no spectroscopic

evidence has been presented to support the liquid water hypothesis (*Mushkin et al.,* 2010; *Ojha et al.,* 2014b).

2.2.3. Linear dune gullies:

Linear dune gullies (LDG) are few meter deep incisions on pole-facing slopes of sandy crater walls or dunes within the southern mid-latitudes of Mars (Figure 2.5). They are a few meters wide and can be as long as a few km (*Diniega et al.,* 2013). The first discovery of LDG was described as long, shallow, and narrow features eroded into the lee-slope of dunes in Russell crater (*Mangold et al.,* 2002). Unlike the classical meandering gullies that include alcove-channel-apron (ACA) morphology, these gullies were observed to be linear, lack the ACA morphology and were found within dune fields and on sandy crater walls within the mid-latitudes on pole-facing slopes (Figure 2.5) (*Di Achille et al.,* 2008; *Reiss et al.,* 2007). LDG originate on steep slopes (>25°); however

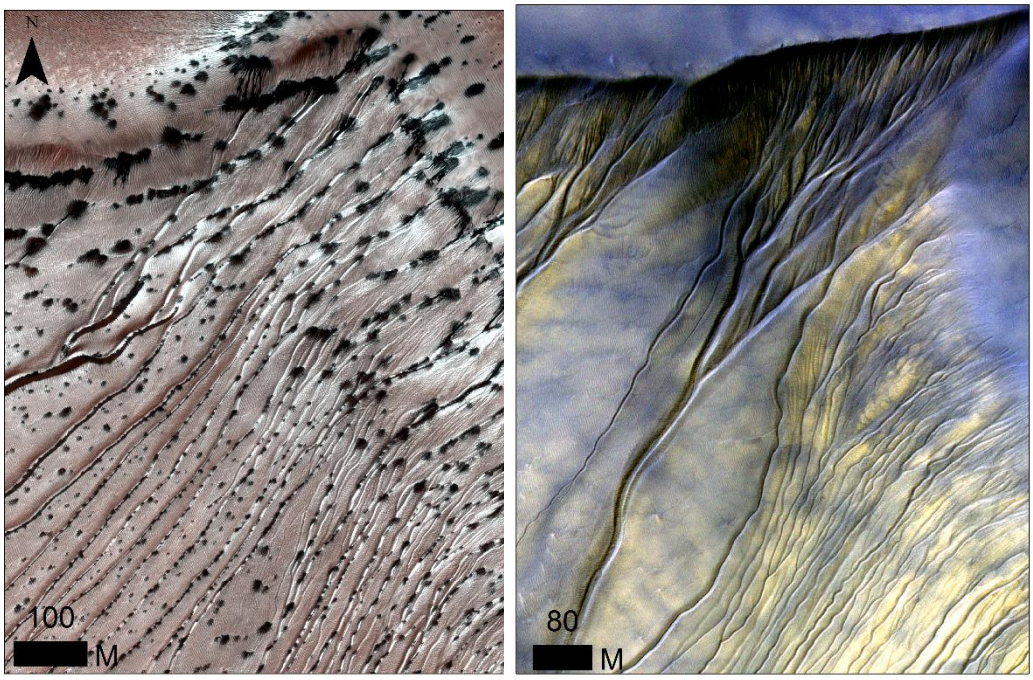

Figure 2.5. (left) HiRISE (PSP_002482_1255) (Infrared-Red-Blue/Green (IRB)) image of linear dune gullies (54.3°S,12.9°E). (right) HiRISE ESP_031755_1255 IRB image of the same site during the summer.

their grooves flow through relatively shallow slopes (~7° to 12°) which is below the angle at which dry granular material is expected to flow (*Jouannic et al.,* 2012; *Mangold et al.,* 2003; *Reiss et al,* 2007). HiRISE observations of elongation of existing grooves and formation of newer grooves have been seen as evidence for these features being active in the present-day Martian climate (*Dundas et al.,* 2012; *Reiss et al.,* 2010). Geographically, they are found within 30-70°S, and are observed to be forming and active during early spring (*Reiss et al.,* 2010; *Dundas et al.,* 2012). The formation of new grooves and elongation of existing grooves are observed yearly, and sublimating blocks of frozen CO_2 instead of water have been suggested as the erosional agent responsible for their formation (*Diniega et al.,* 2013).

In summary, while multiple lines of evidence prove the presence of liquid water on Mars' past, the presence of liquid water in the present day climate is highly debated. Multiple mass wasting features are currently active on Mars, and while liquid water has been proposed to explain the formation mechanism for some of them, the morphometry, distribution and seasonality of these features are more consistent with granular flow or erosion by other volatiles such as CO_2. Recurring slope lineae (RSL) are the best examples of active mass wasting features on Mars that are likely forming due to liquid water. In the coming chapters, I present morphological and spectroscopic data that provides clear evidence that water plays a key role in their formation.

CHAPTER 3

SPECTRAL CONSTRAINTS ON THE FORMATION MECHANISM OF RECURRING SLOPE LINEAE

3.1. Summary:

Recurring slope lineae (RSL) exhibit multiple lines of evidence for a wet origin. In the southern midlatitudes, they form on steep, equator-facing slopes that are warm during southern summer. The formation temperature, seasonality, and other geomorphic characteristics are suggestive of water-related formation, perhaps dense brines. We examined Compact Reconnaissance Imaging Spectrometer for Mars images of all confirmed RSL sites from the southern midlatitudes and the equatorial region to understand the composition of RSL and/or RSL-associated deposits. We did not detect any spectral signature attributable to water; however, a distinct and consistent spectral signature is observed at most sites, indicating enhanced abundances or distinct grain sizes of both ferric and ferrous minerals in RSL-related materials compared to adjacent non-RSL slopes. Like the RSL themselves, the strength of these signatures varies as a function of season. The observed spectral changes may indicate removal of a fine-grained surface component during RSL flow, precipitation of ferric oxides, and/or wetting of the substrate.

3.2. Introduction

Recurring Slope Lineae (RSL) are dark, narrow features that extend downslope on steep rocky slopes of Mars (Figure 3.1.a). In the southern mid-latitudes, RSL tend to form mostly on the equator facing slopes (*McEwen et al.,* 2011). They are also common in Valles Marineris and a few other equatorial locations (*McEwen et al.,* 2013). The slopes are usually very fresh, lacking any significant aeolian mantle or polygonal landforms that take many years to form. They exhibit progressive growth over time in the downslope direction. They are observed to form and grow during multiple warm seasons and are observed to fade and often completely disappear during colder seasons (*McEwen et al.,* 2011; *Ojha et al.,* 2012). RSL occur only in relatively low-albedo regions of Mars, and have an even lower albedo compared to the surroundings. Although carbon dioxide ice drives many other dynamic activities on Mars (*Hansen et al.,* 2011; *Diniega et al.,* 2010; *Dundas et al.,* 2010), the surface temperature at times and places when RSL are active is too hot for solid CO_2 to exist, but is ideal for water (*McEwen et al.,* 2011; *Ojha et al.,* 2012). Freshwater has been suggested based on observed surface temperatures (*Stillman et al.,* 2013), but given a possible subsurface source where temperatures are significantly lower, briny water with a lowered freezing point seems likely (*Chevrier and Rivera-Valentin,* 2012).

Although geomorphic, visual and temporal data supports the liquid hypothesis for RSL, spectroscopic evidence has been lacking. Compact Reconnaissance Imaging Spectrometer for Mars (CRISM; (*Murchie et al.,* 2007)) is a visible to near infrared imaging spectrometer with spectral range of ~0.36 μm to 3.92 μm. It operates with a gimbal mechanism to acquire images at full resolution of 18m/pixel. The relatively coarse

resolution of CRISM makes it challenging to observe RSL, which are a few meters wide at most. A few sites, such as Palikir crater, have dense distributions of RSL, where we expect CRISM to be able to better resolve clusters of RSL, and their inferred deposits. We sought to understand the mineralogical characteristics of RSL slopes and other features associated with RSL using CRISM Full-Resolution Targeted (FRT) and Full Resolution Short (FRS) images.

3. 3. Methodology

We analyzed CRISM images of the 13 confirmed RSL sites in the southern mid-latitudes, and confirmed RSL sites and a few other partially-confirmed sites from equatorial latitudes (*McEwen et al.,* 2013), to understand the mineralogy of RSL slopes. Useful IR (1-4 μm) data are only acquired when the CRISM coolers are active, i.e. during ~25% of observing cycles in recent years. We therefore concentrated mostly on the VNIR region (0.4-1 μm) due to its greater availability, although all IR wavelength data were also analyzed where and when available. CRISM TRR3 I/F images were downloaded and pre-processed using ENVI's CRISM Analysis Toolkit (*Murchie et al.,* 2007) to reduce atmospheric effects, map-project the images, and map parameters indicative of mineralogy (*Pelkey et al.,* 2007). Atmospheric correction was performed using the standard "volcano scan" technique (*Morgan et al.,* 2011; *Murchie et al.,* 2009).

Spectral plots were produced from observations of slopes with RSL activity. Individual RSL are smaller than the spatial resolution of CRISM (~18m/pixel), so we averaged data over RSL slopes and their associated relatively bright fans (Figure 3.1.a). The average spectrum from each region of interest (ROI) was divided by an average from a spectrally neutral region in the same scene; this use of "spectral ratios" is a standard

CRISM analysis technique (e.g., *Ehlmann et al.,* 2009) to suppress residual artifacts in the data while highlighting spectral variations within a scene. Not all denominators were chosen from the same columns, so detector-dependent noise is not completely erased from our spectra. The ratio of the same numerator area to the same denominator area was plotted for all CRISM observations available at each site, in order to observe time dependent behavior in a controlled way.

We calculated band depths for the 530 nm ferric iron absorption band as a function of season for some sites to study any time dependent behavior. To minimize human bias, we calculated the band depth using consistent local minimum and maximum wavelengths for all the images of a particular site. We also checked the atmospheric opacity and phase angle of few observation to explore whether these correlate with any observed fluctuations in band depth.

3. 4. Results

3.4.1. Southern Mid-Latitudes:

The dense distribution of RSL along with the wide expanse of bright fans that we observe at Palikir gives us the best opportunity to deduce their mineralogy (Figure 3.1). We defined an ROI dominated by bright fans (Figure 3.1.a), which are inferred to be deposits from past RSL activity (*Ojha et al.,* 2012). These fans have a distinct color in images from both CRISM and the High Resolution Imaging Science Experiment (HiRISE; (*McEwen et al.,* 2007)), and seem to be composed of homogenous material finer-grained than the surrounding area (Figure 3.1.a, b). In HiRISE Infrared-Red-Blue/green (IRB) color

Figure 3.1. (a) RSL emanating from bedrock exposures at Palikir crater (ESP_023045_1380, 41.6°S, 202.3°E, MY30, Ls: 318). Arrows point to bright, smooth fans at the base of the RSL on equator facing slopes.

images, RSL fans usually have a yellow-green or orange color (Figure 3.1.a), which is consistent with the presence of ferric minerals (*Delamere et al.*, 2010). In the southern mid-latitudes, RSL appear to flow over the bright fans during summer.

In Palikir crater, a broad absorption edge at 530 nm was observed along with a band centered near 950 nm, with the depth of both bands varying over time (Figure 3.1.c). The absorption bands are weakest prior to the onset of RSL activity (~L_s: 20-250) and strongest at the time when HiRISE started observing peak RSL activity (period when RSL were observed to grow and fade) (L_s: 282-309, in MY 30; *Ojha et al.*, 2012) (Figure 3.1.d), however they were observed throughout the southern summer. A broad absorption at 2100 nm is also observed in the IR portion of the spectra, when available (Figure 3.1.c). There seems to be no correlation between observed increase in band depth and phase angle of the images (Figure 3.1.d). Atmospheric opacity data calculated for 900 nm aerosols (*Wolff et al.,* 2009) were also plotted for all the images we examined. In general, we observe greater band depths at times of lower estimated atmospheric opacity, but these do not correlate perfectly. Additionally, non-RSL slopes lack the spectral variation observed on RSL slopes (Figure 3.1.e), so atmospheric opacity cannot be responsible for the observed variation. A possible relationship between atmospheric opacity and band depth has also been observed at other RSL locations in the southern mid-latitudes, but generally the trend is even weaker than that seen at Palikir crater (Figure 3.2.c, e).

Similar RSL spectral characteristics have been observed in other locations, including Raga and Tivat craters (Figure 3.2). However, at these sites, the spatial extents of RSL and the fans are much smaller, so our spectra may include contributions from outside the small features of interest. In Raga crater, the 530 nm absorption is strongly concentrated on the equator facing slopes of the crater where RSL and their fans are observed (Figure 3.2.a.). We observed a similar seasonal pattern of increasing 530 nm band depth with increasing

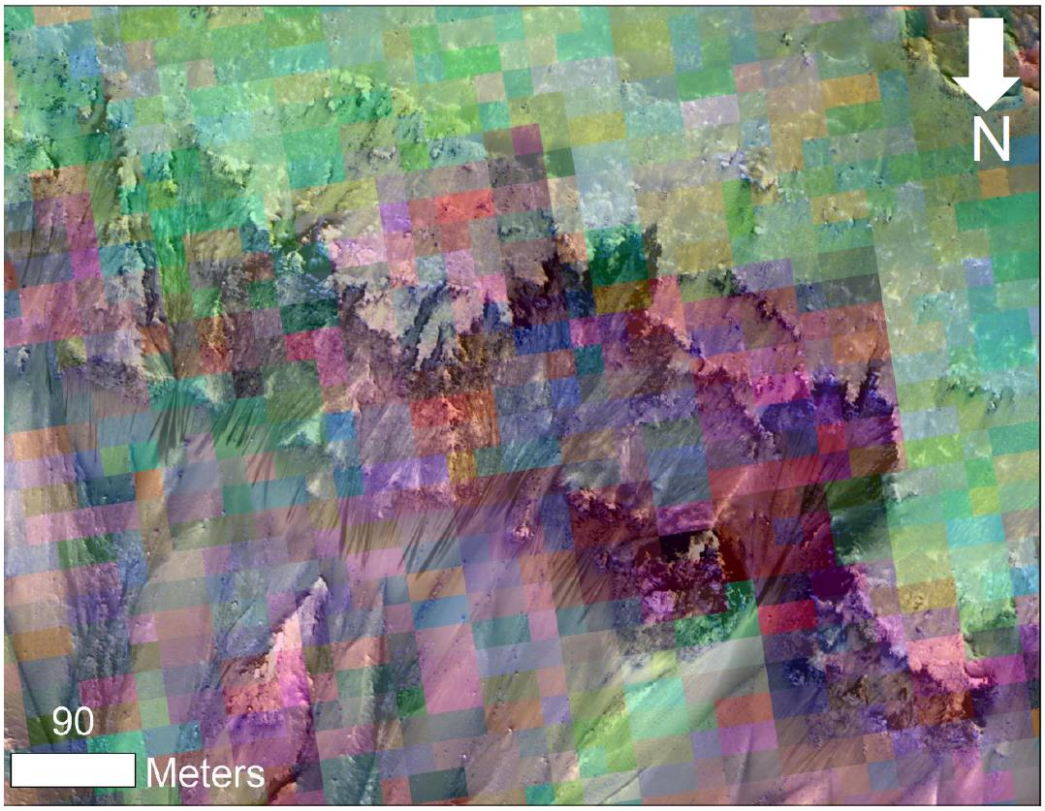

Figure 3.1. (b) CRISM FRT0001E50D (R:BD920, G:R770, B:BD530 from Pelkey et al. (2007)) overlaid on HiRISE PSP_005943_1380 (Stretched using standard deviation of the visible scene). The purple/pink color associated with RSL fans implies an enhancement in the 920 and 530 nm bands.

RSL activity (generally southern-summer L_s 270-360), although the seasonal pattern for the 950 nm band is less straightforward here (Figure 3.2.b, c). In Tivat crater, we observed the 530 nm absorption in all images, but again with higher band depths during RSL season (Figure 3.2.d, e). Here the 950 nm absorption appears only late in the RSL season (Figure 3.2.d). In Asimov crater, RSL are spread over a wide area. Here too, we observe the 530 nm and 950 nm absorptions, along with the 2100 nm absorption, but none of the RSL regions have more than two CRISM images so the spectral behavior as a function of time is not yet well constrained (Figure 3.2. f).

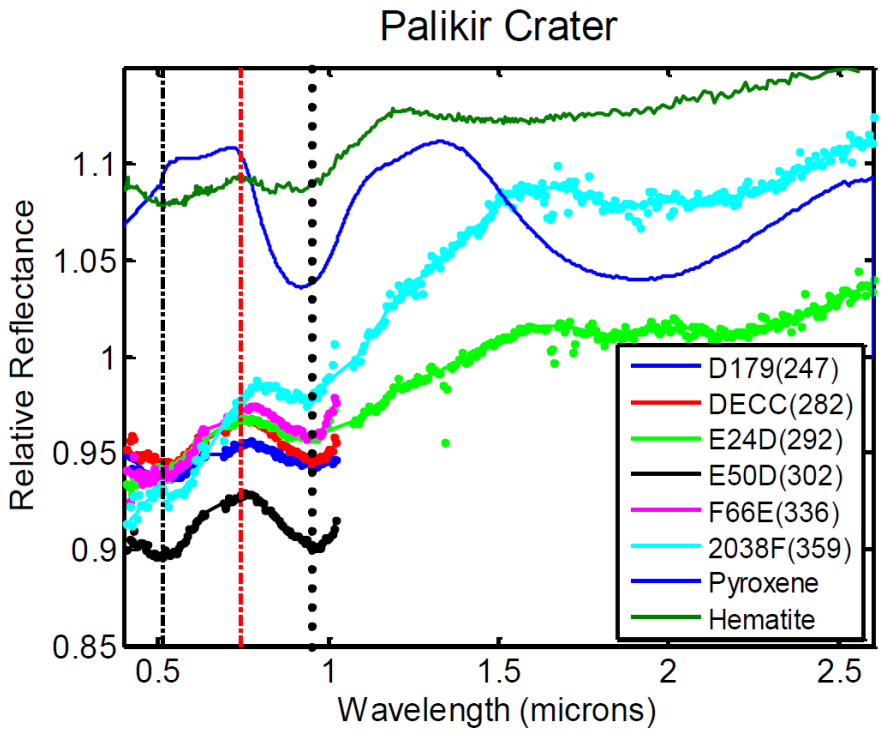

Figure 3.1. (c) Seasonal variability in spectra of Palikir crater RSL and fans. Legend lists CRISM image ID with season L_s in parentheses. Red dotted-dashed line represents band continuum (740 nm) and black dotted-dashed line represents band minimum used to compute band depth ((continuum – minimum)/continuum) for 530 nm (510 nm). Black dotted line represents center of the 950 nm absorption band.

In Horowitz crater, RSL are observed on all slope aspects of the central uplift complex (*McEwen et al.,* 2011), including on hills that expose hydrous minerals such as chlorite. The VNIR spectra of RSL in Horowitz display the 530 nm absorption, but its seasonal dependence is unclear at this site, and there is no obvious absorption at 950 nm.

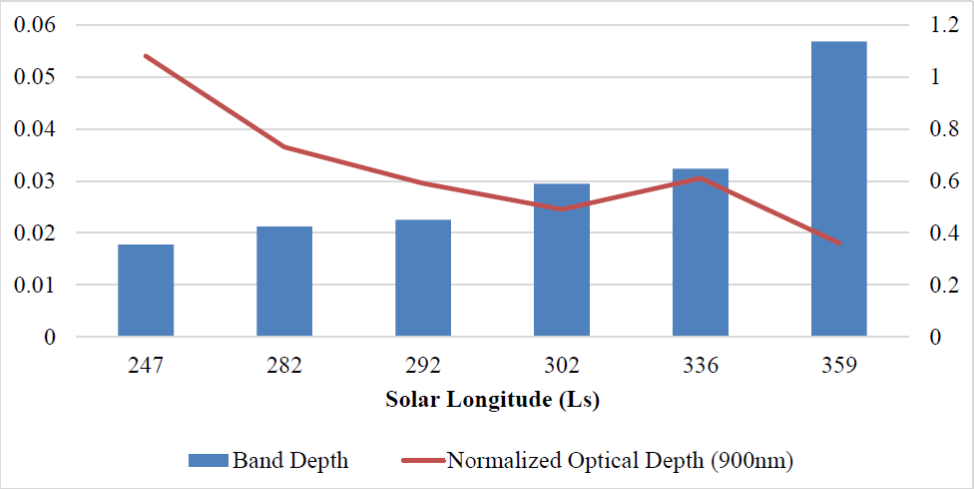

Figure 3.1. (d) Band depth calculated for 530 nm absorption band (blue bars and left axis) for Palikir crater images. Orange line represents the normalized atmospheric optical depth (values on right axis). Bold numbers on top of the bars are the phase angle of the CRISM images.

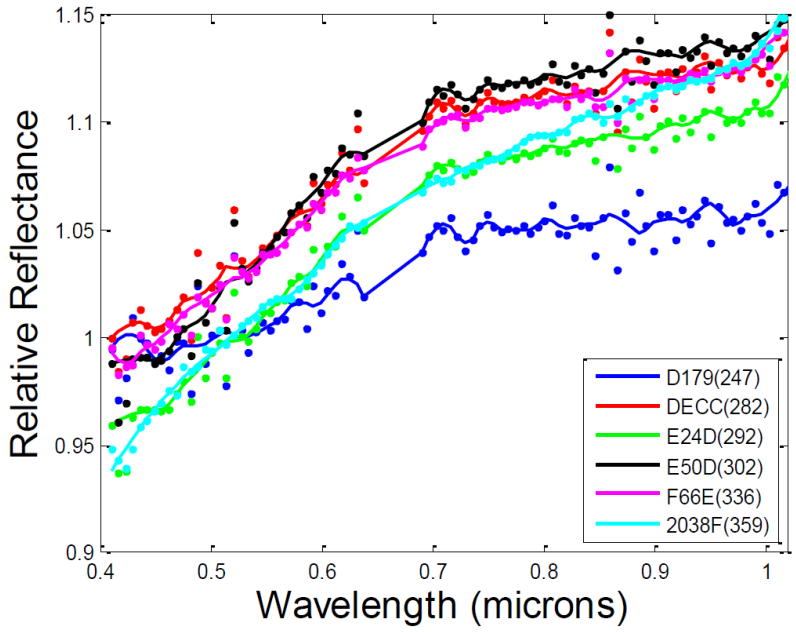

Figure 3.1. (e) Spectral variation observed on non-RSL slope. Legend same as Figure 3.1 (c).

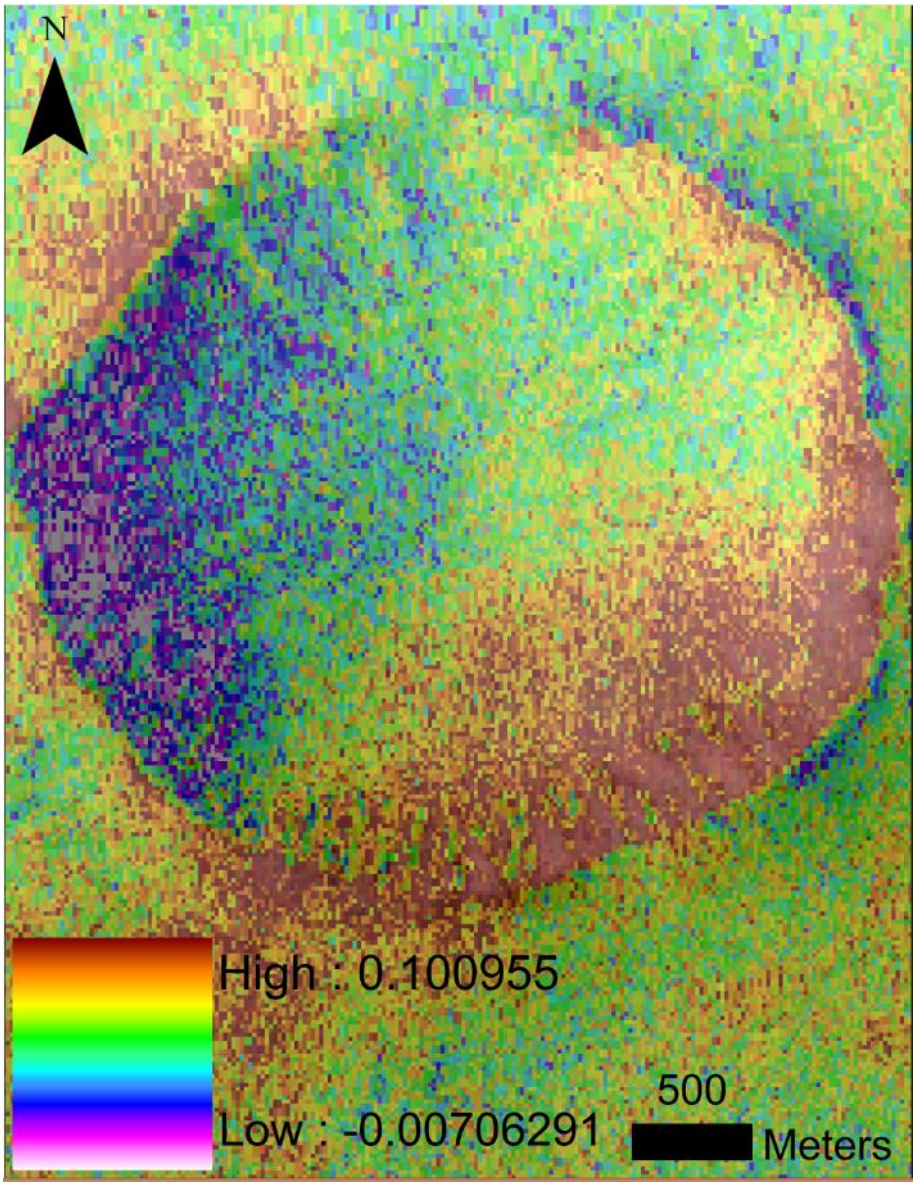

Figure 3.2. (a) BD530 band of CRISM FRT0001CEEB showing abundance of ferric minerals in Raga crater.

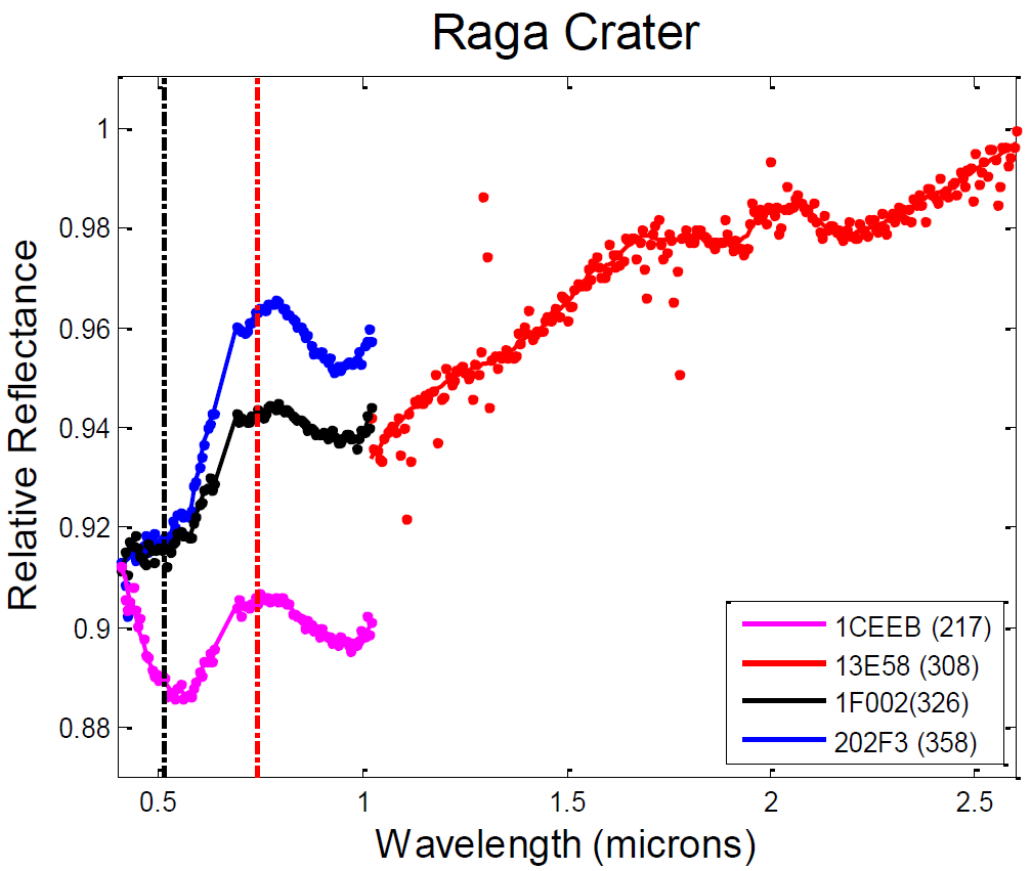

Figure 3.2. (b) Spectra of equator facing RSL slope of Raga crater (48.1°S, 242.5°E), illustrating seasonal variability.

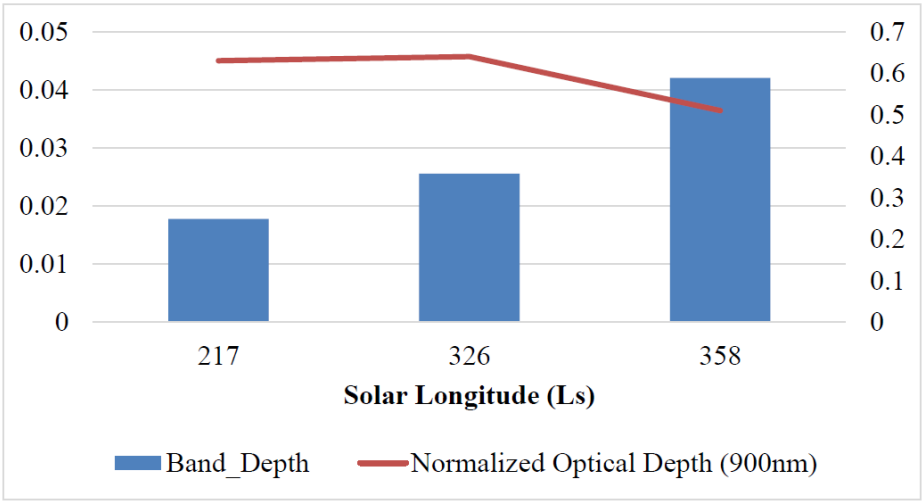

Figure 3.2. (c) Band depth calculation for 530 nm absorption for Raga crater. Orange line is the normalized optical depth.

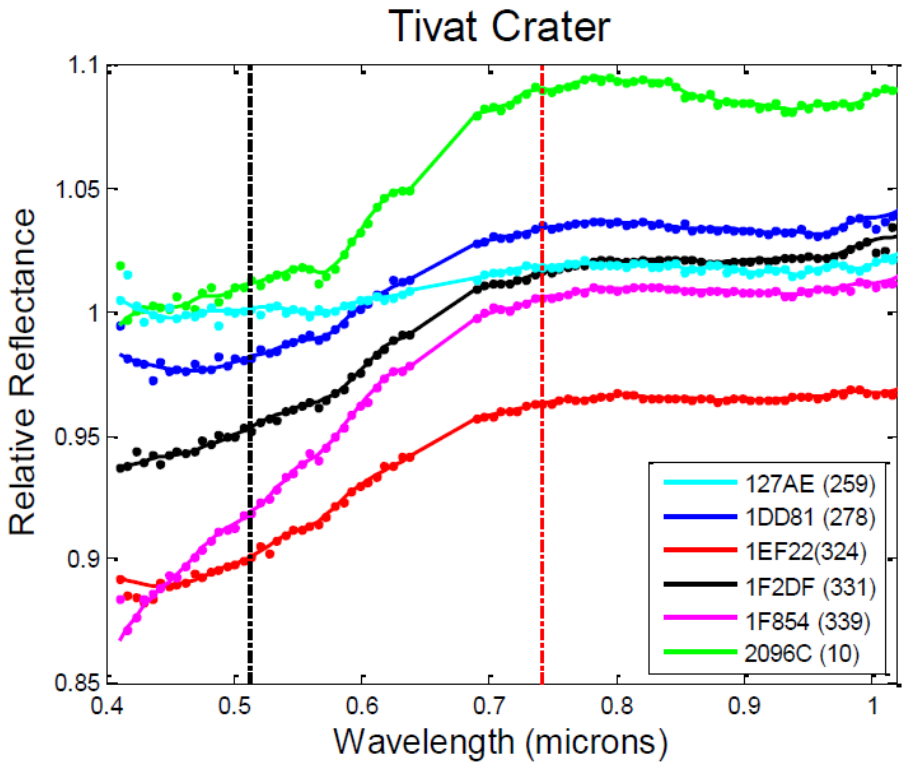

Figure 3.2. (d) Seasonal variability of spectra of equator facing slope of Tivat crater (45.9°S, 9.5°E).

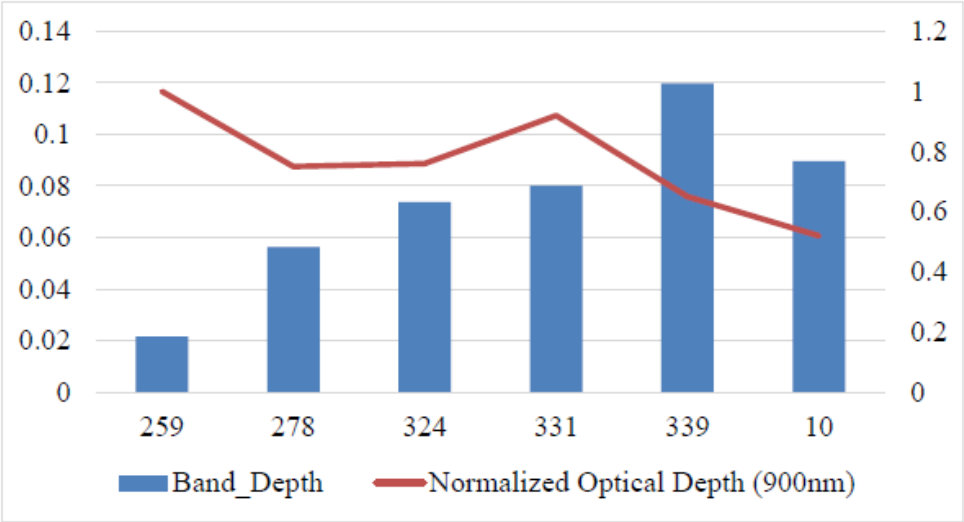

Figure 3.2. (e) Band depth calculated for 530 nm absorption for Tivat crater. Orange line same as (c).

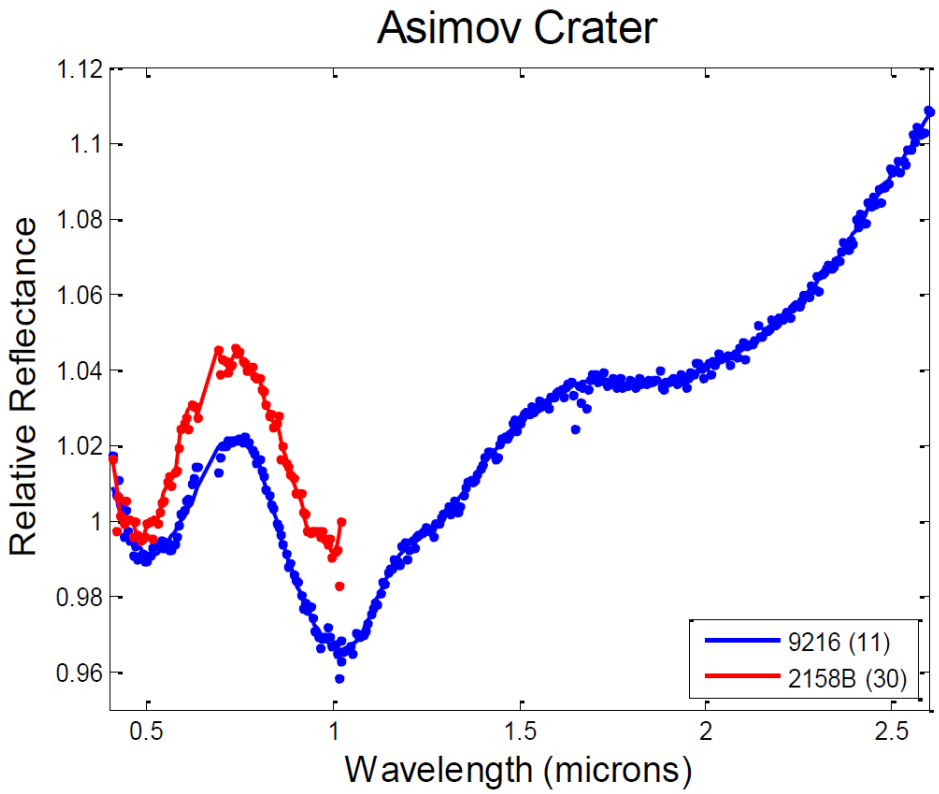

Figure 3.2. (f) Spectra of equator facing RSL slope of Asimov crater (46.9°S, 5.1°E), showing the 530 nm and 950 nm absorption along with a broad 2100 nm absorption.

We have looked at CRISM data, where available, from all other confirmed RSL sites in the southern mid-latitudes of Mars. Our results have been consistent in that we observe the 530 nm and 950 nm absorptions at most RSL sites (see Supporting Information, Table S3.1). Band depth fluctuation is observed at sites where we have good temporal coverage. Table S3.1 presents key spectral highlights from all the sites that we examined.

3.4.2. Equatorial Latitudes:

We looked at CRISM observations of all confirmed and several partially confirmed RSL sites from equatorial latitudes (Table S3.1). We plotted the normalized spectra of one of the RSL slopes from Elorza crater (Figure 3.3.a). Only one image (L_s: 31, when HiRISE observed a few small lineae and darkened fans) shows evidence for absorptions at 530 nm or 950 nm at this site (Figure 3.3.b). Additionally, no 2100 nm absorption is observed in

the IR portion of the spectrum (Figure 3.3.b). The RSL at this location are much smaller, so our lack of observation could be simply due to insufficient spatial resolution.

We looked at CRISM images of a crater on the floor of Melas Chasma. This site consists of hundreds of relatively wide confirmed RSL (Figure 3.3.c). Normalized spectra from RSL slopes show evidence for both 530 and 950 nm absorptions (Figure 3.3.d). The activity of RSL at this crater changes from SW facing to NW facing slopes between the two CRISM images, so the spectra correspond to two different slopes where RSL were observed to be active. Due to lack of repeat imaging, the time variability of the spectra from this site is not clear. We also found some locations in Valles Marineris where candidate RSL formed close to known locations of monohydrate sulfates, but the sulfate signatures do not appear especially enhanced nor depleted in the RSL or their fans specifically.

3.5. Discussion and Conclusions

The 950 nm absorption band from the VNIR data combined with a broad, shallow band centered around 2.1 μm could be attributed to pyroxene (*Adams*, 1974) with small amounts of a ferric oxide such as red hematite. The red hematite would account for the observed absorption at 530 nm, the ~700 nm shoulder, and a ~1000 nm pyroxene absorption shifted to a slightly shorter wavelength than expected (*Morris et al.*, 2000). The inferred enhancement and possible fluctuation in pyroxene signature on RSL slopes (relative to the surrounding terrain) at sites like Palikir and Raga craters seems most readily

explained as due to grain size sorting within the fans, in which a fine component is removed, leaving a coarser grained residue with stronger spectral signatures of

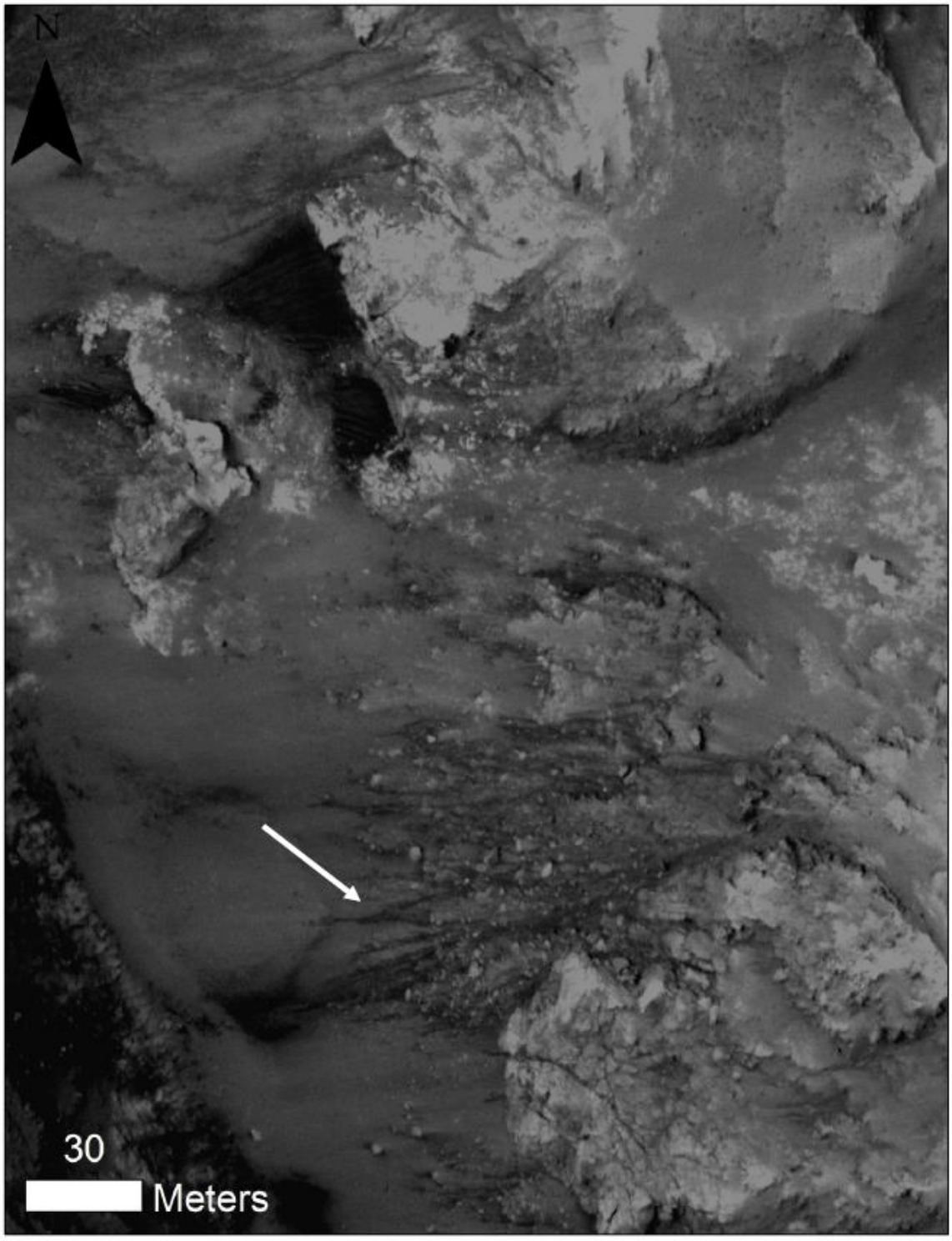

Figure 3.3. (a) Elorza crater (PSP_005649_1710; 8°S, 305°E, Ls: 329). Arrows point to RSL. Downhill is to the left.

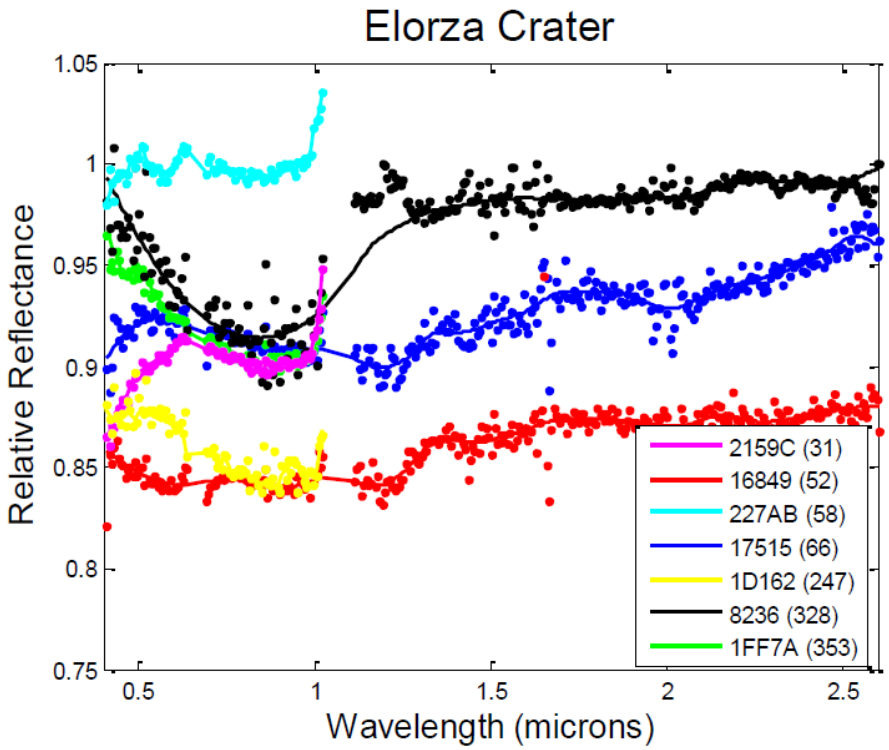

Figure 3.3. (b) Spectra of RSL slope from (a). The steep rise around 1 micron is not real as these wavelengths have degraded accuracy (*Murchie et al.*, 2009).

pyroxene (e.g., *Pieters*, 1983) and red hematite in the coarse component. The enhanced 530 nm band could also originate from an additional ferric component that changes in abundance over the RSL season, as previously suggested for other relatively dark slope features on bright regions of Mars (*Mushkin et al.*, 2010). Although, wet processes can cause grain size sorting, we did not find any water related absorptions on RSL slopes. Many other dry processes including saltation, dust deposition, Brazilian nut effect can be the cause of grain size sorting within the RSL fans. We also did not find evidence of phase angle or atmospheric opacity playing a role in the observed spectral fluctuation. The lack of water related absorptions also rules out hydrous ferric salts as a spectrally dominant

phase on the RSL slopes, despite hypothesized evidence for their presence in the sub-surface throughout the southern mid-latitude soils of Mars (*Karunatillake et al.,* 2013).

In principle, seasonal fluctuation in spectral properties of RSL sites could also be due to wetting of the substrate, which would lower the overall reflectance and deepen the overall band depths of any absorbing minerals that are present (*Balsam et al.*, 1998). At Palikir crater, the deepest band depths and the lowest reflectance occur during RSL season (Figure 3.1.c, d). If RSL are formed by brines or pure water then it is possible that the wetness of the substrate is responsible for lowering the overall reflectance and deepening the band depths. Atmospheric opacity may also have an effect, based on our inference of deeper band depths coinciding with lower estimated 900 nm aerosol opacities. However, southern summer (when RSL are most active) is generally the dustier season on Mars, so the 900 nm aerosols may not fully represent the atmospheric behavior, and the increasing band depths observed at these sites during RSL seasons (Figure 3.2.c, e) likely have a non-atmospheric component. This is further supported by several instances where the band depth increases even when opacity has also increased. Wetting of the substrate or grain size sorting that increases during the RSL season may therefore play a role in the observed temporal variations, and regardless atmospheric opacity cannot explain the spectral differences between RSL slopes and adjacent non-RSL slopes (Figure 3.1.e).

The lack of water-related IR absorptions (e.g., at ~1.4 and 1.9 μm) seemingly precludes hydrous ferric salts as a spectrally dominant phase on the RSL slopes, however several laboratory spectroscopy studies of ferric sulfates have shown that the water related features reduce considerably under exposure to Martian conditions (*Cloutis et al.,* 2008; *Rice et al.*, 2011; *Wang and Ling,* 2011). These absorptions would also be expected for a

wet surface, but when exposed to desiccating conditions they vanish rapidly, even while the surface still retains its darkened albedo (*Massé et al.,* 2012). In water tracks (a proposed terrestrial analog for RSL), the volumetric water content (VWC) increases with depth (*Levy et al.,* 2011). Since IR spectrometers are only sensitive to microns depth, the absence of hydration-related spectral features may be explained by low VWC on the surface. However, we do observe distinct spectral absorptions, fluctuations in band depth and in relative reflectance that can be attributed to wetting of the substrate or grain size sorting. Additionally, H_2O and S chemical maps (sensitive to decimeter depths) support sulfate-driven hydration of bulk soil in the Southern Hemisphere (*Karunatillake et al.,* 2013), including a consistency with hydrous Fe^{3+} sulfates in the latitudinal band of RSL.

Future laboratory modeling that recreates RSL-like morphology with both dry and wet mechanisms, coupled with spectral documentation, will be crucial towards our understanding of RSL. A comparison of VNIR spectra we observe with CRISM to laboratory spectra of RSL created with dry and wet flow will provide insights into their possible formation mechanism. We are also continuing to monitor both equatorial and mid-latitude RSL sites with CRISM, looking for seasonal patterns and assessing their repeatability from year to year, which might further constrain RSL formation processes.

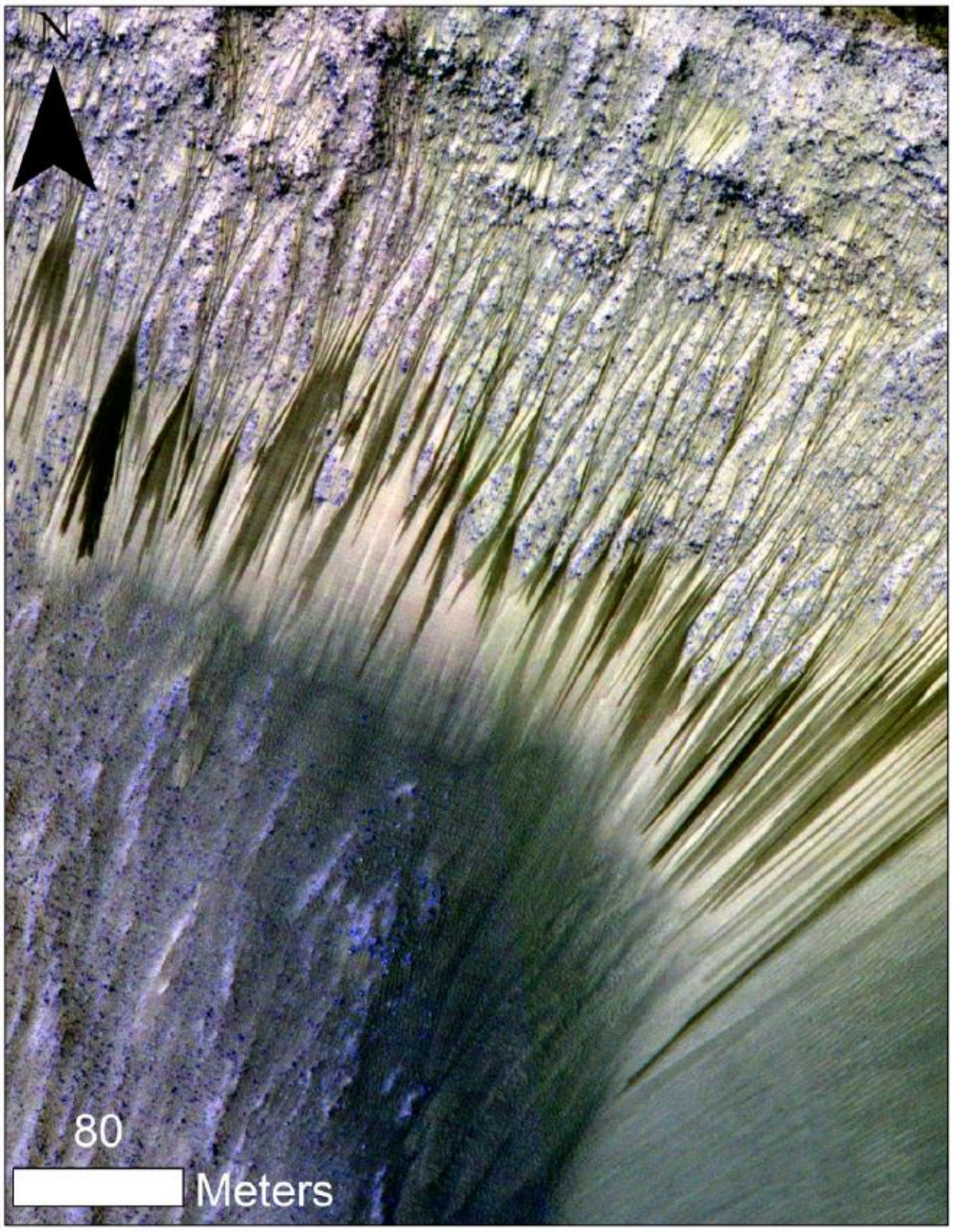

Figure 3.3. (c) RSL in a crater in central Valles Marineris (ESP_031059_1685; 11°S, 290°E, Ls: 281). The RSL are on slopes facing south toward the summer sun.

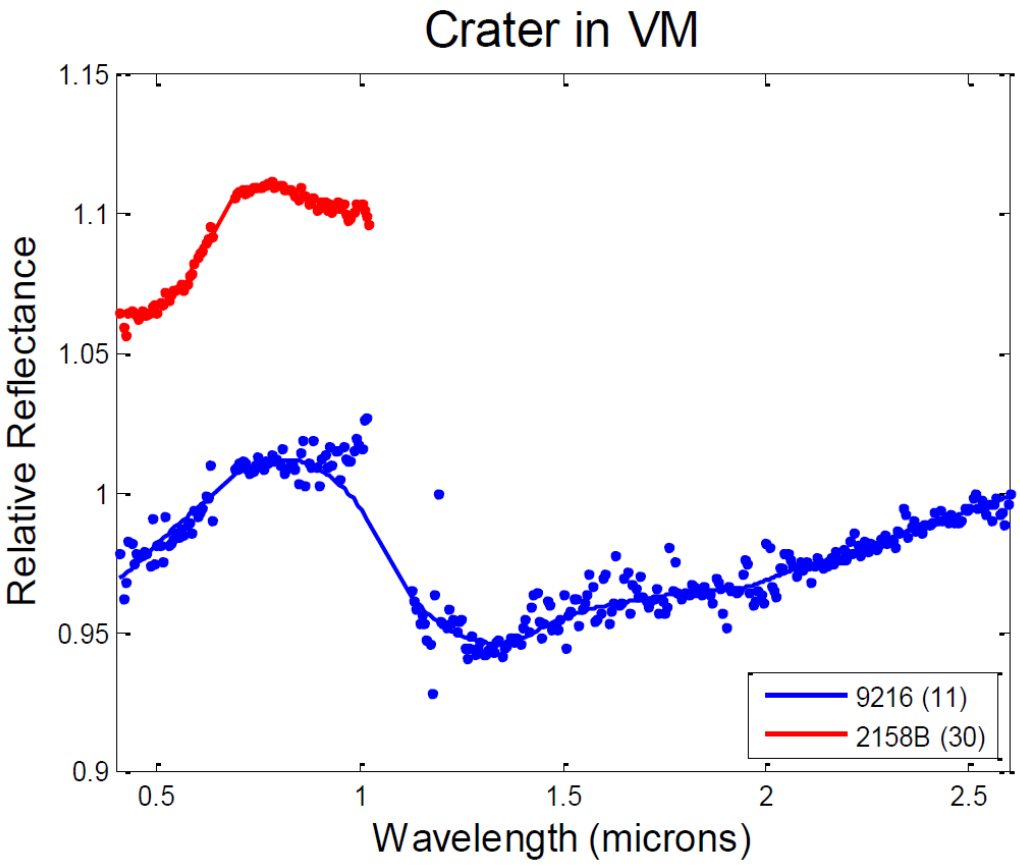

Figure 3.3. (d) Spectra from two CRISM images of (c). The two spectra correspond to two different slopes where RSL were observed to be active.

CHAPTER 4

SPECTRAL EVIDENCE FOR HYDRATED SALTS IN RECURRING SLOPE LINEAE ON MARS

4.1. Summary:

Determining whether liquid water exists on the Martian surface is central to understanding the hydrologic cycle and potential for extant life on Mars. Recurring slope lineae, narrow streaks of low reflectance compared to the surrounding terrain, appear and grow incrementally in the downslope direction during warm seasons when temperatures reach about 250–300 K, a pattern consistent with the transient flow of a volatile species (*McEwen et al.,* 2011; *McEwen et al.,* 2014; *Ojha et al.,* 2014). Brine flows (or seeps) have been proposed to explain the formation of recurring slope lineae (*McEwen et al.,* 2011; *McEwen et al.,* 2014; *Ojha et al.,* 2014), yet no direct evidence for either liquid water or hydrated salts has been found (*Ojha et al.,* 2013). Here we analyze spectral data from the Compact Reconnaissance Imaging Spectrometer for Mars instrument onboard the Mars Reconnaissance Orbiter from four different locations where recurring slope lineae are present. We find evidence for hydrated salts at all four locations in the seasons when recurring slope lineae are most extensive, which suggests that the source of hydration is recurring slope lineae activity. The hydrated salts most consistent with the spectral absorption features we detect are magnesium perchlorate, magnesium chlorate and sodium perchlorate. Our findings strongly support the hypothesis that recurring slope lineae form as a result of contemporary water activity on Mars.

4.2. Introduction

Water is essential to life as we know it. The presence of liquid water on Mars today has astrobiological, geological, and hydrological implications and may affect future human exploration. Various salts (e.g., sulfates, chlorides and perchlorates) have been detected on the surface of Mars from remote and in situ investigations (*Hecht et al.,* 2009; *Glavin et al.,* 2013; *Ehlmann & Edwards,* 2015). These salts can lower the freezing point of water by up to 80 K, lower the evaporation rate of water by an order of magnitude, and can be hygroscopic (i.e., able to easily absorb atmospheric moisture) (*Pestova et al.,* 2005; *Chevrier et al.,* 2009; *Hanley et al.,* 2012; *Altheide et al.,* 2009), thus increasing the possibility of forming and stabilizing liquid water on the surface of present day Mars (*Martin-Torres et al.,* 2015).

Recurring Slope Lineae (RSL) are narrow, low-reflectance features forming on present-day Mars that have been hypothesized to be due to the transient flow of liquid water. RSL extend incrementally downslope on steep, warm slopes, fade when inactive, and reappear annually over multiple Mars years (*McEwen et al.,* 2011; *McEwen et al.,* 2014; *Ojha et al.,* 2014). Average RSL range in width from a few meters (<5 m), down to the detection limit for the High Resolution Imaging Science Experiment (HiRISE) camera (~0.25 m/pixel) (*McEwen et al.,* 2007). The temperatures on slopes where RSL are active typically exceed 250 K and commonly are above 273 K (*McEwen et al.,* 2014). These characteristics suggest a possible role of salts in lowering the freezing point of water, allowing briny solutions to flow (*McEwen et al.,* 2011; *McEwen et al.,* 2014; *Ojha et al.,* 2014). Confirmation of this wet origin hypothesis for RSL would require either (i)

detection of liquid water absorptions on the surface, or (ii) detection of hydrated salts precipitated from that water.

The mineralogic composition of RSL and their surroundings can be investigated using orbital data acquired by the Compact Reconnaissance Imaging Spectrometer for Mars (CRISM) on the Mars Reconnaissance Orbiter (MRO), which acquires spectral cubes with 544 spectral channels (~0.4 μm to 3.92 μm) (*Murchie et al.,* 2007). Within the infrared (IR) detector spectral range of CRISM (1-3.92 μm), both liquid water and hydrated salts have diagnostic absorption bands at ~1.4 μm, ~1.9 μm and a broad absorption feature at ~3.0 μm (*Clark,* 1999) (Figure 4.1). In addition, hydrated salts may exhibit combinations or overtones at other wavelengths from 1.7 μm to 2.4 μm. Given the coarser spatial sampling of CRISM (~18 m/pixel) compared to HiRISE, few locations exist in which RSL are wide or dense enough to fill even a single CRISM pixel. In this work, we devised a variety of methods to reduce uncertainties from extraction of CRISM spectra from individual pixels, allowing examination of pixels mostly filled by RSL.

4.3. Dataset and Methodology:

CRISM (*Murchie et al.,* 2007) full-resolution targeted (FRT ~18 m/pix), full-resolution short (FRS ~18 m/pix), and Along Track Oversampled (ATO 18 m/pix, with enhanced overlap to support processing to ~6 m/pixel) observations at Infrared (IR: 1.0-3.9 μm) wavelengths coordinated with HiRISE observations were used to examine the spectral characteristics of RSL. We chose not to inspect images in the VNIR detector range (0.4-1.0 μm), because our focus was clear evidence for or against signs of hydration, which is primarily detected using absorptions in the IR detector wavelength range. The CRISM images which were analyzed to study spectral characteristics of RSL described here are

listed in Table S4.1, along with the coordinated HiRISE images in which the lineae were initially identified. Table S4.1 also lists the central latitude and longitude of the images along with their solar longitude (L_s), and exact coordinates for the location of spectra presented here. Table S4.2 lists exact coordinates of the denominator areas used to create the ratio spectra of RSL shown here. CRISM I/F images were downloaded from PDS and were preprocessed using ENVI's (Exelis Visual Information Solutions) CRISM Analysis Tool (CAT) (*McGuire et al.,* 2009) to reduce atmospheric effects, and when necessary map project the images.

A significant challenge in conducting a spectroscopic study of RSL is uncertainty in the precise location of the feature seen in HiRISE data within CRISM images. Most individual lineae are a few meters wide and several times narrower than a CRISM pixel, but for sites discussed here, individual lineae overlap so that their footprints occupy a footprint close to that of a CRISM pixel. Previous work inspected only averages of many CRISM pixels, such that absorptions present over smaller areas would have been significantly weakened due to areal mixing. Given uncertainty in the location of RSL in CRISM observations, we instead searched for evidence of hydration in areas of CRISM images where RSL are detected in higher-resolution coordinated HiRISE images. We used multiple volcano-scan (*McGuire et al.,* 2009) observations to divide out atmospheric gas absorptions. We then normalized the entire image by generating a mean spectrum from a spectrally neutral area in the CRISM image, and dividing the entire atmospherically-corrected image by that neutral area. Denominator areas typically consisted of a few hundred pixels. Additionally, we tested multiple denominator areas to confirm that any apparent absorption features were independent of that choice. Once a satisfactory ratio

image was created, we inspected the approximate RSL area pixel-by-pixel to seek any signs of hydration. We observed areas with weak signs of hydration on and near RSL. Once these areas of enhanced hydration were identified, we normalized the spectra from a region of interest using a denominator area from the same detector column in the atmospherically corrected image (Table S4.2). Reduction in systematic noise was significant, and the depth of hydration absorption bands relative to noise increased.

We also designed a band-detection algorithm to objectively discriminate between signal and noise. We apply a smoothing (moving-average) filter to a normalized reflectance spectrum and remove the continuum by dividing the original spectrum by a 7^{th} order polynomial-fit continuum curve. A band-detection algorithm was implemented with a threshold distance of at least 0.2 μm between subsequent bands. The width and depth of each band was calculated to find the approximate area within the band. Any band detected by the algorithm that has an area higher than the mean of all the "bands" at any wavelength was characterized as a real signature. In the particular case of Palikir crater, where a probable 2.15 μm absorption band is observed, the program identified the 1.9 μm absorptions as real for all 6 pixels (Figure 4.11). In three cases out of the six, the program also identified the 2.15 μm absorption feature as a true signal. The flowchart for the algorithm is presented in Figure 4.14.

Although the detection of 1.9-μm hydration bands in all areas presented is robust, we wanted to ensure that the observed absorption is time-variable and corresponds with RSL activity. In Palikir crater, four coordinated HiRISE/CRISM observations exist (Table S4.1). Spectral absorptions indicative of hydrated salts only occur in the images acquired towards the end of the southern summer, when fading RSL were observed to be longest

and widest. At all other sites reported here, no other images from different seasons or Mars year exist to conduct a temporal study. Although we do not report negative results here, we conducted a spectroscopic search for signs of hydration in many other RSL sites (some with adequate temporal coverage), but no enhanced hydration absorptions were observed.

Spectral mixture models were created using laboratory spectra of various salts and reference spectra from each CRISM scene. In order to introduce similar noise content in our spectral mixture model as observed in spectra of RSL, we extracted reference spectra from areas listed in Table S4.2. These areas are in the same column as where we observed RSL hydration features, and were ratioed using the same denominator used for RSL spectra (hereafter referred to as "Martian soil" spectrum). A linear combination of Martian soil and various laboratory spectra of perchlorate, chlorate and chloride salts (*Hanley et al.,* 2015; *Crowley et al.,* 1991) was used to find the best matching spectra. In addition, we also ran a least-square regression analysis between the observed spectrum and mixtures of various oxychlorine perchlorate species to match the position of the 1.4 μm absorption. The best match from the linear regression routine is shown in Figure 4.6. While perchlorates can explain the narrowness of the observed absorptions, the inability to match the exact wavelength of the 1.48 μm band suggests the presence of an additional salt. We ran a similar least-square regression analysis between the observed spectrum and mixture of various sulfates to explore if there is a better match (Figure 4.8). While the best fit linear-mixture of alunite (11.5%), jarosite (26.78%), Fe^{3+}-sulfate (19%) and Martian soil

(42.65%) has an absorption band at ~1.48 μm, the linear mixture does not have an absorption band at 1.90 μm and 2.14 μm (Figure 4.8).

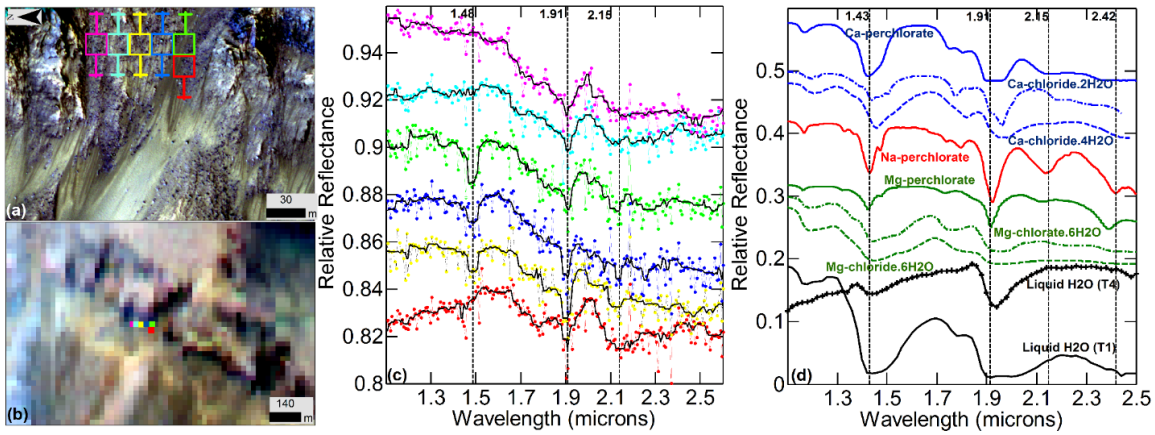

Figure 4.1. Palikir crater RSL and spectral detection of hydration features. **(a)** RSL on slope of Palikir crater ESP_024034_1380 (Infrared-Red-Blue/Green (IRB)) (L_S: 359 MY: 30). Colored boxes show the location of the CRISM pixels with the uncertainty. **(b)** Concurrent CRISM observation FRT0002038F (R: 2.53 μm, G: 1.51 μm, B: 1.08 μm) showing the same area as (a). **(c)** Spectra from colored ROIs shown in (a) and (b). The observed data are plotted with color lines, and the smoothed data in black lines. **(d)** Laboratory spectra of various salts (*Hanley et al.*, 2014; *Hanley et al.*, 2015; *Crowley*, 1991) and liquid water (T1 = 1, and T4 = 4 hours into dehydration) (*Massé et al.*, 2014).

4.4. Results:

At Palikir crater, RSL are observed to be longest and widest towards the end of the southern summer. In the HiRISE image acquired at the end of the southern summer of Mars Year (MY) 30, wide RSL were observed on the slopes of Palikir (Figure 4.1, Table. S4.1). CRISM spectra from this dense region of RSL were inspected. Six individual CRISM pixels exhibit enhanced hydration absorption features (Figure 4.1, Table S4.1). The CRISM pixels closest to the wide RSL exhibited absorption features at wavelengths near ~1.48 μm, 1.91 μm (Figure 4.1) and ~3 μm (Figure 4.7), whereas pixels farther away from RSL only exhibited absorption features at ~1.91 μm and ~3 μm (Figure 4.2 and Table 4.1). In general, the ~1.4 μm absorption feature generally weakens with dehydration and disappears more rapidly than the ~1.9 μm and 3.0 μm absorption bands (*Massé et al.*, 2014). This suggests

a higher hydration state in areas closest to the RSL core. The 1.9 μm absorption is also present in the unratioed I/F spectrum, precluding ratio artifacts as the source of the absorption band (Figure 4.7). We carried out a statistical study to elucidate true signal from noise. The 1.9 μm absorption is consistently well above the noise threshold, and in half of the cases the 1.4 μm and 2.15 μm absorption features are also above the noise threshold (Figure 4.11). The wavelength position of the observed 1.4 μm absorption is longer than is typical of perchlorates, suggesting the presence of an additional mineral.

We also analyzed CRISM observation of Palikir crater during the middle of MY 30 southern summer when RSL were shorter and narrower and found no evidence for absorption features at ~1.4 μm and/or 1.9 μm anywhere surrounding the RSL (Figure 4.4 and Table 4.1). In MY 31, only the image from the end of the summer (FRT00029F0C) showed 1.9 μm and 3.0 μm absorptions (Figure 4.5). Detections of hydration bands from both MY are only from late-season images where RSL are observed to be the widest consistent with our hypothesis that the hydration feature is due to areally extensive presence of RSL.

The absorptions observed in CRISM images of Palikir are too narrow to be explained by liquid water. Instead, they may be consistent with hydrated salts (Figure 4.1). The rapid change in hydration state of the minerals imply that at the times and places where RSL form, either (a) the hydration state of the minerals is being increased by the presence of RSL, or (b) hydrated minerals are deposited by RSL and later desiccated. A linear spectral mixture of Martian soil with Mg perchlorate, chlorate, and chloride provides the closest match (Figure 4.6).

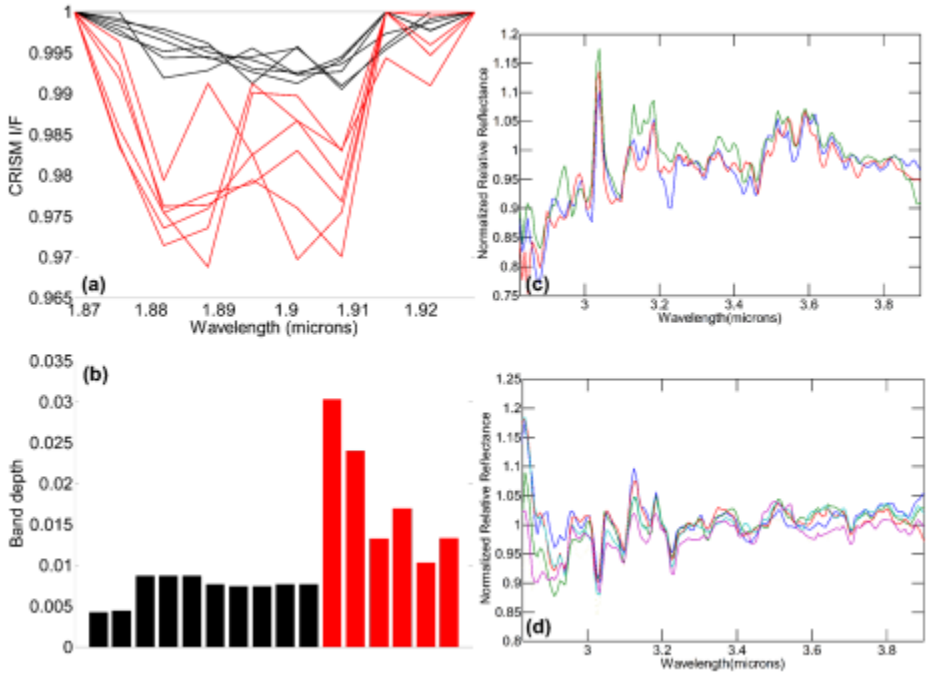

Figure 4.2 Spectra of RSL and a non-RSL region with similar albedo from CRISM FRT0002038F. **(a)** Continuum removed CRISM I/F reflectance spectra of the RSL pixels in red and non-RSL pixels in black showing absorption band at 1.9 μm. **(b)** Band-depth computed from the plot in (a). Red and Black corresponds to RSL and non-RSL slopes. **(c)** CRISM reflectance spectra ratioed to nearby non-RSL areas and normalized to relative reflectance at 2.6 μm. All RSL pixels show an enhanced absorption band at ~3 μm. **(d)** Same as (c) but for non-RSL regions with similar albedo. The latter spectra lack enhanced absorption bands at 1.4 μm, 1.9 μm and 3.0 μm (see Table S4.2 for the location of the spectra).

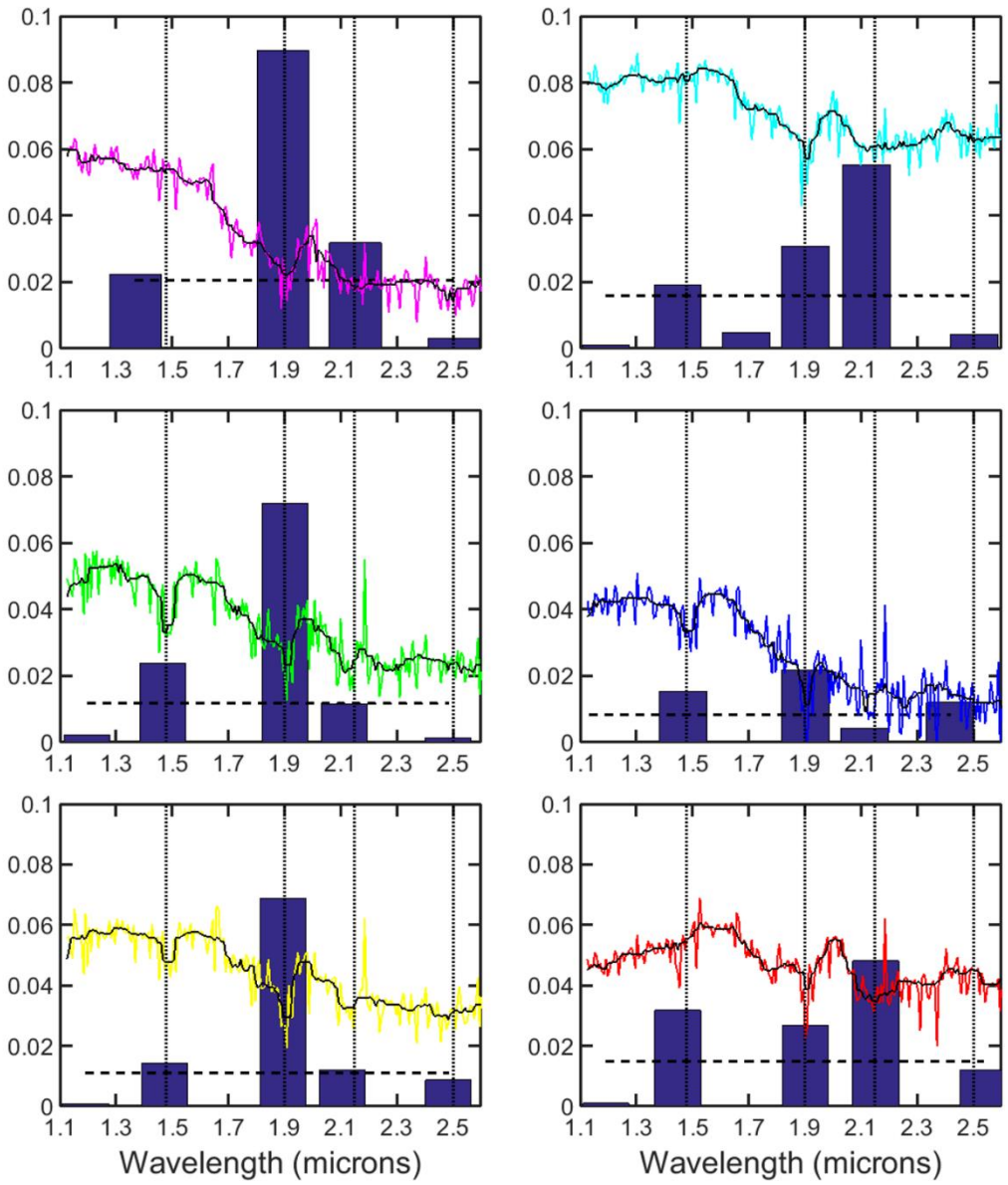

Figure 4.3. Signal verification for Palikir using band-detection algorithm. Each plot corresponds to one of the six pixels from Figure 4.1 where a hydration band is observed. The bars show areas of the detected bands at wavelengths of hydration combinations and overtones, where the y-axis shows area of the absorption band. The horizontal dashed lines show the mean of areas of all detected "bands" at any wavelength, which is taken to represent the noise threshold for band detection. The 4 vertical dotted lines mark the same wavelengths as Figure 4.1.

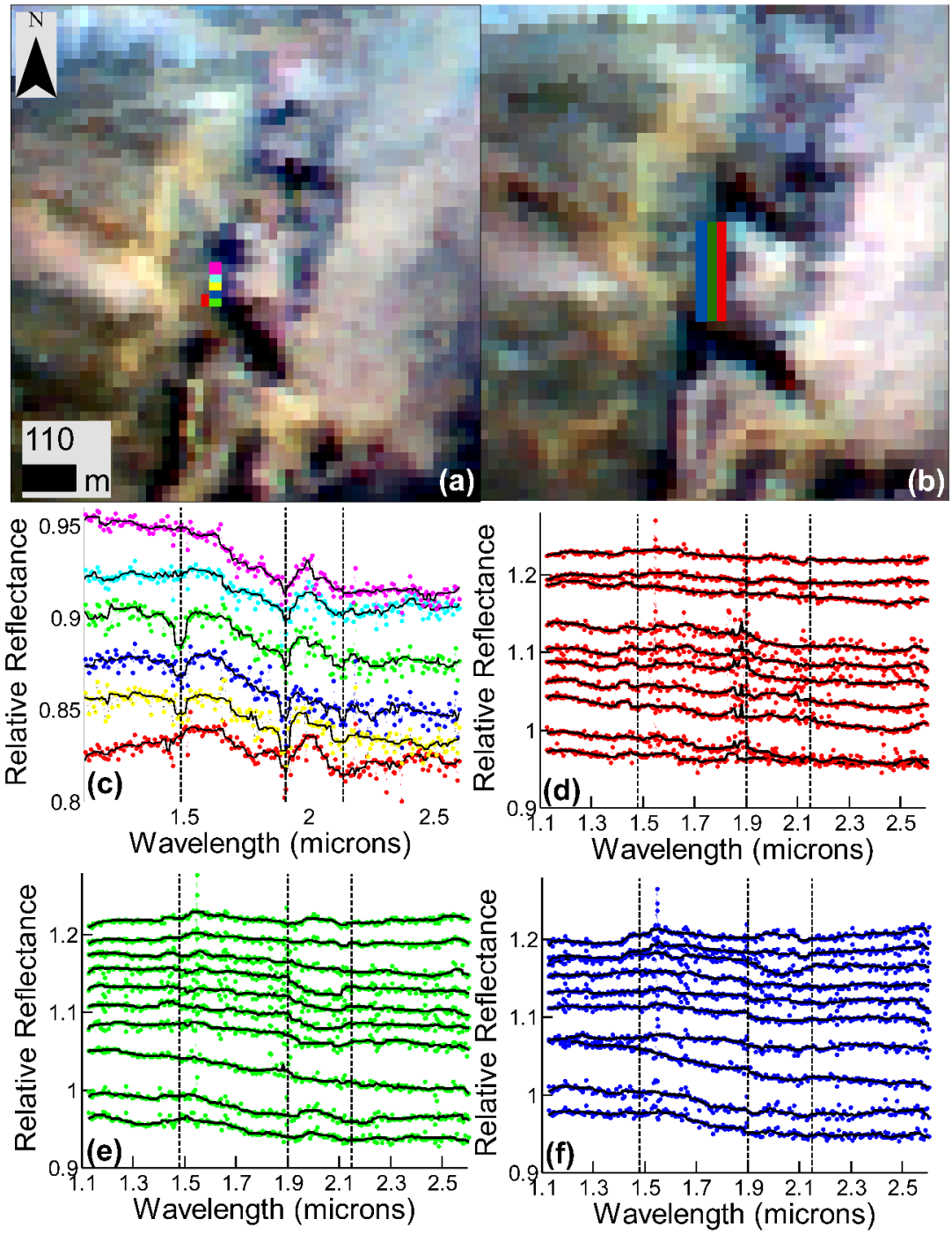

Figure 4.4. CRISM data of Palikir crater RSL from the same region but at two different times. **(a)** CRISM observation FRT0002038F of Palikir crater, and the six pixels where the hydration band is observed. **(b)** CRISM observation FRT0001E24D with regions of interest (red, green and blue pixels) shown, which was used to generate spectra. Scale and N-arrow for both (a) and (b) are the same. Both images use the same CRISM bands for the RGB as Figure 4.1b **(c)** Spectra from all the pixels shown in (a). **(d)** Normalized spectra

from all the red pixels in (b). **(e)** Same as (d) but for the green pixels. **(f)** Same as (d) for the blue pixels. All are shown ratioed to nearby non-RSL material.

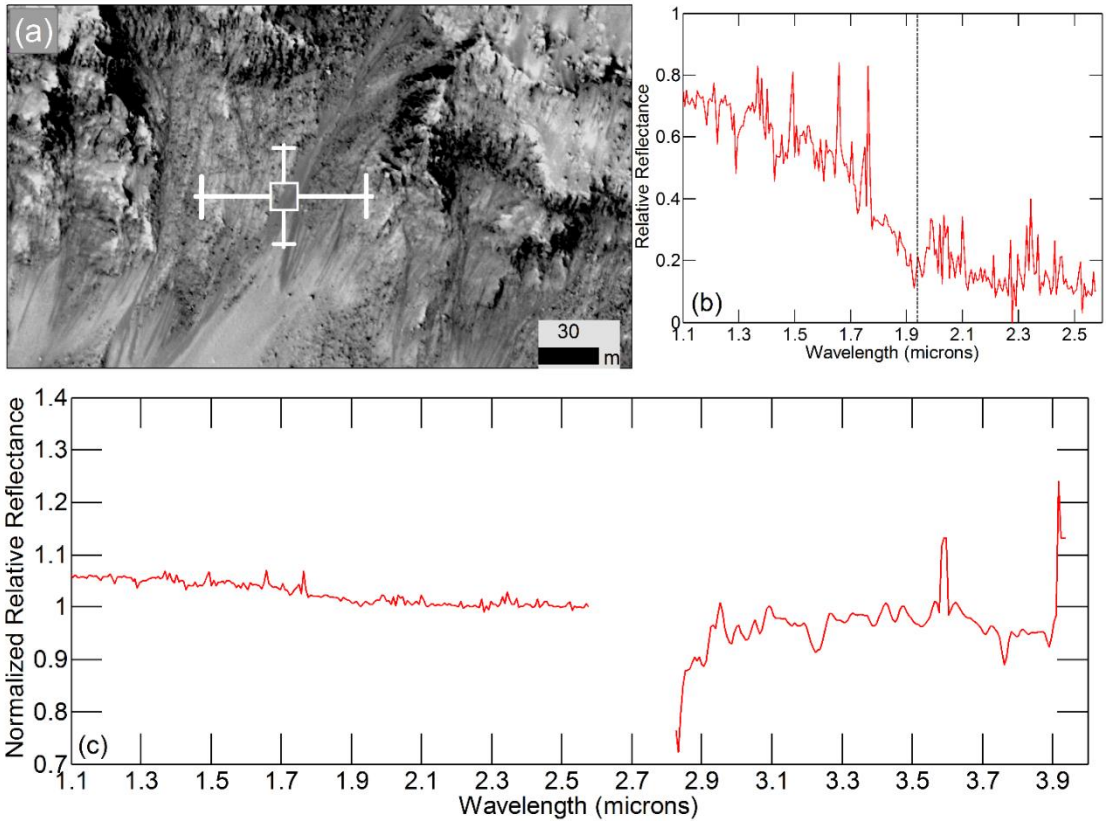

Figure 4.5. RSL in Palikir crater from MY 31 and its spectrum. **(a)** ESP_032381_1380 (Ls: 340, MY: 31): Orthorectified HiRISE observation of the same area as Figure 4.1 (a), but from a different Mars year showing the recurring aspect of RSL. White box with error bars showing the approximate location of the CRISM pixel analyzed. **(b)** CRISM spectrum of the regions seen in (a), ratioed to nearby non-RSL material. The red spectrum is from MY 31 of approximately the same spot (coordinated CRISM observation FRT00029F0C). (c) Same as (b), but the spectrum extends from 1.1 μm to 4.0 μm and is normalized to relative reflectance at 2.6 μm. A broad absorption at ~3 μm is clearly seen.

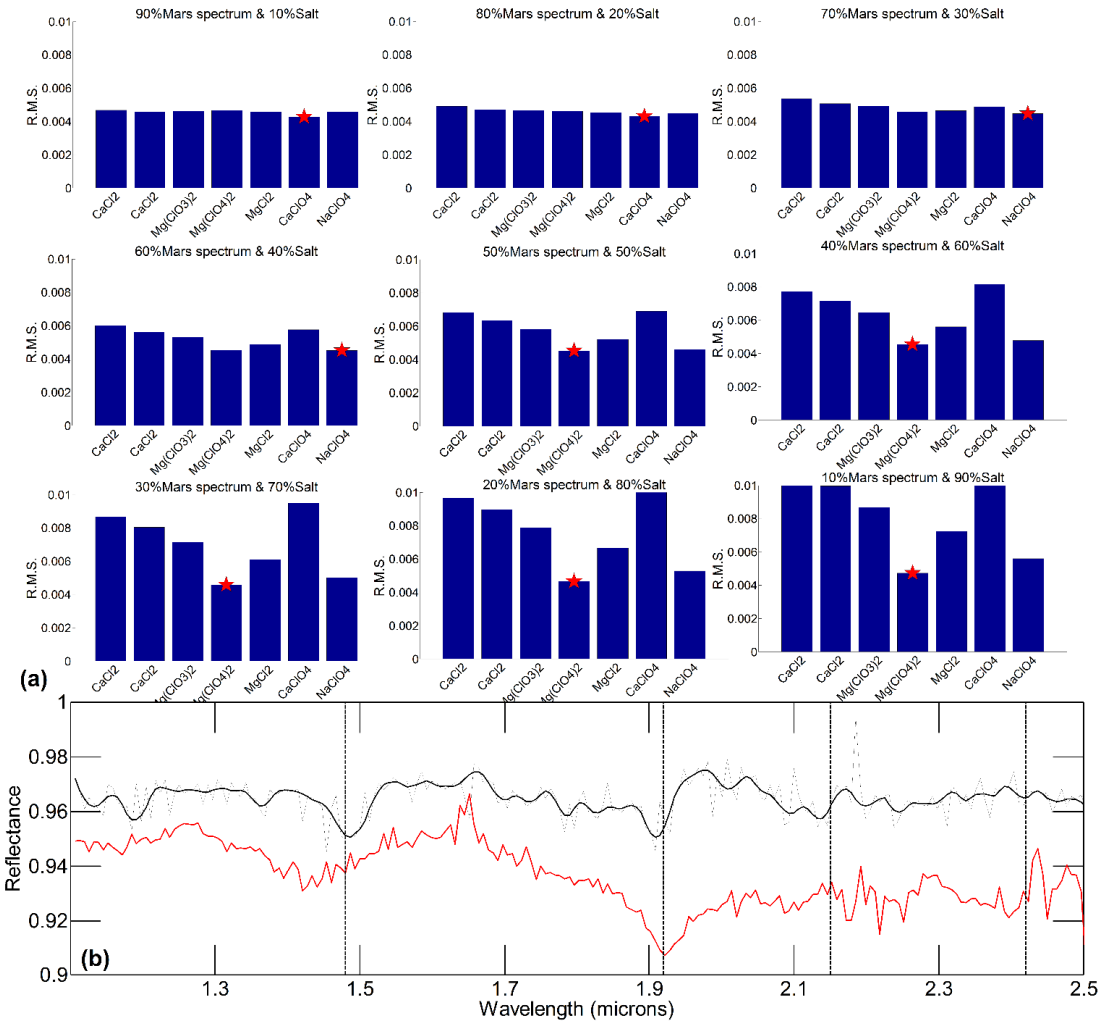

Figure 4.6. Misfit between Palikir RSL and laboratory spectra. **(a)** The nine plots here show the misfit between the observed spectrum and laboratory spectra of single salt species as a function of their proportions. The title of each slide reports the proportion of each spectrum used in the model. The Y-axis is the total root-mean square error between the two spectra. The X-axis corresponds to single salts used in the model. The bar with red star denotes the linear combination of the salt and Mars spectrum that results in the lowest misfit (i.e. best match). **(b)** Result from least-square regression analysis. The black spectrum is from Palikir crater, and the red laboratory spectrum is the best matched, which is a linear combination of the Martian soil (62%) and multiple salts (magnesium perchlorate (23.15%), chlorate (12.5%), and chloride (1.5%)). Perchlorates can explain the narrowness of the observed absorptions, but the inability to match the exact wavelength of the 1.48-µm band suggests the presence of an additional salt.

Coordinated HiRISE-CRISM observations of Horowitz crater in MY 29 show large RSL emanating from the central peaks (Figure 4.7). At two of the central peaks, we observed absorptions at 1.9 μm, 2.15 μm and 2.43 μm. A linear spectral mixture of Martian soil and Na-perchlorate (*Hanley et al.*, 2014; *Bishop et al.*, 2014) provided the best match to the observed spectra (Figure 4.2, Figure 4.9). The spectra reported here lack absorption features above the noise threshold at ~1.4 μm, but they do have broad ~3 μm absorptions consistent with hydration (Figure 4.10). The 1.9 μm and 2.15 μm absorptions are also present in the unratioed I/F spectrum (Figure 4.10).

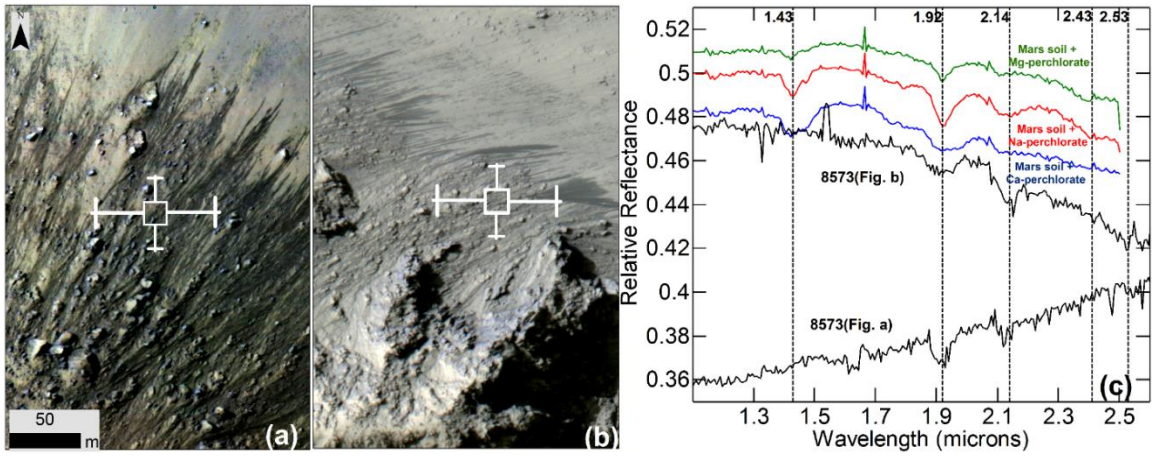

Figure 4.7. RSL activity in the central peaks of Horowitz crater and associated CRISM spectra. **(a)** RSL emanating from bedrock exposures at Horowitz crater's central peak. Part of HiRISE image PSP_005787_1475 (IRB) (L_s=334°, MY 28): **(b)** Same image as (a) showing RSL activity at a different part of the central peak (scale same as (a)). White box with error bars same as in previous figures. **(c)** Black spectra correspond to area in (a) and (b. Color spectra are results from spectral mixing between the Martian soil and a variety of salts (specified in the figure).

Some of the most intense RSL activity in the southern mid-latitudes occurs on the central peak structures of Hale crater (Figure 4.11). A HiRISE-CRISM coordinated observation was acquired during late RSL season (Figure 4.3, Table S4.1). Analysis of the CRISM data shows strong ~1.48 μm and 1.9 μm absorption features in the location where dense RSL activity is observed in the HiRISE image (Figure 4.11). Similar to Palikir, the presence of

narrow 1.48 μm and 1.9 μm absorption bands is consistent with a linear spectral mixture of Mg perchlorate and Martian soil.

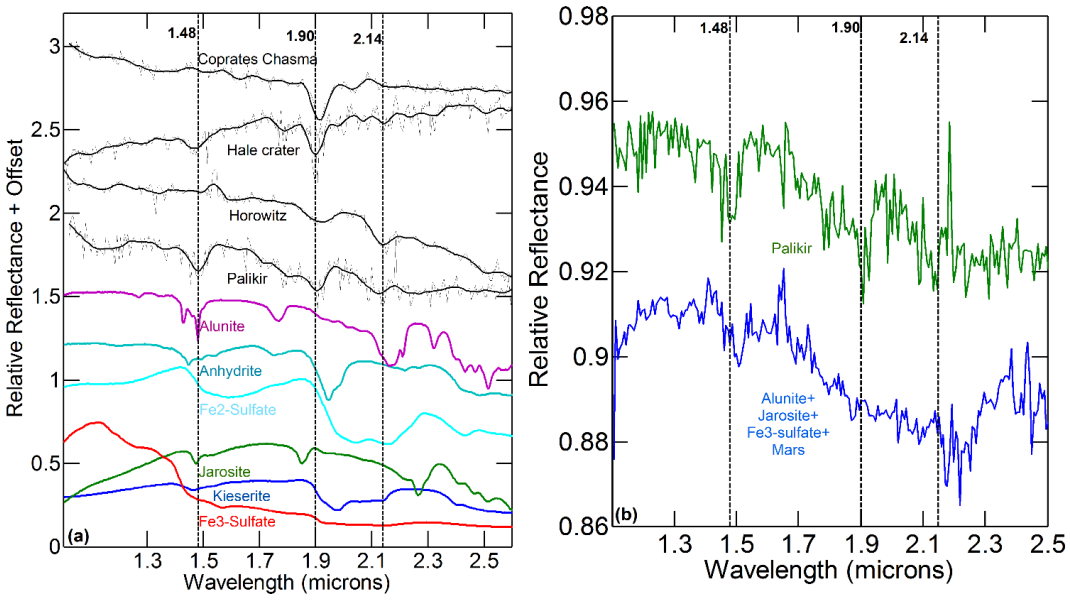

Figure 4.8. Spectra of various sulfates and RSL sites and result from linear spectral mixture. **(a)** Infrared laboratory spectra of various sulfates in color, and of the four RSL sites in solid black color lines. **(b)** The blue spectrum is the result from spectral mixing between alunite (11.56%), jarosite (26.78%), Fe3-sulfate (19%) and Martian soil (42.65%). The green spectrum is of Palikir crater for comparison.

In Coprates Chasma, RSL are abundant and in some cases entire fans associated with RSL are observed to change their reflectance (*McEwen et al.*, 2014) (Figure 4.12). Spectra of RSL fans in Coprates were analyzed, and we found multiple places in the CRISM images with 1.9 μm absorptions (Figure 4.12). Without detection of other absorptions, assignment to a particular salt mineralogy is not possible. The 1.9 μm absorption on the RSL slope suggests precipitation of salts and resulting modification of grain sizes as a viable mechanism for the change in albedo of the fans, and may also explain spectral changes previously reported on RSL fans (*Ojha et al.*, 2013).

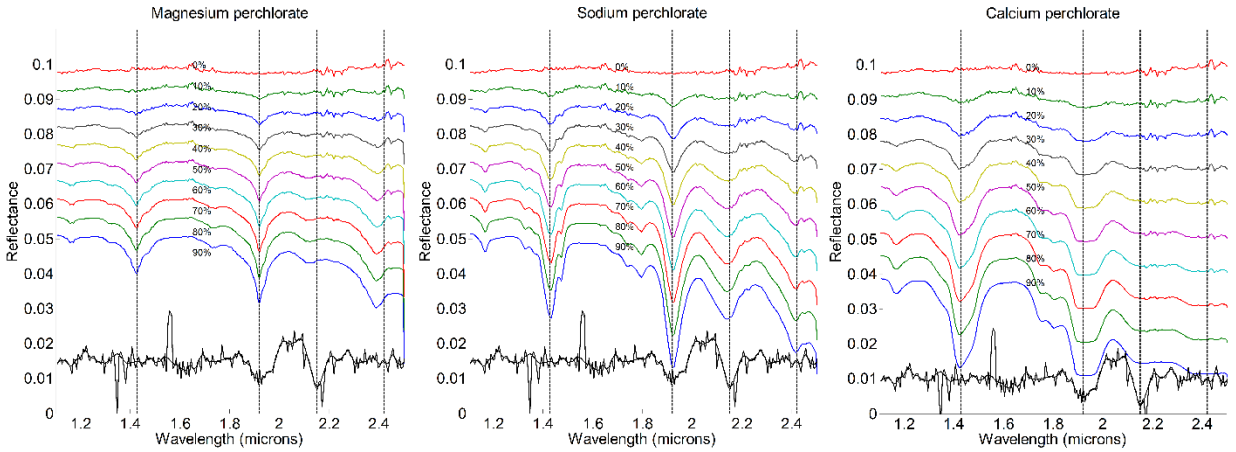

Figure 4.9. Linear spectral mixture result for Horowitz crater. The three plots show the Horowitz spectrum in black and results from linear spectral mixtures between Martian soil and various salts (specified in the title) as a function of the proportion. The text in black near each curve shows the proportion of the salt spectrum used in that model. A linear combination of sodium perchlorate and Martian soil is the only mixture that is able to recreate the shape of the 2.15 μm feature observed in the Horowitz RSL slope spectrum, but it predicts a stronger 1.4-μm absorption than is observed. Alternatively a non-perchlorate salt may be responsible for the 2.15-μm band.

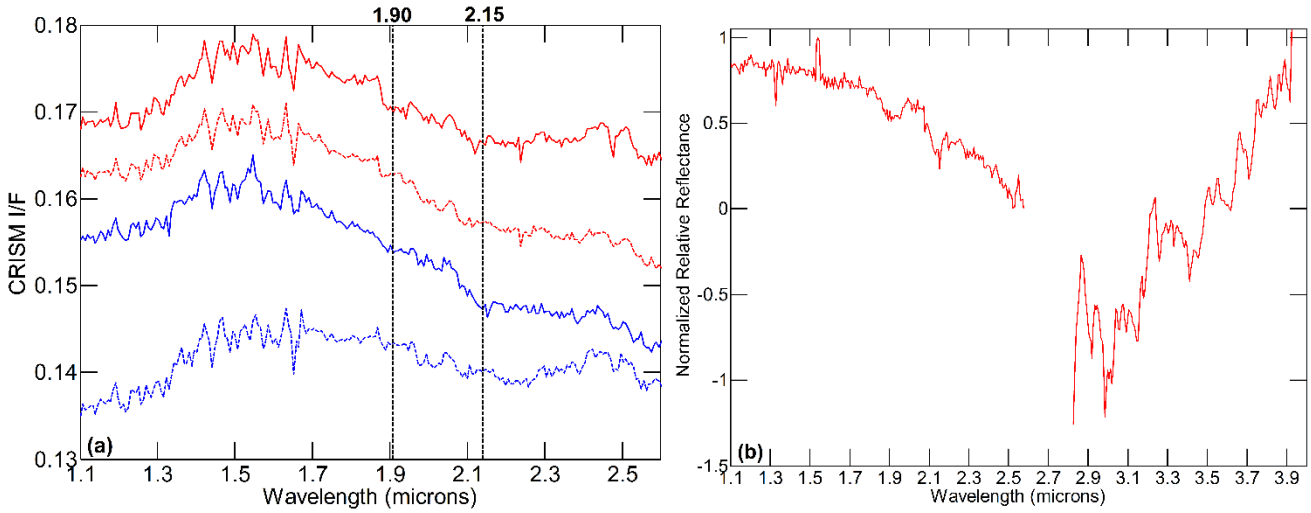

Figure 4.10. Spectrum of RSL slopes from Horowitz crater. (a) Spectra from FRT00008573 of RSL region in solid color lines and corresponding denominator areas in dashed color lines. (b) CRISM reflectance spectrum of the RSL pixels from FRT00008573, ratioed to nearby non-RSL material and normalized to relative reflectance at 2.6 μm, showing a deep absorption band at ~3 μm.

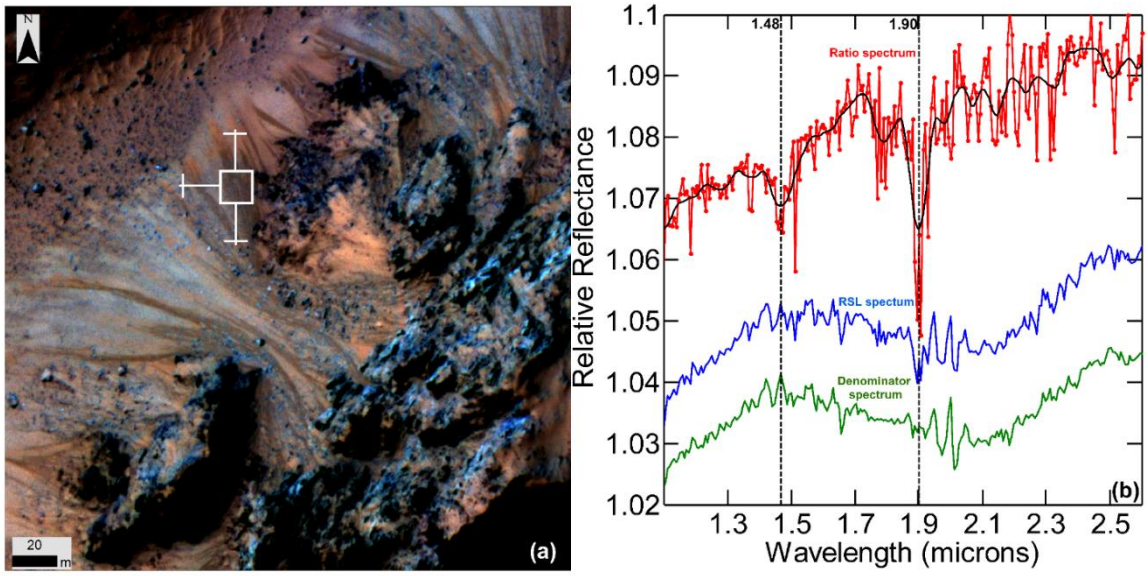

Figure 4.11. RSL emanating from a central peak in Hale crater and associated CRISM spectrum. **(a)** RSL on a central peak of Hale crater. Section of HiRISE image ESP_032416_1440 (IRB) (L_s = 342, MY 31): North is up and light is from the left. White box with error bars same as in previous figures. **(b)** IR spectrum from the RSL seen in HiRISE image. The symbols and the smoothing functions used are the same as in previous figures.

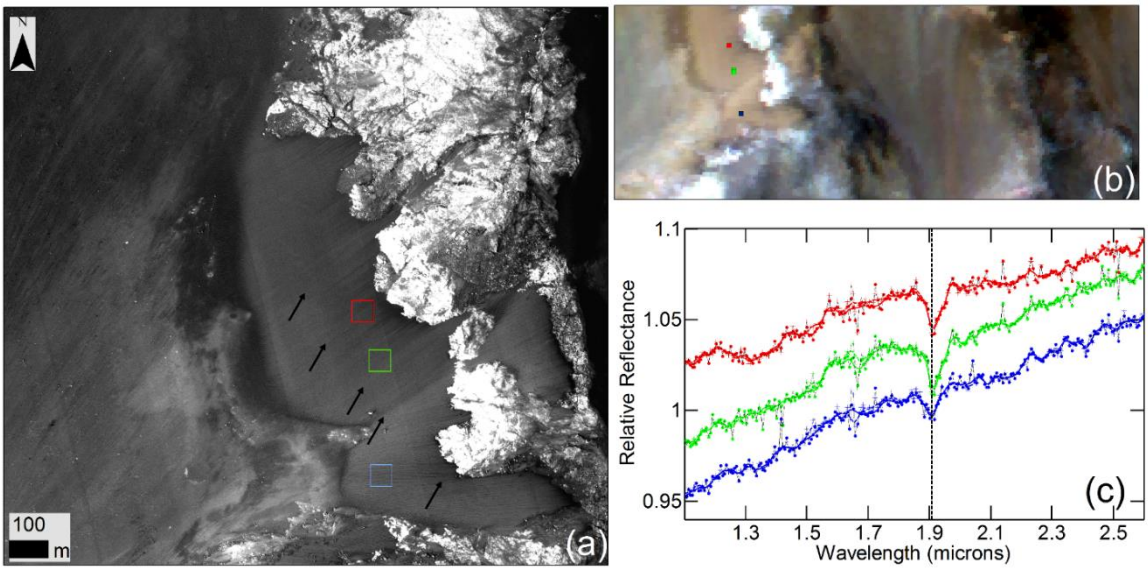

Figure 4.12. RSL and associated dark fans observed in Coprates chasma and associated CRISM spectra. **(a)** RSL emanating from bedrock exposures at Coprates Chasma. Dark fans associated with RSL are denoted by arrows. Various colored boxes show the approximate location of CRISM pixels shown in (b). Section of HiRISE image ESP_031019_1650 (L_s=279°, MY 31). **(b)** Areas analyzed in concurrent CRISM observation FRS00028E0A. Same RGB channels as were used in Figure 4.1b. **(c)** The spectra from the three colored pixels in (b) are shown ratioed to nearby non-RSL material.

4.4. Conclusion and Discussion

MRO's mid-PM (~3 pm) observations occur at the time of the day with lowest relative humidity (*Rummel et al.,* 2014), which minimizes the probability of detecting liquid brines that emplaced hydrated salts, and may even facilitate dehydration of salts. In all sites discussed here, we observe H_2O-related absorption features at 1.9 μm and 3.0 μm, but the OH-related ~1.4 μm feature is observed only in Palikir and Hale crater. Based on the widths and the band centers of the absorptions at 1.4 μm and 1.9 μm, an Mg-perchlorate, Mg-chlorate and Mg-chloride mixture was found to be the best match from our spectral mixture model (Figure 4.6). Based on spectral mixing models and absorption features at 2.15 μm and 2.43 μm, Na-perchlorate was found to be the best match at Horowitz (Figure 4.7). We also performed similar spectral mixing model with various sulfates, but found no good match (Figure 4.8).

The presence of perchlorates on the surface of Mars has been confirmed at Gale crater by Mars Science Laboratory (MSL), the northern plains by the Phoenix mission, and is suspected at the Viking landing sites (*Glavin et al.,* 2013; *Cull et al.,* 2010; *Navarro-Gonzalez et al.,* 2010) (Figure 4.13). At Gale crater, hydrated Ca-perchlorate is interpreted to be the best matching oxychlorine compound (*Glavin et al.,* 2013). Mg- and Ca-perchlorate were proposed as the most likely cation species of perchlorate at Phoenix landing site (*Glavin et al.,* 2013; *Cull et al.,* 2010; *Chevrier & Rivera-Valentin,* 2012). Additionally, thin films of water were hypothesized to have dissolved perchlorate from the surface to the subsurface and to have created concentrated patches at Phoenix landing site (*Hecht et al.,* 2009; *Cull et al.,* 2010). Re-interpretation of the Viking data also found Mg-perchlorate to be the most likely perchlorate species (*Navarro-Gonzalez et al.,* 2010).

These *in situ* perchlorate detections are consistent with our observation at RSL sites. Additionally, perchlorate and chlorate species have also been found in a Martian meteorite (*Elsenousy et al.,* 2015).

The origin of water forming the RSL is not understood (*McEwen et al.,* 2011; *McEwen et al.,* 2014; *Ojha et al.,* 2014). Water could form by the surface/sub-surface melting of ice, but the presence of near-surface ice at equatorial latitudes is highly unlikely (*Kounaves et al.,* 2014). RSL could form alternatively via deliquescence, but it is unclear whether the Martian atmosphere can supply sufficient water vapor every year to create RSL (*McEwen et al.,* 2014). Another hypothesis is seasonal discharge of a local aquifer, but lineae extending to the tops of local peaks (*McEwen et al.,* 2014) are difficult to explain. It is conceivable that RSL are forming in different parts of Mars via different formation mechanisms.

In all the sites reported here, we find evidence for hydrated salts on the RSL-containing slopes, supporting a genetic connection between the two. Na-perchlorate can lower the freezing point of water by up to 40 K, whereas Mg-perchlorate and Mg-chlorate can depress the freezing point even more by up to 70 K (*Chevrier et al.,* 2009; *Hanley et al.,* 2012; *Rummel et al.,* 2014). Mg-chlorate, Mg-perchlorate and Na-perchlorate monohydrate are also predicted to be the most likely salts to concentrate from evaporation of brine at the Phoenix landing site (*Chevrier & Rivera-Valentin,* 2012). Our observation of perchlorate could be due to liquid water in RSL dissolving perchlorates present in the soil and re-precipitating them in higher concentrations. Regardless, the spectral absorption of hydration bands at times and places when we observe maximum RSL activity implicates RSL as the source of hydrated salts.

These results strongly support the hypothesis that seasonal warm slopes are forming liquid water on contemporary Mars. The spectral identification of perchlorate in association with RSL also suggests that the water is briny and not pure. Terrestrially, in the hyperarid core of the Atacama Desert, deliquescence of hygroscopic salts offers the only known refuge for active microbial communities (*Davilla et al.,* 2008; *Davilla et al.,* 2013) and halophylic prokaryotes (*Aharon et al.,* 2014). If RSL are indeed formed as a result of deliquescence of perchlorate salts, they might provide transiently wet conditions near surface on Mars, although the water activity in perchlorate solutions may be too low to support known terrestrial life (*Rummel et al.*, 2014). The detection described here warrants further astrobiological characterization and exploration of these unique regions on Mars. This enhanced evidence for water flow also provides new clues to the nature of the current Martian hydrological cycle.

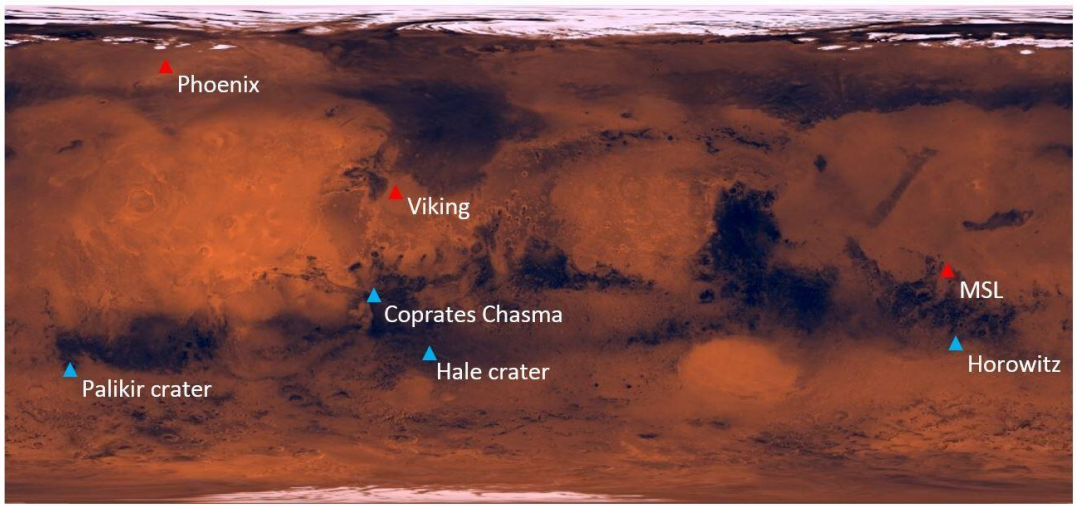

Figure 4.13. Distribution of sites where perchlorate has been detected. In red: in-situ detection of perchlorates via surface missions. In blue: Sites discussed in this paper. Background is colorized global Viking mosaic.

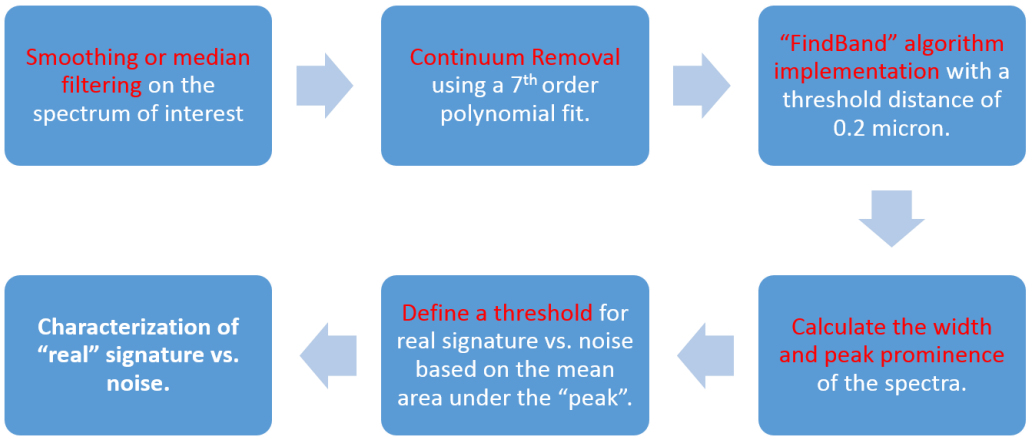

Figure 4.14. Flow chart for the band detection algorithm routine used in this study to elucidate signal from noise.

Chapter 5

Oxychlorine Salts in the Northern Mid-Latitudes of Mars: Implications for Ice Stability and Habitability

5.1. Summary:

Out of >500 known impact events that have been detected within the last ~10 years on Mars, 31 have ejected or exposed water-ice from the Martian sub-surface (*Daubar et al.*, 2016; *Dundas and Byrne*, 2014). Near-infrared spectroscopy near the water-ice-rich ejecta excavated by some of the largest new impact craters in the Martian mid-latitudes provides evidence for hydrated oxychlorine salts. Based on the observed spectral absorption features, the most likely oxychlorine salts are perchlorates and/or chlorates. The source of these oxychlorine compounds (regolith vs. precipitation from ice) is unknown, but their presence helps to explain the long-term stability and widespread distribution of mid-latitude ice on Mars. Additionally, this result further corroborates the important role oxychlorine salts play in the contemporary Martian hydrological cycle.

5.2. Introduction:

Characterizing the volume and geographic distribution of water-ice on Mars is critical for understanding the Martian paleoclimate, ice-emplacement history, and potential for habitability. Numerous geomorphic features in both hemispheres of Mars provide evidence for a recent ice age (within the last few million years) *(Head et al., 2003; Mustard et al.,* 2001). The near-surface hydrogen abundance data from the Gamma Ray Spectrometer (GRS) have provided evidence for large amounts of water-ice poleward of $\pm$ 60° latitudes(*Boynton et al.,* 2002). Additionally, from repeat imaging from high-resolution cameras in Mars orbit, over 500 new impact craters formed during the era of spacecraft exploration have been discovered (*Daubar et al.,* 2016), of which 31 (Table S5.1) have been observed to excavate shallow sub-surface ice at middle (as low as 39°N, and 56°S) and high latitudes of Mars (*Byrne et al.,* 2009; *Daubar et al.,* 2013; *Dundas and Byrne,* 2014). Collectively, these lines of evidence point to the widespread distribution of shallow (*Dundas and Byrne,* 2014) (0.25 m - 2 m) subsurface ice at mid-latitudes of Mars. This is excess ice—far exceeding the pore space—likely >99% pure, although likely vertically and laterally heterogeneous.

The depositional history of the mid-latitude ice is largely unknown, but "expanded" craters in Arcadia Planitia suggest that deposition of the excess mid-latitude ice may have occurred more than 10 million years ago (*Viola et al.,* 2015). This observed long-term

stability of mid-latitude ice is inconsistent with Martian climate models that predict complete sublimation of ice on much shorter time scales (*Dundas and Byrne,* 2014; *Mellon et al.,* 2004). Furthermore, at some of the low-latitude sites (e.g. site III at 39°N, (Table S5.1, Table S5.2)), mean atmospheric water content twice the current value is required to explain persistent stability of shallow sub-surface ice (*Dundas and Byrne,* 2014). Higher near-surface humidity(*Zent et al.,* 2010) and/or reduction of water vapor pressure by deliquescent salts(*Chevrier and Rivera-Valentin,* 2012; *Hudson and Aharonson,* 2008) have been proposed as additional factors that can aid in the long term stability of ice in the Martian shallow sub-surface. It is possible that ice is currently unstable in the Martian near-surface and is sublimating slowly, and/or that the long term average atmospheric water content is higher than currently observed.

Hygroscopic (i.e. able to absorb moisture from the air) salts intermixed within the regolith can reduce the diffusivity of water (*Hudson and Aharonson,* 2008; *Hudson et al.,* 2007) vapor due to sublimation of sub-surface ice by a factor of 10. Additionally, in the case of salty ice, the sublimation rate would be even lower since the ice would first melt and then possibly evaporate (*Chevrier and Rivera-Valentin,* 2012). In the presence of hygroscopic salts, the vapor pressure is reduced in proportion to the water activity, which reduces the rate of either sublimation, or evaporation. Ice is stable when its mean vapor pressure is less than or equal to that in the atmosphere, so reduction in the vapor pressure by deliquescent salts at sites in the mid-latitudes would greatly increase the stability of ice.

Deliquescent salts—in particular, perchlorates (*Gough et al.,* 2014; *Nuding et al.,* 2014)—have been identified in-situ by landers (*Hecht et al.,* 2009; *Navarro-González et al.,* 2010), the Curiosity rover mission (*Glavin et al.,* 2013), and they were recently confirmed to occur in recurring slope lineae (RSL) (*Ojha et al.,* 2015) in the southern and equatorial regions of Mars (*McEwen et al.,* 2013, 2011; *Ojha et al.,* 2014). The Phoenix mission found that high-latitude soil contains as much as 0.6 wt% perchlorates (*Hecht et al.,* 2009), orders of magnitude greater than natural concentrations in any terrestrial deserts.

In this work, we analyzed coordinated observations from High Resolution Imaging Science Experiment (HiRISE) and Compact Reconnaissance Imaging Spectrometer for Mars (CRISM) of impact-excavated icy ejecta to seek evidence of deliquescent salts that may aid in the long-term stability of ice on Mars.

5.3. Methods:

Methodology previously employed to find evidence of hydrated salts in Recurring Slope Lineae (RSL) (*Ojha et al.,* 2015) was used in this study. PDS-released CRISM I/F images were used to analyze the spectral characteristics of impact-excavated ice and nearby surroundings. ENVI's (Exelis Visual Information Solutions) CRISM Analysis Tool (CAT) (*Murchie et al.,* 2007) was used to normalize atmospheric absorptions. Median spectra from each column of pixels were used to normalize and create a ratio image. The pixels whose spectra we present here were found via manual and automated inspections of the ratio image. PDS-released HiRISE images were downloaded and no further processing was performed for this work. CRISM images were manually georeferenced to the HiRISE

images to locate the pixels of interest. For laboratory spectra of ice and perchlorate presented here, we produced the ice via condensation of liquid water on a cooled metal plate (*Dupire et al.,* 2009). It was then crushed to obtain grain sizes between 500 and 600 μm, and placed in a liquid nitrogen cryostat (MicrostatN, Oxford Instruments) to reproduce the Martian pressure and temperature conditions (less than 10 Mbar, 250-290 K). Spectra were acquired with a Nicolet 5700 Fourier Transform Infrared Spectrometer, which collects 4149 spectral channels from 1 to 5 μm. Detailed information on our methodology can be found in the supplementary materials.

Coordinated CRISM and HiRISE observations were used to examine the spectral and geomorphic characteristics of icy ejecta excavated by impact events. HiRISE color and red images were downloaded from the PDS and visually inspected to find the location and extent of the icy ejecta (e.g. Figure 5.4). Besides manual color and contrast adjustment, no further processing was applied to HiRISE images. Coordinated (i.e. acquired at the same time with HiRISE) CRISM full-resolution targeted (FRT ~18 m/pix), full-resolution short (FRS ~18 m/pix), and half-resolution short (HRS ~36 m/pix) observations at Infrared (IR: 1.0-3.9 μm) wavelengths were used to examine the spectral characteristics of the icy ejecta. The details of the HiRISE and CRISM images, including observations IDs, central latitude/longitude and the acquisition times, are listed in Table S5.2.

ENVI's (Exelis Visual Information Solutions) CRISM Analysis Tool (CAT) was used to import the PDS-released CRISM images, and to reduce atmospheric effects. Multiple variants of the 'volcano-scan' approach were used to normalize the atmospheric gas absorptions (e.g. Figure 5.15 and Figure 5.16). To assess the effect of artifacts from

the volcano-scan observations on the normalizing procedure (Figure 5.15), we computed the standard deviation in the reflectance value as a function of wavelength:

$$\sigma = \sqrt{\frac{1}{N}\sum_{i=1}^{N}\left(R_i - R_{avg}\right)^2}$$

where σ is the standard deviation, N is the number of 'volcano-scan' variants used, R_i is the reflectance at each wavelength, and R_{avg} is the average reflectance value at a particular wavelength from N different 'volcano-scan' normalizations. The image was further normalized by dividing the value at each wavelength in a given detector column by the median value at that wavelength over the entire detector column. This normalization led to reduction in systematic detector related noise, and thereby increased the depth of hydration absorption bands relative to noise.

A band-detection algorithm, previously used to find hydration absorption bands on RSL slopes, was used to complement our visual search for absorption bands around the icy ejecta. Once spectral absorption band of interest were found, we used a local regression linear least square 2nd order polynomial filter that assigns zero weight to data outside six mean absolute deviations to smooth out isolated spikes and high-frequency noise (e.g. Figure 5.1 – Figure 5.3). Numerous previous works have used band-depth parameter maps to isolate areas with specific absorption bands of interest. In our case, the spectral absorption bands are isolated to very few pixels, so band-depth parameter maps were ineffective in illustrating this as they are sensitive to spikes and noise. We, therefore, used ENVI's Multi Range Spectral Feature Fitting (SFF) tool to identify any other areas in the image with similar absorption features. SFF locates pixels in a given image with similar

spectral absorption features to the ones input by the user and outputs a classified image with the root-mean-square (RMS) difference between the input spectrum and each pixel investigated. We manually inspected each pixel with RMS less than 10% and found a spike at ~2 μm to be the reason for most false positives (Figure 5.7). Other than that, we found no other pixels in any analyzed scene with similar absorption features to the ones we report in this work. Spectral mixture models were created via mixture of laboratory spectra of various perchlorate salts and reference spectra from the CRISM scene[4].

Multiple laboratory experiments were conducted to explore the timing of hydration/dehydration cycles of perchlorates under Mars-like conditions. Sodium perchlorates monohydrates (99% purity) were used for the simulation. In the first simulation, we conducted dehydration experiments by filling a ~2-cm sample vial with sodium perchlorate at ambient conditions. The samples were then placed in a liquid nitrogen cryostat (MicrostatN, Oxford Instruments) to reproduce the Martian pressure and temperature conditions (less than 10 Mbar, and 250 to 290 K). The spectra of the samples were acquired with a Nicolet 5700 Fourier Transform Infrared Spectrometer, which collects 4149 channels from 1 μm to 5 μm. We observed dehydration (deduced through a reduction in band-depths of the 1.4 μm, 1.9 μm, and 3 μm features) within a few hours at 260 K.

We also ran multiple experiments to explore the hydration cycle of sodium perchlorates. Pure water ice and perchlorate-briny ice (i.e. solution of pure water and perchlorate frozen at temperatures below their eutectic) were produced via condensation on a cooled metal plate. The ice layer was added to the sample vial and overtopped with sand-sized quartz. The top layer of the vial (on top of the sand-size quartz) was filled with

perchlorate (Figure 5.17). The sample was placed under Martian conditions (i.e. P < 10mbar), and the temperature was slowly increased with a 5-minute pause interval for the acquisition of spectra (Figure 5.19). As the temperature slowly increased, ice began sublimating and perchlorates absorbed the water vapor. We observed perchlorates adsorbing water via the increase in the band-depth of the hydration features (Figure 5.19). Once temperature exceeded the eutectic point of the perchlorate, complete deliquescence and a phase transformation occurred, such that we observed liquid water spectra (Figure 5.19; lines corresponding to T = 263 K - 283 K). As temperature further increased, the water evaporated and the spectrum of hydrated perchlorate was observed again.

5.4. Results:

At Site-I (55.6°N, 150.6°E) , an impact crater ~5 meters in diameter excavated to a depth of ~50 cm in the northern mid-latitudes of Mars and excavated ice in its ejecta (*Dundas and Byrne,* 2014) (Figure 5.1, Figure 5.4). A coordinated CRISM image was analyzed, and the CRISM pixels overlapping the bright materials exhibit absorption features at ~1.25 μm, 1.5 μm, 2.0 μm, and ~3 μm (Figure 5.1, Figure 5.5, Table S5.2), indicative of water ice (*Clark,* 1999). In one pixel south of the impact crater, absorption bands at 1.45 μm, 1.91 μm, 2.14 μm, and 3.0 μm are observed (Figure 5.1, Figure 5.5). Liquid water and minerals containing water molecules have absorption bands near ~1.4 μm, ~1.9 μm, and 3.0 μm, with the wavelengths of their minima and their band widths and relative depths varying with the minerals hosting the molecular water and the magnitude

of hydration(*Clark,* 1999). Additionally, hydrated minerals can have cation-related combination or overtone absorptions at other wavelengths ranging from 1.7 μm to 2.4 μm, and typically lack the broad absorption band at 1.2 μm observed for ice.

Neither ice nor dry basaltic regolith has the observed narrow absorption band at 2.14 μm; thus, spectral mixtures of ice and dry regolith are unable to reproduce this absorption (Figure 5.6 (a) & Supplementary Information). Hydrated perchlorates, especially sodium perchlorate, have a distinct absorption band around 2.14 μm (*Hanley et al.,* 2015) (Figure 5.1), and are able to recreate the absorption at 2.14 μm through a linear spectral mixture of laboratory sodium perchlorate and Martian soil (Figure 5.6). Additionally, the strength of the 3 μm band in the hydrated perchlorate is comparable to that of ice suggesting a high degree of hydration (Figure 5.5). Systematic noise in CRISM data can create absorption-like features, so we examined other pixels within the scene for similar absorptions (Supplementary Information). An automated algorithm designed to find pixels with absorptions of interest was unable to find other pixels in the scene with matching bands at 1.4 μm, 1.9 μm, 2.14 μm, and 3 μm (Figure 5.7).

Two subsequent coordinated HiRISE and CRISM observations of this site were analyzed. HiRISE images show only very minor differences in the distribution and volume of ice in the ejecta between the three observations (Figure 5.8); CRISM observations however show subtle changes in the brightness and areal distribution of the icy ejecta

(Figure 5.9), and neither of the later images show absorption bands at 2.14 μm around the ejecta (Figure 5.10). The absorption bands attributed to impact excavated water-ice were also weak and barely detectable above the noise in the later images (Figure 5.10), so either (i) atmospheric haze or accumulated surface dust (ii) or spectral mixing and signal being split between pixels precluded detection of both ice and hydrated salts in the later CRISM images.

An impact crater 20 meters in diameter excavated ice from a depth of up to roughly 2 meters at Site-II (44.2°N, 164.2°E) (Figure 5.2, Figure 5.7). Coordinated HiRISE and CRISM images of this site were analyzed, and where bright materials are observed, we observe spectral absorption bands at 1.25 μm, 1.5 μm, 1.95 μm and 3 μm, indicative of water ice (Figure 5.2, Figure 5.11). In one pixel north of the impact crater absorption bands at 1.95 μm, 2.14 μm, and 3 μm are present, implying the presence of hydrated minerals on the surface, similar to Site-I (Figure 5.2 and Figure 5.11). In three pixels west of the impact crater, where no ice is observed, absorption bands at 1.95 μm, 2.19 μm, and 3 μm are present. Several chlorite, chlorate, and perchlorate salts have an absorption band at ~2.19 μm(Hanley et al., 2015) (Figure 5.12). Hydrated silica (*Milliken et al.*, 2008) also has an absorption band near 2.2 μm, but the minima for both the ~1.9 and ~2.2 μm bands are more consistent with oxychlorine compounds (Figure 5.12).

Two other coordinated HiRISE/CRISM images of Site-II were analyzed and neither absorption bands for ice nor hydrated minerals were observed. HiRISE images show that

a significant fraction of the ice had sublimated away prior to acquisition of the third image (Figure 5.13). Therefore, the lack of detection of ice and hydrated minerals in the latter images could be due to sublimation of the ice and dehydration of hydrated minerals (Supplementary Information). Additionally, the second CRISM observation of Site II was acquired at half-resolution (~36 m/pix), so significant spectral mixing could have obscured the detectability of remnant icy or hydrated areas.

Site-III (39°N, 190°E) is the lowest latitude site with impact-excavated ice(Daubar et al., 2013; Dundas and Byrne, 2014), and it hosts a cluster of craters (largest ~12 meters) within a wider blast zone (Figure 5.3, Figure 5.4). Ice is mostly visible inside the craters, with only traces present in the ejecta. In the coordinated CRISM image, we observe a few pixels with absorption bands at 1.95 μm, 2.13 μm and 3.0 μm (Figure 5.3, Figure 5.14). Unlike Site-I, the 1.45 μm absorption band is much weaker or absent, implying lesser hydration of the oxychlorine compounds (*Hanley et al.,* 2015; *Ojha et al.,* 2015). The presence of a 2.13 μm band and its strength relative to the 1.95 μm band is most consistent with hydrated sodium perchlorate (similar to Site-I & Site-II); however, the presence of hydrated perchlorates, chlorates or chlorides with other cations is possible.

5.5. Discussion

The presence of 2.13 μm absorptions in addition to absorptions due to molecular water at ~1.4 μm, 1.9 μm and 3 μm surrounding the sites investigated here implies the presence of hydrated oxychlorine compounds on the surface. At all sites, the presence of a 2.13 μm absorption band is most consistent with one or more hydrated oxychlorine compounds, especially sodium-perchlorate; presence of other chlorinated species is possible. At Site-II, few pixels also have absorption band at 2.19 μm band similar to various

chlorates and perchlorate species, however the presence of 3 μm band at Site-II rules out any anhydrous oxychlorine compounds. Without any other distinct absorption band, robust identification of the minerals at site-II with 2.19 μm band is not possible. Hydrated silica also has an absorption band at 2.2 μm, but its band minimum is less consistent with the Martian feature than is the minimum in some chlorine compounds (Figure 5.12). Hydrated sodium chlorate hexahydrate also has an absorption band near ~2.2 μm, and could be present with sodium perchlorate at Site-II. The atmospheric correction process for CRISM scenes (see Methodology & Supplementary Information) can sometimes create spurious absorption-like features; therefore we excluded this type of artifact by performing multiple "volcano-scan" observations to divide out atmospheric gas contributions, and confirming that they do not create the observed absorptions (Figure 5.15, Figure 5.16). Regardless of the volcano-scan observation used for atmospheric correction, the absorption bands discussed here are present in all the corrected images, and even also in those without any atmospheric correction (Figure 5.15). The spectra of ice reported here were extracted from only a few pixels, and yet clearly show absorption bands related to water (Figure 5.5, Figure 5.11, Figure 5.14), demonstrating the potential of single pixel spectra for elucidating small-scale compositional anomalies on Mars. The spectra of oxychlorine salts reported here also have a deep 3 μm band comparable to that of the water ice, indicating a fairly high degree of hydration.

The detection of the hydrated oxychlorine species was also possibly transient, with absorptions due to hydration not observed in later observations of the sites described here (e.g. Figure 5.10). Rapid dehydration of the hydrated minerals could have led to null detection in the later images, as suggested by laboratory experimental data in which

hydration/dehydration cycles completed within hours (Figure 5.17-Figure 5.19 & Supplementary Information). However, in Site-I and Site-II, ice was undetectable in the later CRISM observations even though bright material was visible in the coordinated HiRISE images (e.g. Figure 5.8), underlining the possibility of non-detection due to the signal being split between pixels and lost by spectral mixing. Additionally, hazy atmospheric conditions (yielding noise issues in the CRISM spectra) combined with rapid dehydration (e.g. Figure 5.18), made worse by possible dust masking (e.g Figure 5.10), could all be reasons for null detection in the later images.

The detection, albeit transient, of oxychlorine compounds in the vicinity of impact-excavated ice raises questions about their source(s) of the chlorinated phase. In all cases reported here, the absorptions were found within ejecta of the craters, suggesting that impact excavation played a key role in our ability to detect the chlorinated phase (Figure 5.4). Two possibilities exist: (i) anhydrous oxychlorine compounds are present in the Martian regolith, and reaction with impact ice hydrated them briefly at the time of our detection, or (ii) ice at the Martian mid-latitudes is salty, and hydrated oxychlorine compounds represent a residue of precipitated salts after sublimation of the ice. CRISM images of impacts with no excavated ice were analyzed, but evidence for hydrated salts were not observed, implying that ice helps hydrate the salts on the Martian surface. Atmospheric water may also be further aiding in the hydration of the excavated salts. The widespread detection of oxychlorine species on the surface of Mars (*Glavin et al.,* 2013; *Hecht et al.,* 2009; *Navarro-González et al.,* 2010; *Ojha et al.,* 2015) is consistent with the first scenario, in which excavated ice hydrates oxychlorine species already present in the regolith. At the Phoenix and Curiosity landing sites, perchlorates were thought to play a

major role in absorbing the atmospheric water vapor (*Martín-Torres et al.,* 2015; *Zent et al.,* 2010). Phoenix found that the Martian soil contained ~1% perchlorates, and in either hexahydrate or octahydrate state they can take up and release more water than is in the peak column density in the entire atmosphere (*Hecht et al.,* 2009). The time-varying cohesiveness of the soil at the Phoenix landing site may also be explained by a related mechanism, in which exchange of water vapor between buried ice and overlying perchlorate-rich soil may wet soil with a eutectic solution at certain temperatures (*Hecht et al.,* 2009). Deliquescent salts would effectively reduce the water vapor pressure, and intermixture of salt and regolith would also reduce the diffusivity of water vapor by up to an order of magnitude (*Hudson and Aharonson,* 2008).

Another possibility is that the shallow ice in Martian mid-latitudes is not pure, but is frozen brine. The oxychlorine compounds would thus be a lag deposit from ice sublimation, similar to the origin hypothesized for the gypsum and possible perchlorates in the sublimation residue of the north polar layered deposits (*Massé et al.,* 2012, 2010). At Site-III, surface temperature can exceed 273 K for hours daily during the northern-summer (Figure 5.20). Over geological time scales, ice at this site should have sublimated given current conditions, yet the presence of shallow sub-surface ice implicates an additional factor that is aiding in the long term stability of ice. If the ice in Site-III is salty and perchlorate-bearing, then it would form a eutectic melt rather than sublimating directly (*Chevrier and Rivera-Valentin,* 2012), and only slowly evaporate due to reduced vapor pressure, thus prolonging ice stability under present day Martian conditions (e.g. Figure 5.19).

Detection of the oxychlorine species in ejecta of icy craters helps to explain the stability of ice in the northern mid-latitudes of Mars over millions of year timescales. Furthermore, it supports the idea that oxychlorine species play a pervasive role in the contemporary Martian water cycle. So far, in every instance where evidence of potential water (liquid or ice) at low to mid latitudes on Mars has been detected, perchlorates appear to also be present (*Hecht et al.,* 2009; *Ojha et al.,* 2015; *Zent et al.,* 2010). This association may have implications for potential current habitability of the Martian surface. If perchlorates were also involved in the water cycle on early Mars, as suggested by their presence in late Noachian sedimentary rocks of Yellowknife Bay (*Ming et al.,* 2014), deposited billions of years ago and buried until recently (*Farley et al.,* 2013), then estimating their paleo-concentrations relative to known toxicity limits for life on Earth may be critical to understanding where ancient Mars was habitable. Widespread perchlorates may also challenge our ability to characterize some organic species *in situ* via traditional pyrolysis experiments (*Glavin et al.,* 2013) because of their reactivity with organics; at the same time, O_2 release upon their pyrolysis could be a potential resource for future human explorers. Further characterization of the oxychlorine speciation, which likely varies from region to region as suggested by the spectral differences observed between sites (Figs. 1-3), will be important for determining the temperatures and concentrations at which O_2 would be liberated from these minerals, and for fully understanding what each assemblage implies about the environment in which it formed.

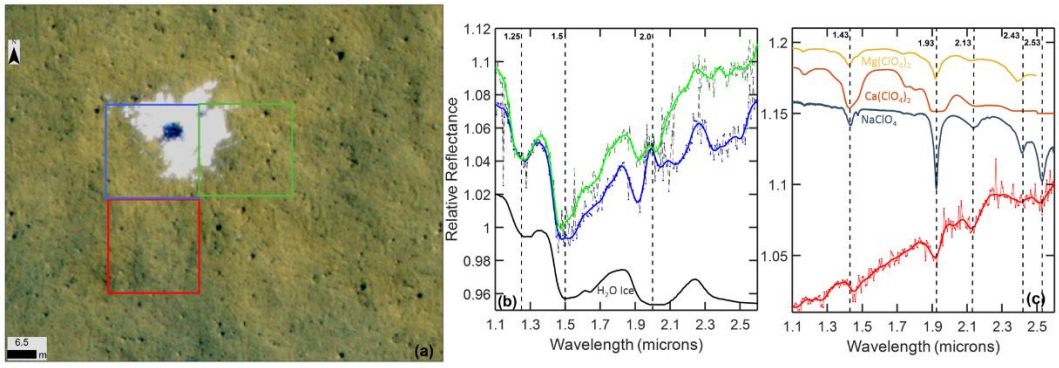

Figure 5.1. Impact-excavated ice and associated CRISM spectra at Site-I. (a) HiRISE image PSP_010625_2360 (Infrared-Red-Blue/Green - IRB) showing impact-excavated ice and surroundings. Colored boxes show estimated locations of the individual pixels examined in CRISM image FRT0000D2F7. (b) Spectra from the green and blue colored pixels shown in (a). Observed reflectances, ratioed to a nearby bland region in the same detector column, are plotted using dashed lines; data smoothed using a 7-element boxcar are shown in solid color. A laboratory spectrum of water ice is shown in black. (c) The smoothed ratio spectrum from the red colored pixel shown in (a). Laboratory spectra of various perchlorates (monohydrates) are labeled.

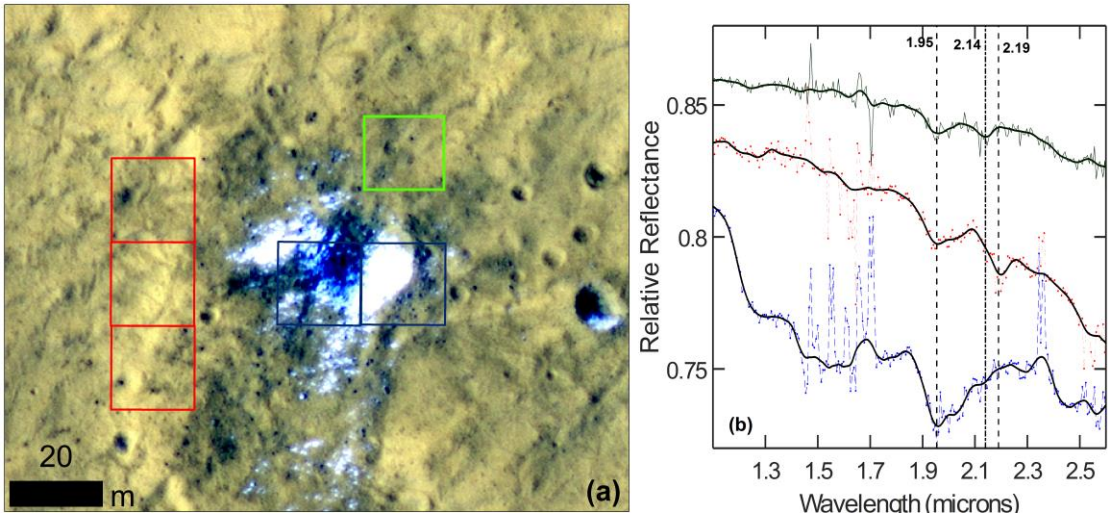

Figure 5.2. Impact-excavated ice and associated CRISM spectra at Site-II. (a) HiRISE image ESP_016954_2245_IRB showing impact-excavated ice and surroundings. Colored boxes show estimated locations of the CRISM pixels (FRT0001719F). (b) Spectra from the red, green and blue colored regions shown in (a). The observed data are plotted in colored dashed lines and the smoothed data in solid black.

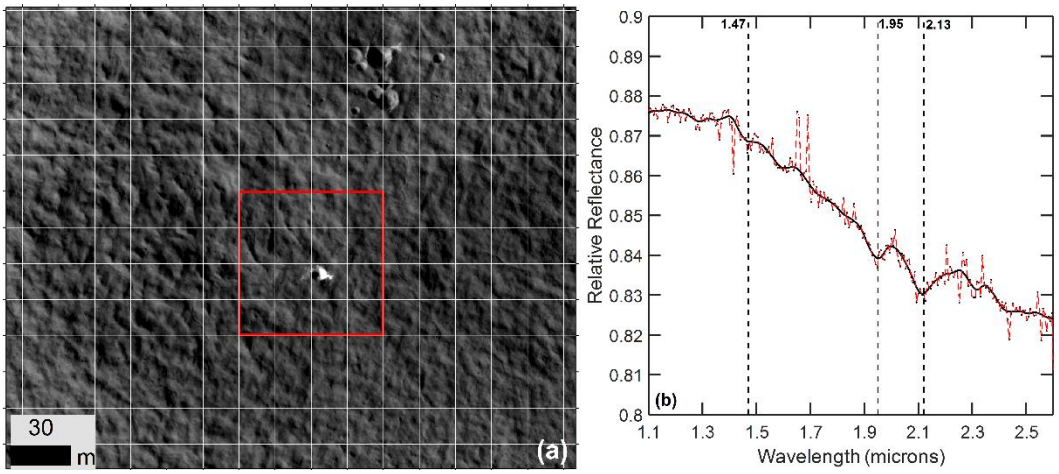

Figure 5.3. Impact-excavated ice and CRISM spectrum of the surroundings. (a) HiRISE image ESP_029256_2195_RED showing a relatively small crater, ~10 meters in diameter. Grid lines show the pixel size of the coordinated CRISM observation (18m/pixel). The red square shows the uncertainty in coregistering the CRISM pixel to the HiRISE observation. (b) CRISM FRT0002755E spectrum corresponding to two pixels within the red bounding box shown in (a).

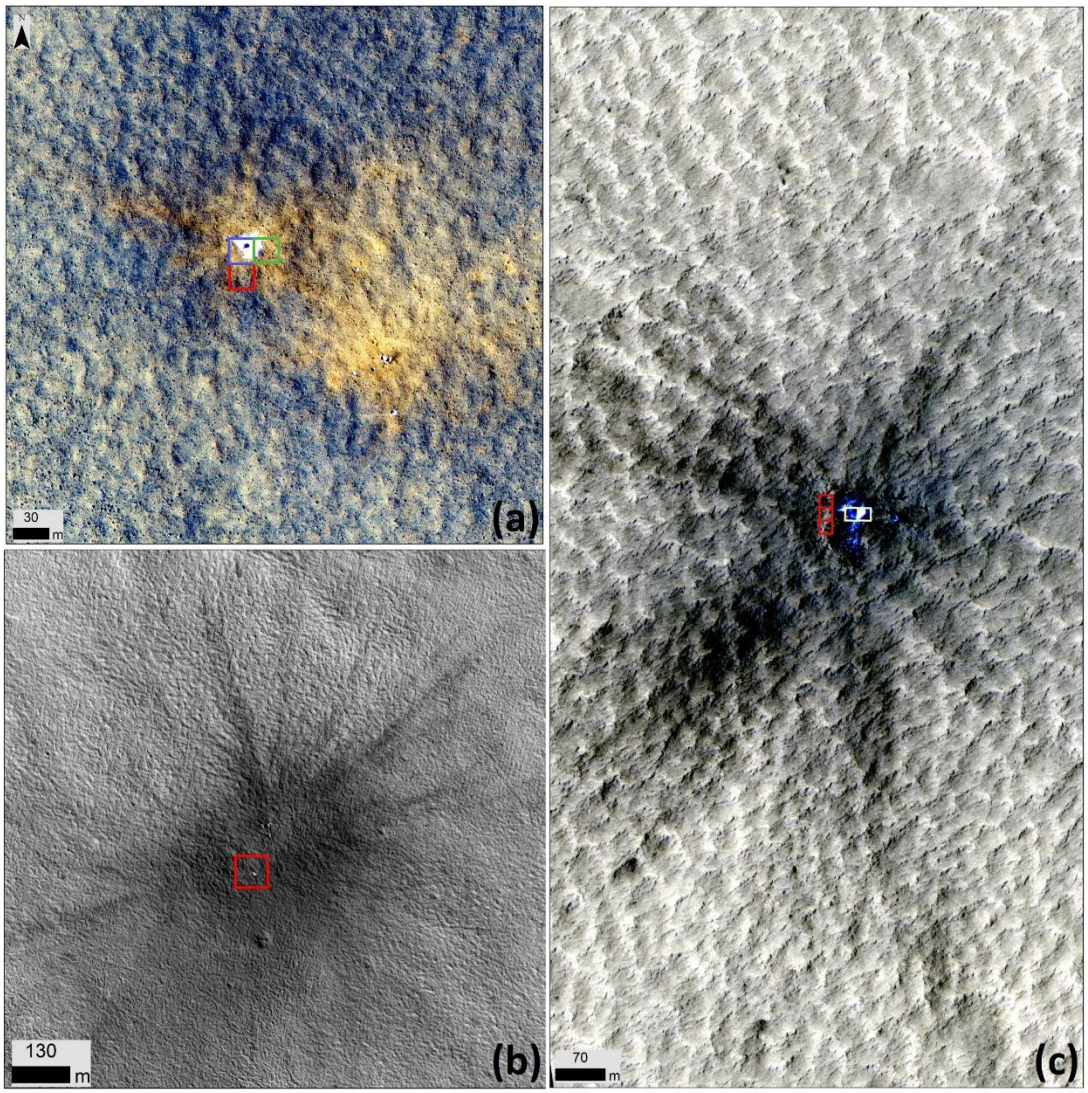

Figure 5.4. HiRISE view of the impact sites studied in this paper showing the extents of their ejecta blankets. (a) HiRISE image PSP_010625_2360 (Infrared-Red-Blue/Green (IRB)) showing the impact crater cluster and associated ejecta. The colored boxes correspond to the locations of the spectra shown in Figure 5.1. (b) HiRISE image ESP_029256_2195_RED showing blast zone from the impact event and the location of the spectrum shown in Figure 5.3. (c) HiRISE image ESP_016954_2245_IRB showing the impact and associated ejecta blanket. Colored boxes show the location of CRISM spectra in Figure 5.2.

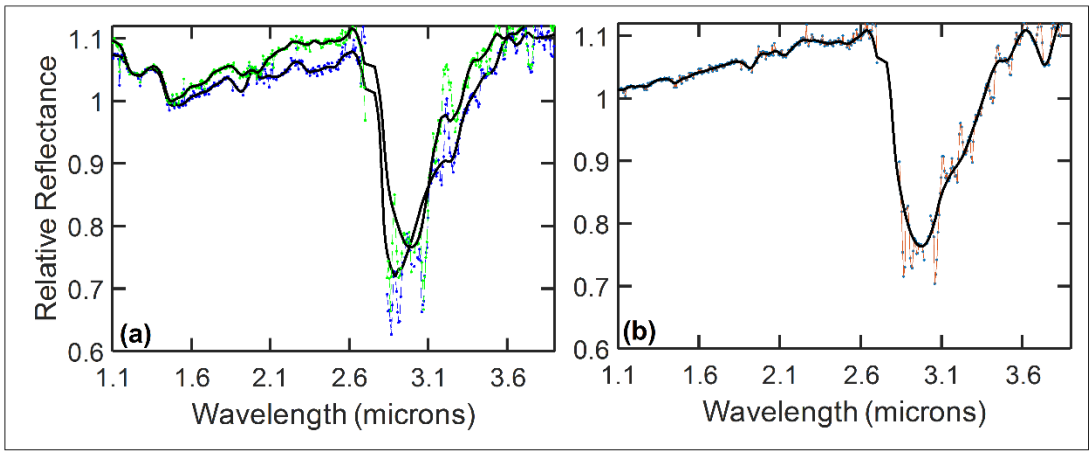

Figure 5.5. Ratio spectra of impact excavated ice and surrounding regions from CRISM FRT0000D2F7. (See Figure 5.1 and Figure 5.4 for the location of the region corresponding to the spectra). **(a)** CRISM spectra of impact excavated ice showing a deep ~3 μm absorption band. **(b)** CRISM spectrum of the area south of the impact excavated ice showing a deep ~3 μm absorption band due to a hydrated mineral, in addition to the narrower weaker overtone features at shorter wavelengths.

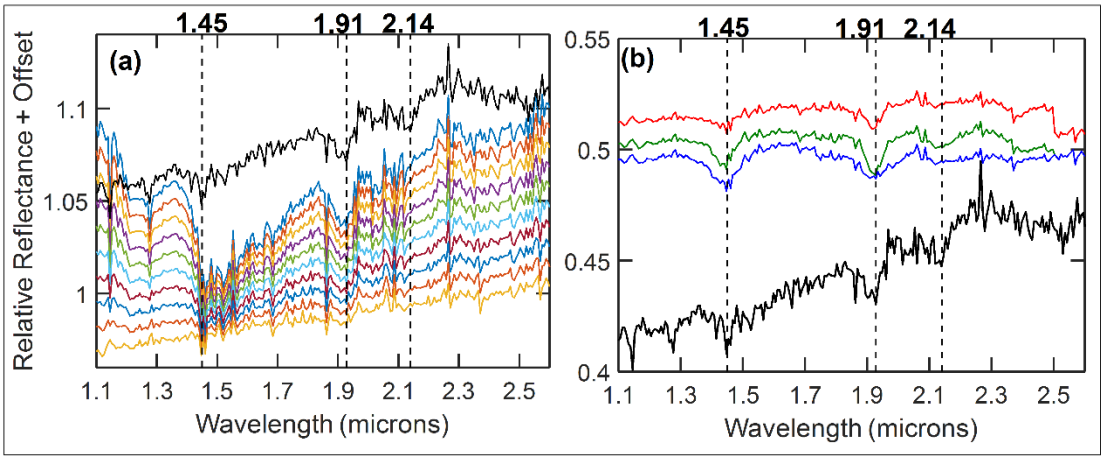

Figure 5.6. Linear spectral mixture result for Site-I. (a) The black spectrum shows the observed spectrum from Site-I with absorption band at 1.45 μm, 1.91 μm, and 2.14 μm. Colored lines are linear spectral mixtures between the impact excavated ice (blue spectrum from Figure 5.1) and Martian regolith (decreasing from 90% ice and 10% regolith on the top to 10% ice and 90% regolith at the bottom). (b) Linear spectral combination of various perchlorate salts (Red: Mg, Green: Na, and Blue: Ca) (50 %) and Martian regolith (50 %). The black spectrum is that observed from Site-I. The spectral mixture between Martian soil and sodium perchlorate is able to reproduce the 2.14 μm band. The difference in spectral slope can easily result from textural differences.

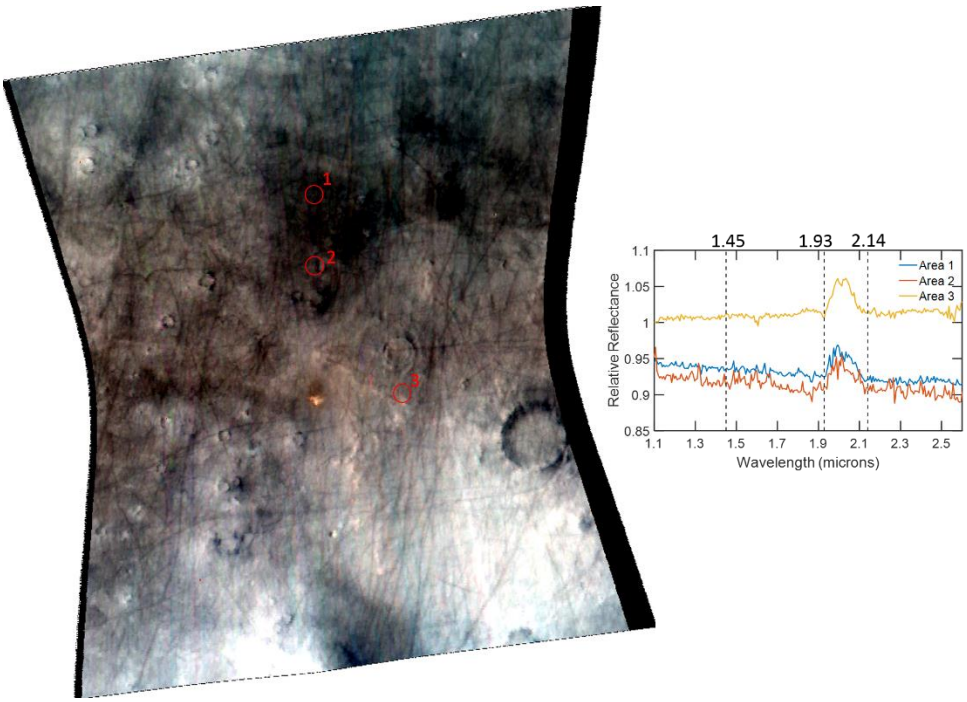

Figure 5.7. The result from multi-range spectra feature fitting (SFF) tool applied to CRISM image of Site I. SFF identified a few pixels (bounded by the red circles) that had less than 10% RMS from the input spectrum. Spectra from those regions in red are shown in the spectral plot.

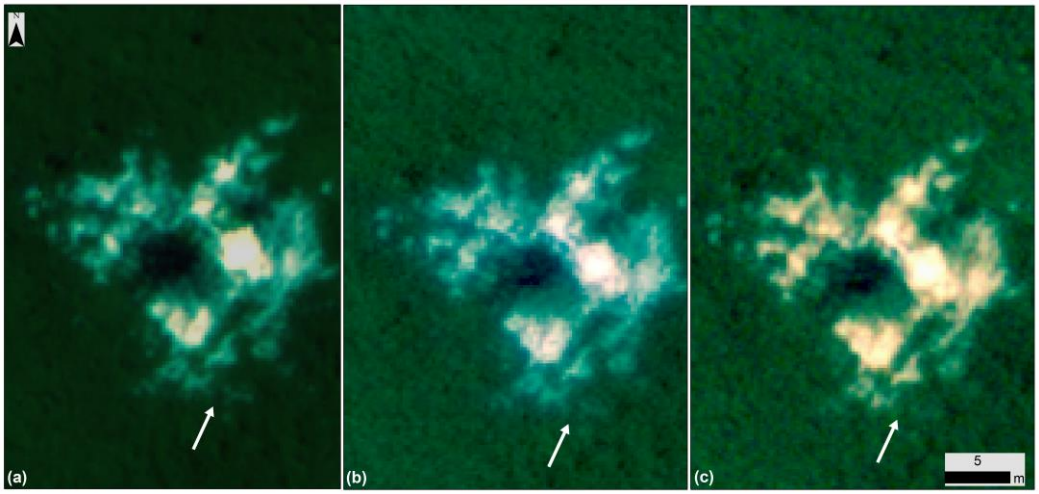

Figure 5.8. Repeat observation of Site-I with HiRISE. (a) HiRISE (IRB) observation PSP_010625_2360 (MY: 29 Ls: 151 Sol: 319) showing the 5 m impact crater and

excavated sub-surface ice. (b) ESP_011337_2360 (MY: 29 Ls: 180 Sol: 372), and (c) ESP_011548_2360 (MY: 29 Ls: 190 Sol: 389) showing the same impact crater. All images were linearly stretched using a minimum-maximum linear stretch, where the minimum value was set to 80% of the maximum value in the scene. White arrows point to the same region in the three images where minor sublimation is observed.

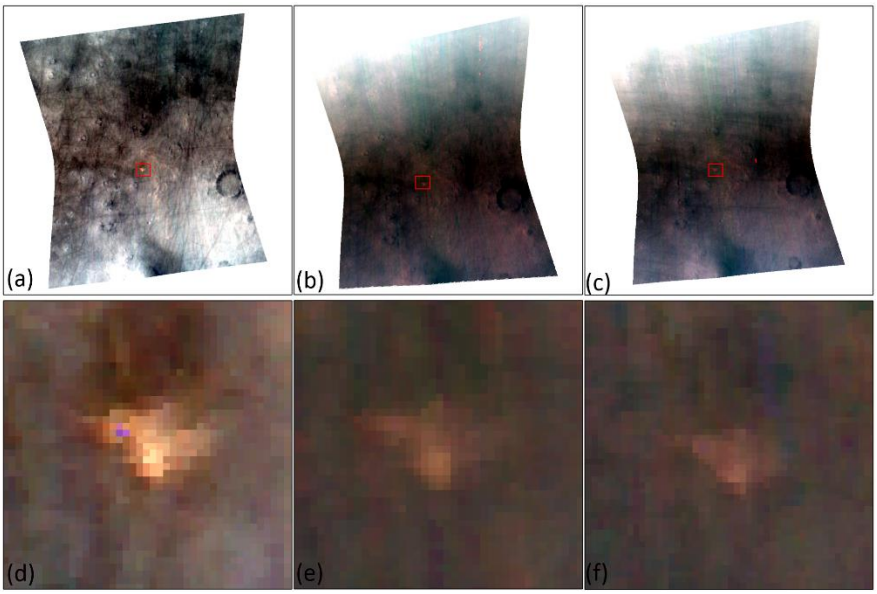

Figure 5.9. Coordinated observation of Site-I by CRISM. (a)-(c) Map-projected view of CRISM FRT0000D2F7, FRT00010274, and FRT000107CF. The red box shows the location of the impact excavated icy-ejecta. (d)-(f) A close-up view of the icy ejecta excavated by the impact at this site. All images acquired at 18m/pixel resolution.

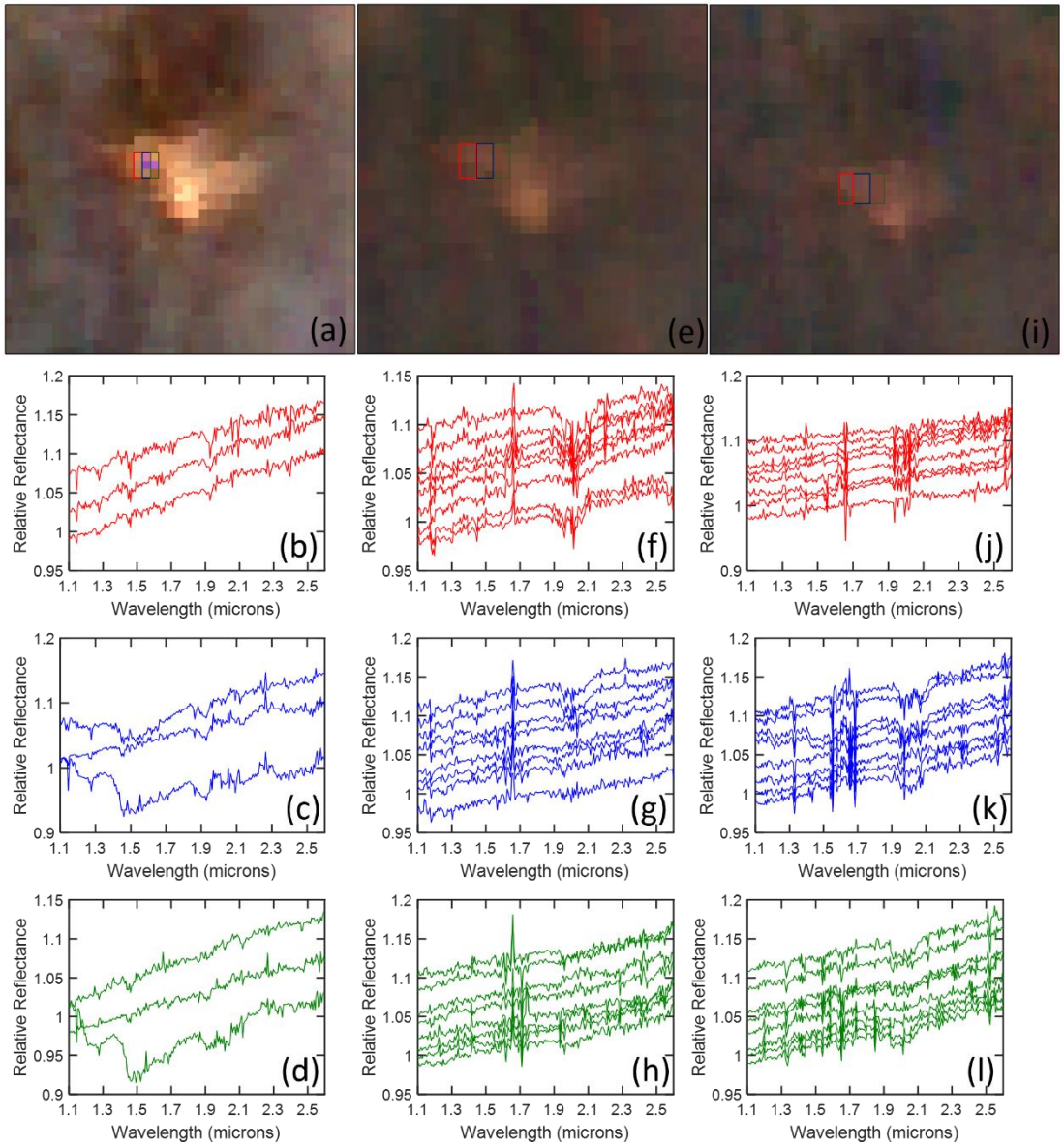

Figure 5.10. Temporal evolution of the spectra of the icy ejecta. (a) FRT0000D2F7 showing the icy ejecta site. (b)-(d) Spectra from each of the colored ROIs shown in (a). (e) View of the icy ejecta in FRT00010274. (f)-(h) Spectra corresponding to pixels within the same colored ROIs shown in (e). Broad features centered around ~2 μm are attributed to artifacts of atmospheric CO_2 removal. (i) View of the icy ejecta in FRT000107CF. (j) – (l) Spectra corresponding to pixels within the same colored ROIs shown in (i). The ice is clearly present in the later images, but likely obscured by dust.

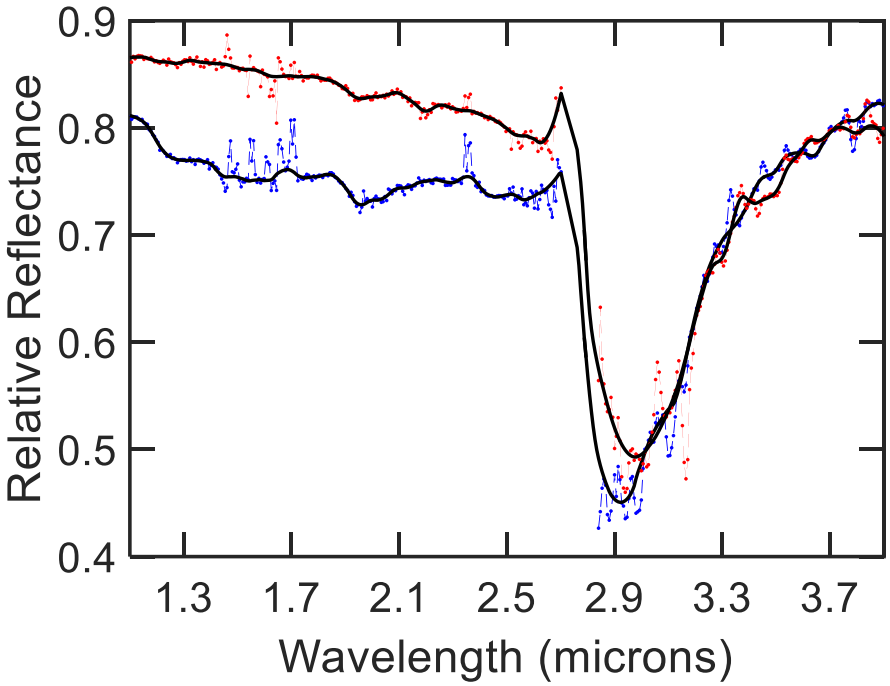

Figure 5.11. Ratio spectra of impact excavated ice (in blue) and surrounding region (in red) from CRISM FRT0001719F. Both exhibit a deep 3 μm absorption band due to ice in the blue spectrum and a hydrated mineral in the red spectrum. See Figure 5.2 and Table S5.1 for the locations corresponding to the spectra.

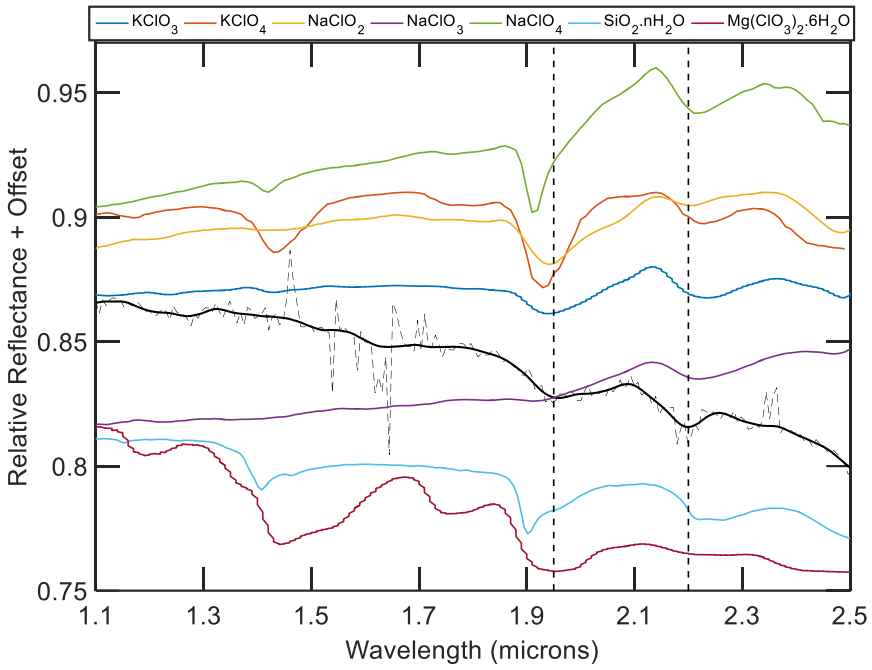

Figure 5.12. Spectra of various anhydrous chlorite, chlorate, perchlorate salts and hydrated silica with absorption bands at ~2.2 microns. The weak 1.9 μm is due to remnant adsorbed water. The observed spectrum from CRISM FRT0001719F in solid black.

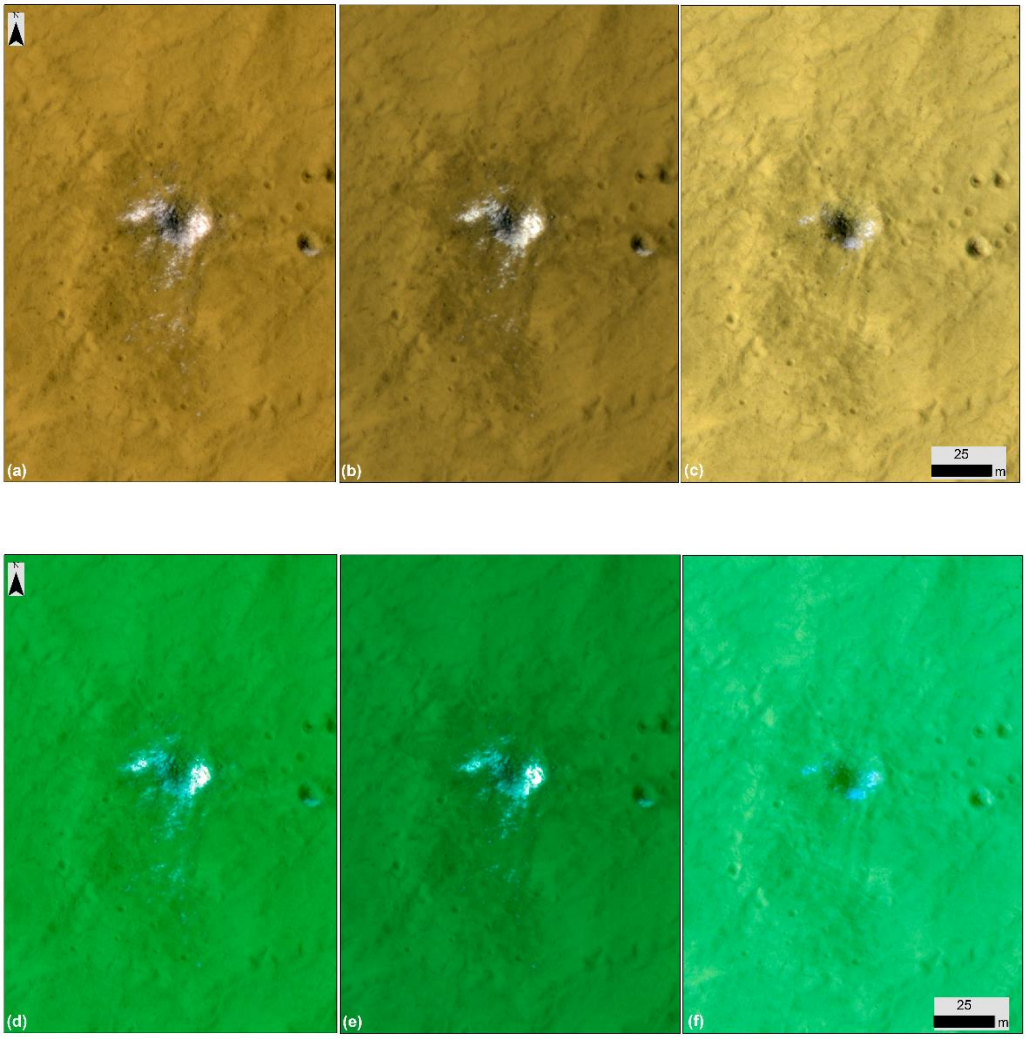

Figure 5.13. Repeat observations of site-II with HiRISE. (a) HiRISE observation ESP_016954_2245_IRB (MY: 30 Ls: 62 Sol: 130) showing the 20-m impact crater and excavated sub-surface ice. (b) ESP_017877_2245 (MY: 30 Ls: 92 Sol: 200), and (c) ESP_025314_2245 (MY: 31 Ls: 46 Sol: 96) showing the same impact crater. Manual stretch applied to keep the brightness and contrast similar between all the images. (d)-(f) same as (a) – (c), but with a linear stretch between the maximum value in the scene and 80% of that maximum value as the minimum.

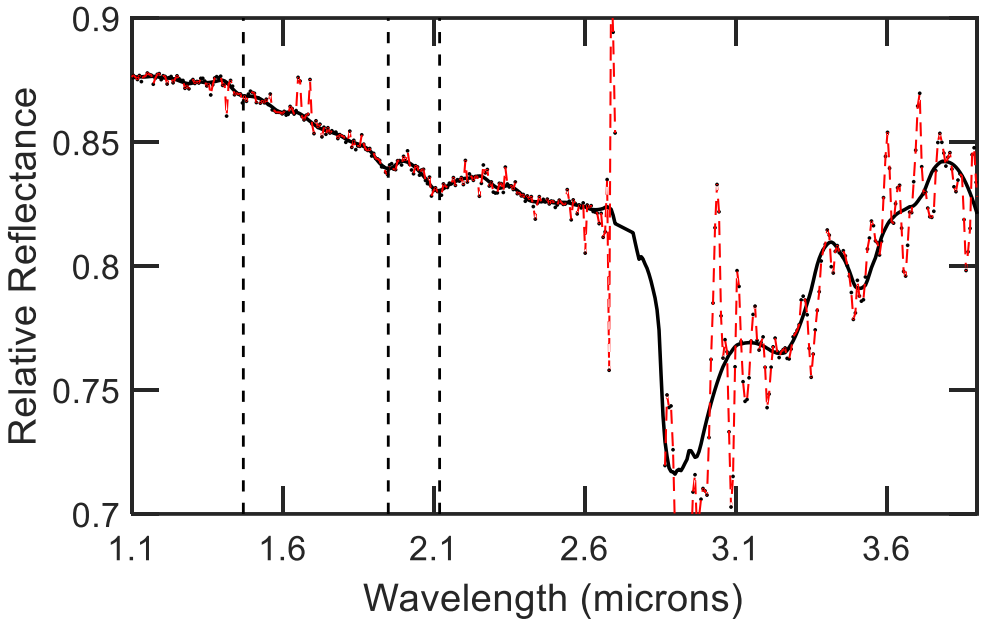

Figure 5.14. Spectrum of hydrated salts from CRISM FRT0002755E showing a deep 3 μm absorption band. See Figure 5.3 for the location corresponding to the spectrum.

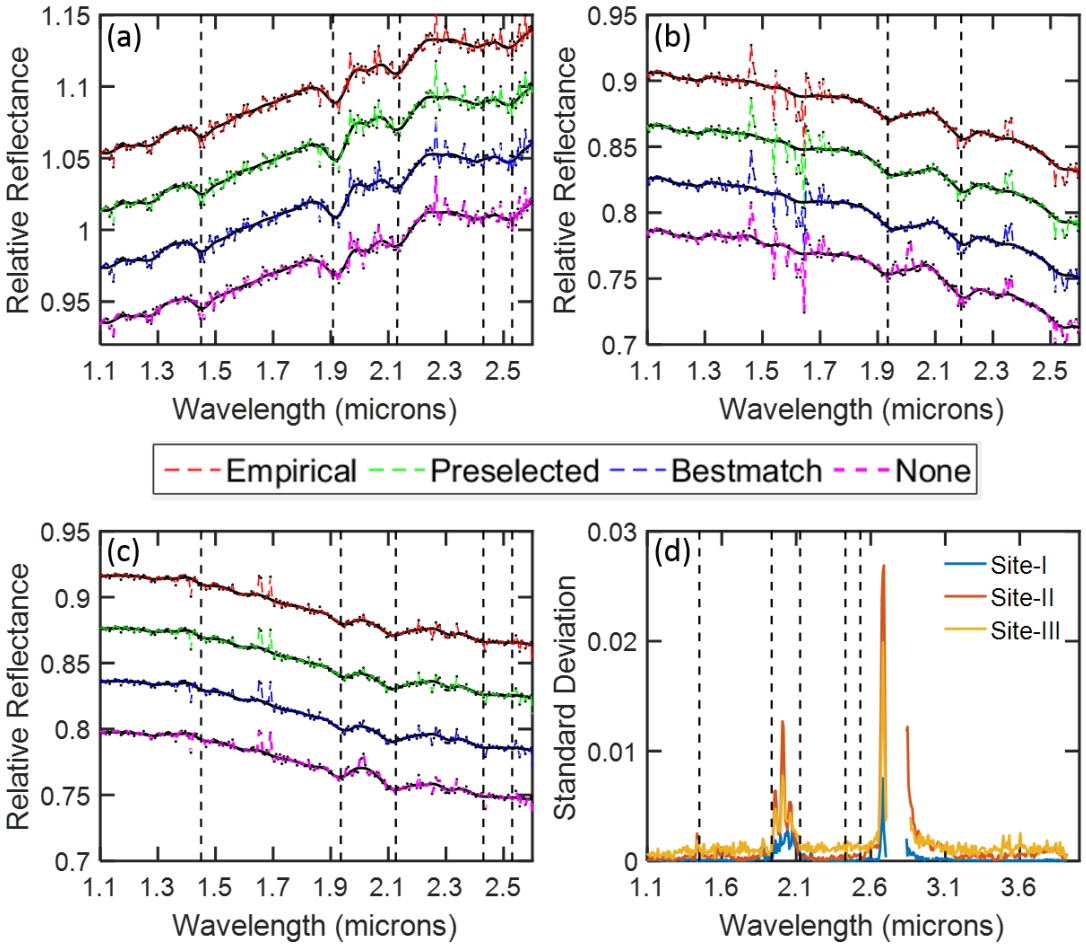

Figure 5.15. Relative reflectance spectra of the sites discussed here and the effect of various atmospheric correction. (a)-(c) Reflectance spectra of the pixel(s) where 2.13 μm and 2.19 μm absorption bands are observed in Site-I to Site-III respectively. Different volcano scan observations used are, "*Empirical*: Empirically optimized for each observation; *Pre-selected*: Pre-selected volcano scan optimum for time period; *Best match*: Best match to optical bench temperature-derived spectral shift and; *None*: No atmospheric correction". (d) Standard deviation in the reflectance values due to various atmospheric correction approaches as a function of wavelength for Site-I to Site-III. Note the low residuals near the wavelength of interest.

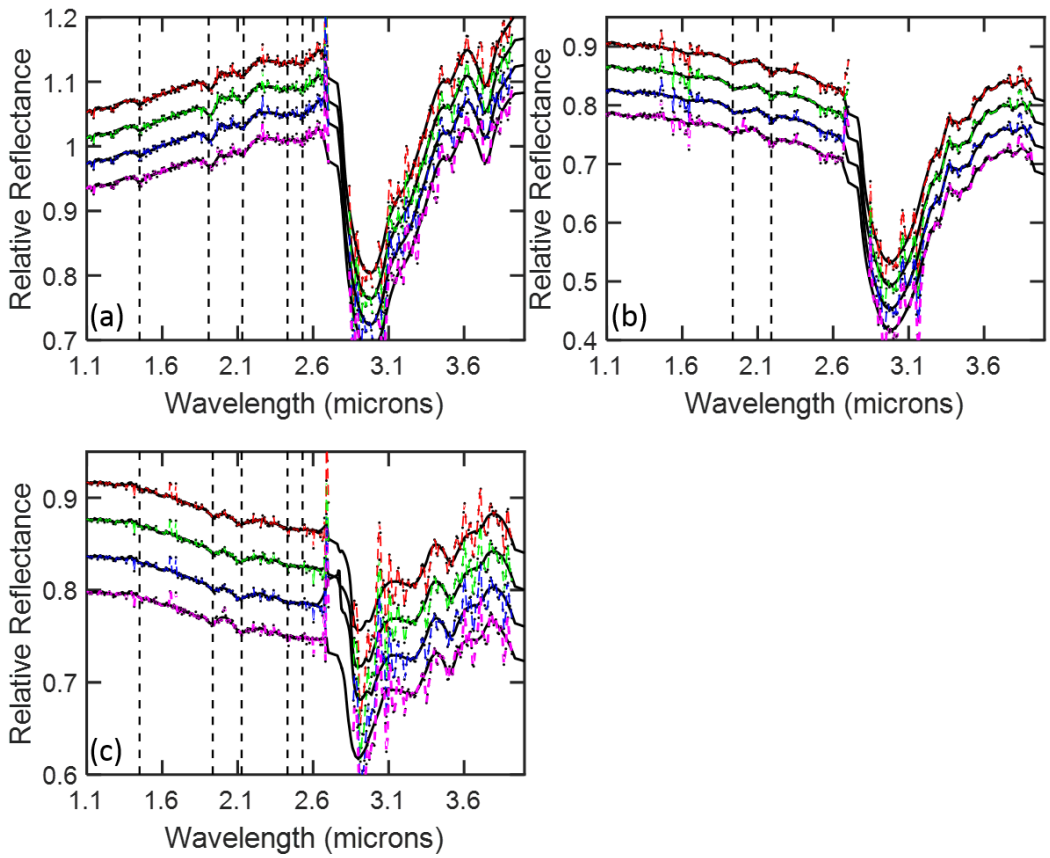

Figure 5.16. Relative Reflectance spectra of the sites discussed here ((a)-(c): Site-I to Site-III respectively) and the effect of various atmospheric corrections on the 3 μm absorption band.

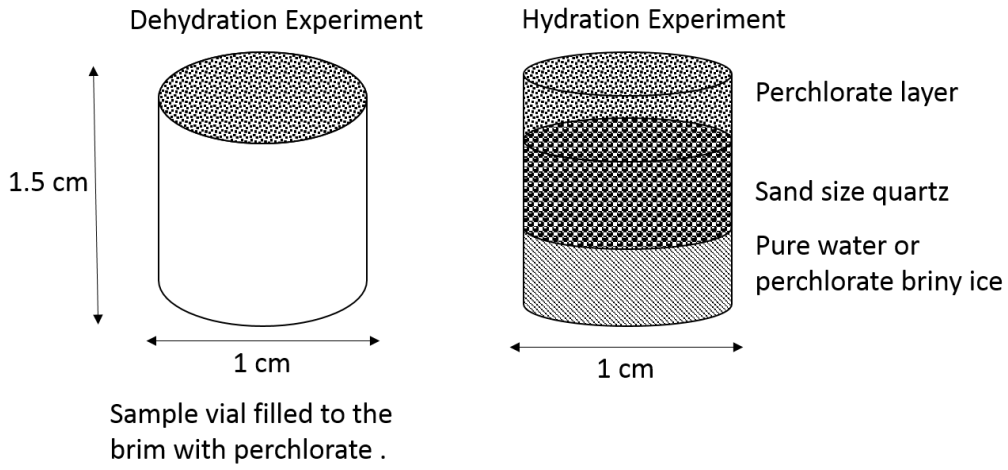

Figure 5.17. Schematic diagram showing the configuration of the sample in the dehydration and hydration experiments.

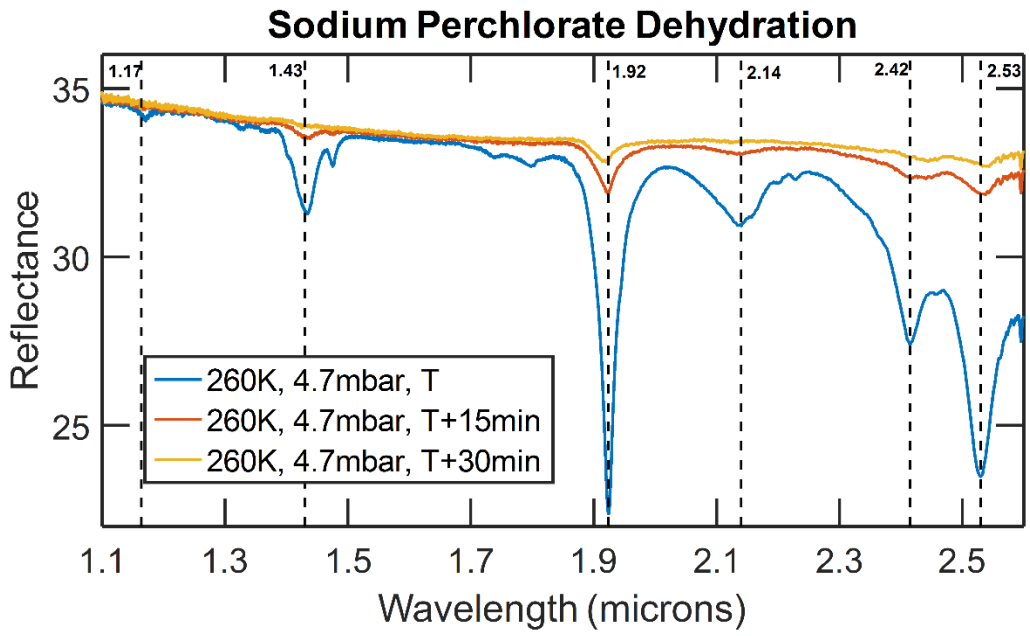

Figure 5.18. Dehydration cycle of sodium perchlorate monohydrate at Martian daytime temperature and pressure conditions (T:260 K, P <10 mbar) as a function of time (T), showing a rapid decrease in the band depth of the key absorption feature.

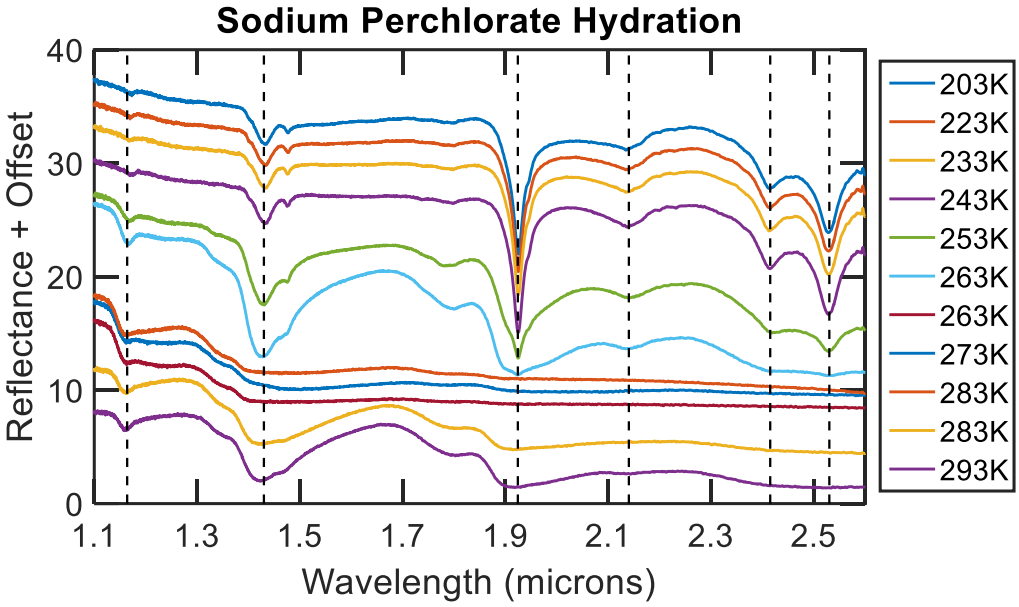

Figure 5.19. Hydration cycle of sodium perchlorate monohydrate. As temperature increased, the sublimation of sub-surface ice (see Figure 5.17 for schematics) hydrated the perchlorates on the surface. At T = 263, the flat spectra correspond to formation of an aqueous solution. As temperature increased further, water began to evaporate and at T = 293 K, a spectrum corresponding to hydrated salts was observed.

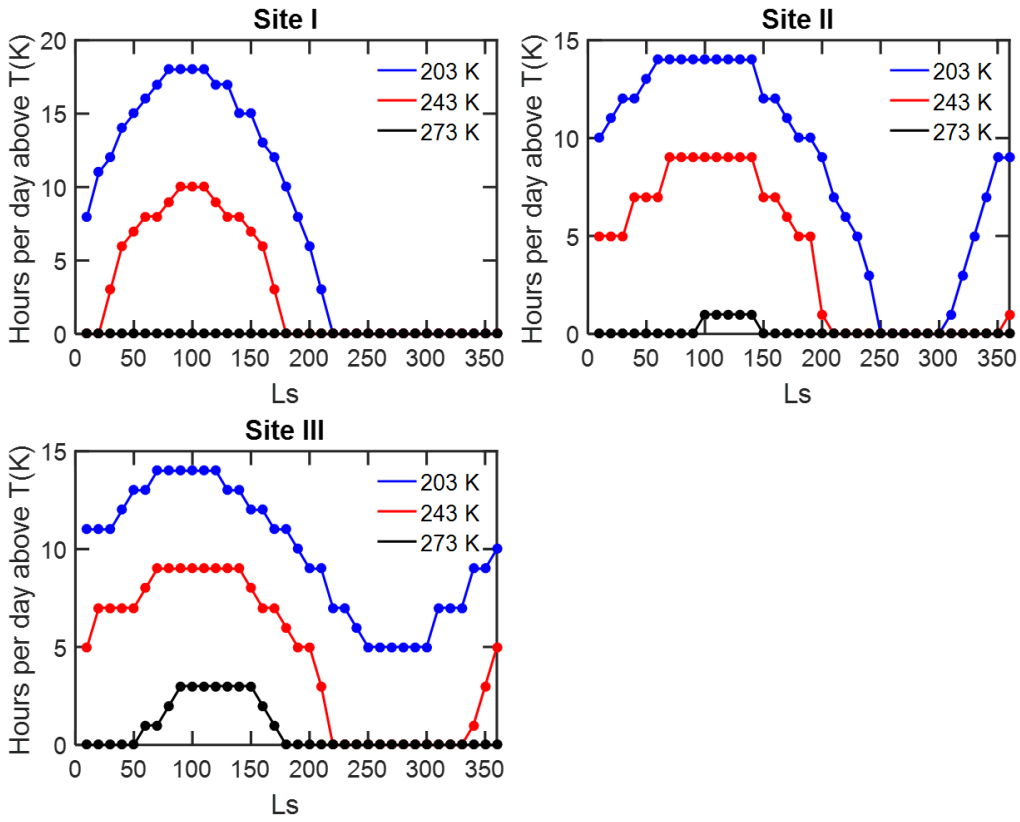

Figure 5.20. Plot showing the number of hours per day as a function of the solar longitude when the temperature is above 203 K, 243 K, and 273 K, eutectic temperatures for magnesium perchlorate, sodium perchlorate and pure water respectively, for all the sites discussed here.

Chapter 6

GEOPHYSICAL CHARACTERIZATION OF ELYSIUM PLANITIA: IMPLICATIONS FOR INSIGHT MISSION

6.1. Summary:

The Heat Flow and Physical Properties Probe (HP^3) on board Interior Exploration using Seismic Investigations, Geodesy and Heat Transport (InSight) will provide the first *in-situ* heat-flow measurement from the sub-surface of Mars. A key parameter necessary for the interpretation of the heat-flow data and radiogenic elemental abundance is crustal thickness. We used gravity and topography data from Mars Reconnaissance Orbiter and employed various modeling approaches to characterize the geophysical properties of the proposed (at the time of writing) InSight landing site area in Elysium Planitia. Our observation and modeling of the gravity data suggest that the crust in Elysium Planitia is relatively thin (17-30 km). The top-load density is found to be relatively low ~2400 kg/m^3, possibly due to the presence of pyroclastic or brecciated regolith deposits. The region's admittance spectrum is also well matched by a model with a bottom-to-top load ratio of 0.8, consistent with a pronounced bouguer anomaly observed at the landing site. Based on elemental abundance data compiled by the Gamma Ray Spectrometer (GRS) on board Mars Global Surveyor along with our crustal thickness model, we find the crustal contribution to heat-flow to be in the range of 4-6 mW/m^2. Validation and/or adjustment of our predicted geophysical parameters by *in-situ* data from InSight will allow better characterization of geophysical parameters for the rest of the planet.

6.2. Introduction

All rocky planets have an interior structure consisting of a crust, mantle, and core. However, the four rocky planets of our solar system have clearly evolved very differently. The thermal state and equilibrium are key parameters that control the course of planetary evolution, which in turn has a huge effect on habitability. NASA's *Kepler* spacecraft (*Borucki et al.,* 2010) has detected numerous planetary candidates with radii less than twice that of the Earth (i.e. $r < 2R_E$), with multiple of these planets within the habitable zone (*Burke et al.,* 2013). Additionally based on Doppler signal, six extrasolar planets (with $r < 2R_E$) have been identified with densities resembling those of rocky planets. It is, therefore, imperative to understand the evolution of terrestrial planets in our own solar system, to better understand the formation and evolution of terrestrial planets elsewhere in the universe.

Interior Exploration using Seismic Investigations, Geodesy and Heat Transport (InSight) is a mission to Mars whose primary goal is to understand the formation and evolution of terrestrial planets through investigation of the interior structure and processes. InSight's payload, aimed at understanding the interior processes of Mars, will consist of a seismometer, SEIS (Seismic Experiment for Interior Structure), a heat flow probe, HP^3 (Heat Flow and Physical Properties Package), and a rotation track instrument, RISE (Rotation and Interior Structure Experiment). HP^3 is a self-penetrating mole that is expected to dig down to 3 to 5 meters to get beneath the annual temperature variations. The probe trails a tether containing precise temperature sensors that will measure the temperature gradient in the subsurface. The HP^3 will stop at 50 cm intervals and conduct

active heating experiments to determine thermal conductivity. The amount of heat escaping from the planet's interior (i.e. heat-flow) is the product of the thermal conductivity and thermal gradient.

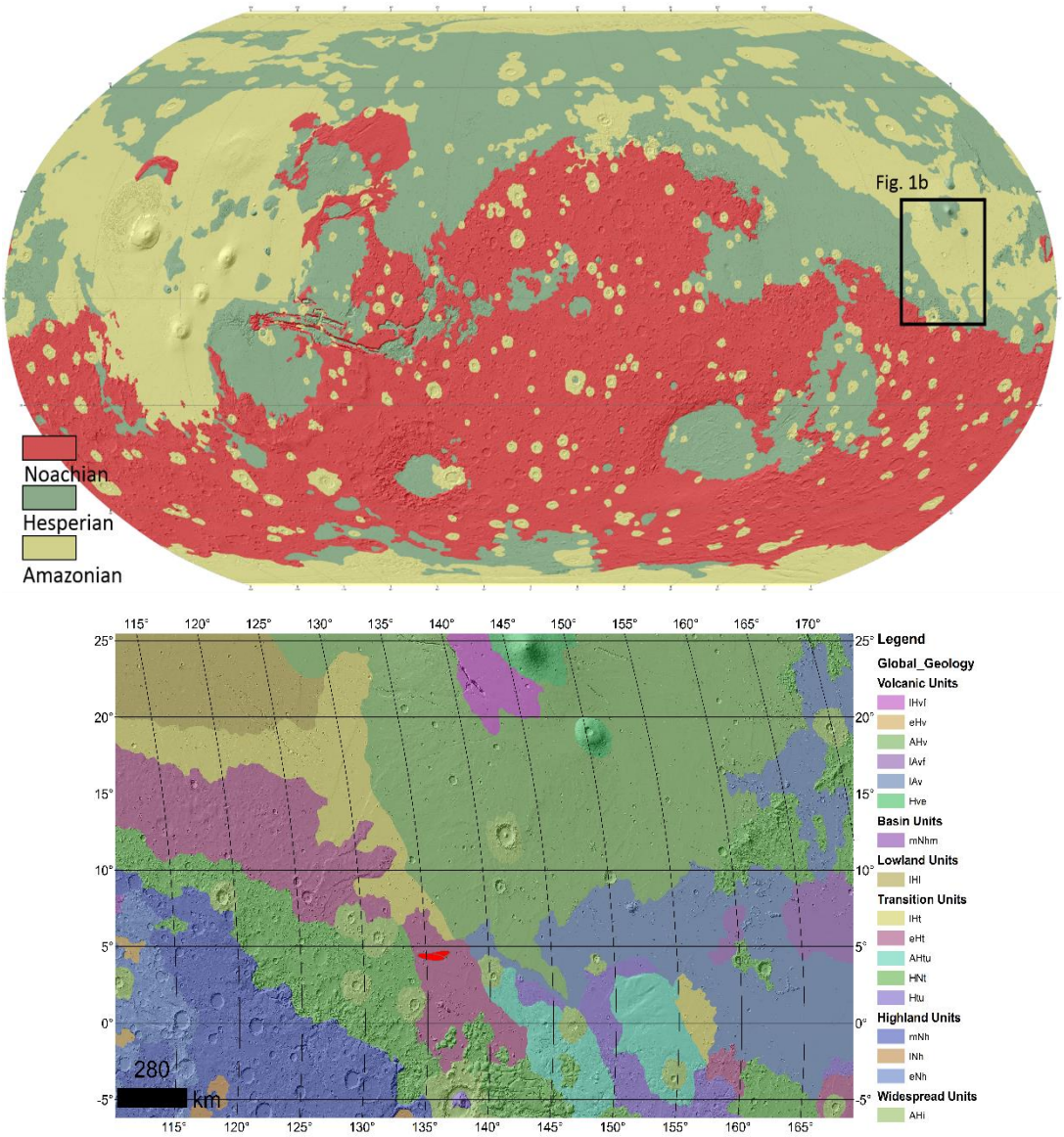

Figure 6.1: Geological context for InSight landing region. **(a)** Surface-age map of Mars showing the distribution of Noachian, Hesperian and Amazonian terrain (modified from *Tanaka et al.,* 2014). The black rectangle is centered on the InSight landing ellipse in Elysium Planitia. **(b)** Detailed geological map of the area around the InSight landing ellipse (see *Tanaka et al.*, 2014 for a full description of the legend). InSight landing ellipses (red filled ellipses near 5°N, 135°E) falls on "Early Hesperian transition unit (eHt) in magenta, and is proximal to the "Late Amazonian volcanic unit (lAv)" in blue.

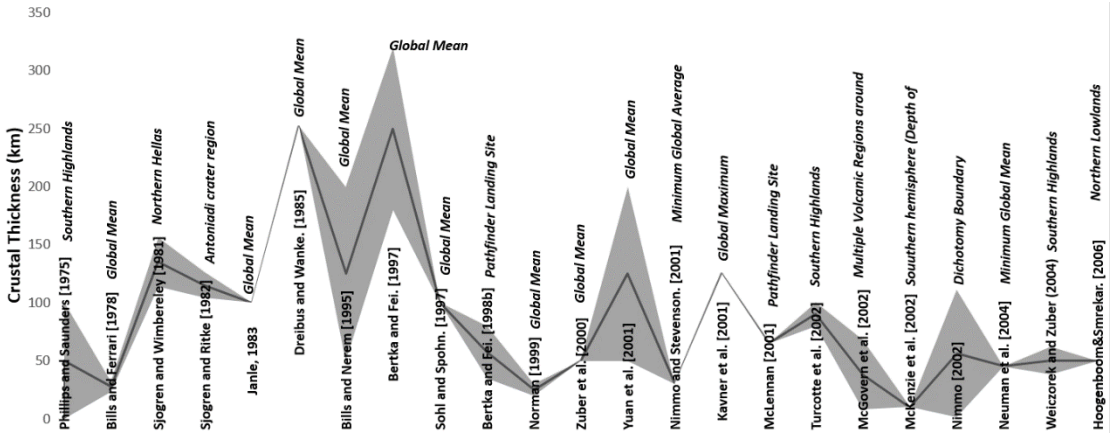

Figure 6.2: Variability in the crustal thickness values from various studies utilizing several different methodologies.

The long term interior evolution and crustal-mantle recycling of Mars are likely driven by mantle convection, partial melting and silicate differentiation in the absence of plate tectonics [*e.g. Grott et al.,* 2013 and references within]. The thermal evolution of a planetary interior depends on the internal heat sources and the mode of heat transfer. Post accretion, the major sources of internal heat are long-lived radioactive elements with half-lives of billions of years (e.g. ^{238}U, ^{235}U, ^{232}Th, and ^{40}K). These radiogenic elements are not compatible with the solid mantle undergoing melting and, therefore, get enriched in the melt. The magma ascends to the surface and subsequently forms a crust that is enriched in radiogenic materials. Due to this incompatibility in the igneous process, an estimated 50% or more of the Martian planetary budget of the heat-producing elements has been sequestered into the crust during planetary differentiation (*McLennan,* 2001; *Taylor et al.,* 2007)

Planetary heat-flow measurement provides a constraint on the radiogenic content and thermal evolution of a planet. A key aspect of interpreting heat-flow and thus the associated radiogenic content in a given area is estimating the local crustal thickness and

density. Current constraints on heat-flow come from estimated elastic and thermal lithospheric thickness based on models of lithospheric loading, which suggest both that there was a change in the heat flow during the early evolution of planet, and that the concentration of radiogenic elements may be lower than expected (*Guest & Smrekar,* 2007; *McGovern et al.,* 2002). In this work, for the proposed InSight landing site: (i) we constrain crustal properties using a variety of gravity and topography methods to aid in the interpretation of HP^3 data, exploring the uncertainty in our estimate (Section 2); (ii) we model the source of a local Bouguer anomaly using a simple geometric interface; and (iii) we calculate the expected crustal component of heat-flow based on elemental abundance maps compiled by Gamma Ray Spectrometer (*Boynton et al.,* 2004) on Mars Odyssey.

6.3. Elysium Planitia

InSight will land within the vast volcanic plains of Elysium Planitia (~4°N, 135°E) (Figure 6.1). The landing site is just north of the Martian hemispheric dichotomy which separates the heavily cratered and relatively old, thick crust of the southern highlands from the relatively smooth, thin and younger crust of northern plains (Figure 6.1). However, although the surface looks relatively smooth, a large number of craters are observed beneath the deposit that mantles the lowland, suggesting a resurfacing event in Mars' past (*Frey,* 2002). The origin of the dichotomy is not well understood, and both endogenic (e.g. *Mutch et al.,* 1976; *Wise et al.,* 1979 and many more) and exogenic (*Andrews-Hanna,* 2012; *Frey & Schultz,* 1988; *Wilhelms & Squyres,* 1984) processes have been proposed to explain the origin. Although volcanic activity in Mars was widespread during the late Noachian and Hesperian, during the Amazonian, volcanism was confined to Tharsis and Elysium

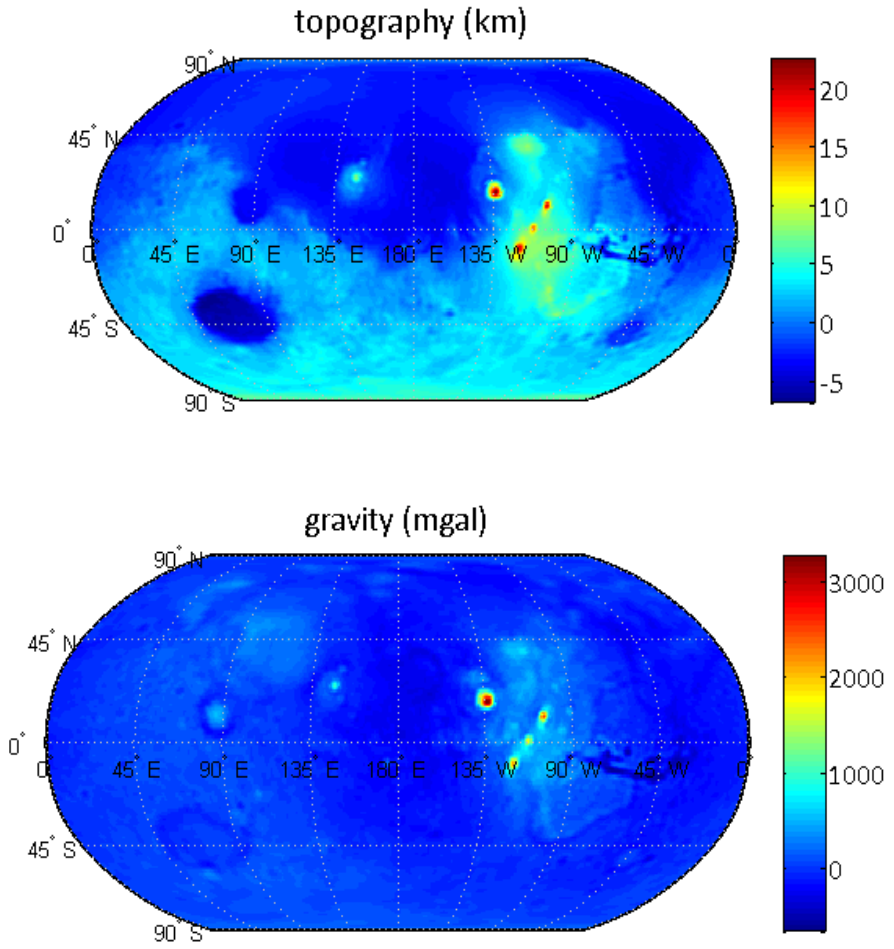

Figure 6.3. Gravity and topography of Mars. **(a)** Global topography of Mars derived from spherical harmonic expansion (degree 1 to 90). **(b)** Spherical harmonic expansion (degree 2 to 90) of the Martian gravity field.

(*Werner*, 2009). Elysium is the second largest volcanic province on Mars, spanning volcanic activity from ~3.9 Ga to as recent as 5 Ma, although the InSight ellipse resides outside this area (Figure 6.1) (*Platz & Michael*, 2011). The major peak of volcanism at Elysium is observed to be around ~2.2 Ga, and the activity has rapidly waned in the last billion year, however, this region of Mars may still be volcanically active (*Platz & Michael*, 2011). Eons of volcanic resurfacing could have made this region of Mars especially enriched in radiogenic elements, and consequentially it may have higher heat flow. However the GRS instrument, which is sensitive to decimeter depth-scale has not revealed

the near surface to be enriched in any of the long-lived radiogenic elements (*Boynton et al.,* 2007).

The Martian crustal thickness has been estimated by various authors using techniques such as (i) global gravity and topography admittance (e.g. *Bills & Nerem,* 1995; *Yuan et al.,* 2001) (ii) spatial gravity and topography admittance (e.g. *Phillips & Saunders,* 1975; *Sjorgren & Winberly,* 1981; *Zuber & Smith,* 1997) (iii) local gravity and topography admittance (*McGovern et al., 2002; Nimmo, 2002),* (iv) global crustal thickness inversion (e.g. *Bills & Ferrari,* 1978; *Zuber et al.,* 2000), (v) moment-of-inertia constraint (Sohl & Spohn, 1997)(*e.g. Sohl and Spohn* 1997; *Berka and Fei,* 1998), (vi) viscous relaxation of surface (*e.g. Nimmo and Stevenson,* 2001; *Guest and Smrekar,* 2007), and elemental surface balance models (*e.g. McLennan* 2001) (Figure 6.2). However, there is a significant variation in the crustal thickness values from all these studies, even when the focus of the study is the same geographical region (Figure 6.2).

Additionally, there have been few studies that estimated crustal (T_c) and elastic thicknesses (T_e) and heat-flow around Elysium using gravity and topography admittance methods. *Nimmo* (2002) estimated the mean crustal thickness and density near the Martian hemispheric dichotomy (110E to 220E, 40S to 20N), which includes Elysium Planitia, to be 27 km with 2500 kg/m^3 crustal density. However, areas outside Elysium Planitia in particular the topographic highs at the dichotomy and Elysium Rise, are likely to contribute significantly to the admittance spectra in this study. *McGovern et al.* 2002 analyzed the admittance spectra from the Elysium rise with reference crustal thickness of 50 km to put constraints on the elastic thickness and heat flow. They found best fitting T_e values at Elysium ranging from 50 to 80 km with a heat-flow estimate of 21-30 mW/m^2. *McKenzie*

et al. (2002) averaged admittance signal from a large region (10S to 60N, 115 to 175E) and found the best T_e value to be about 29 km. In all of the previous analyses, the gravity signature was either dominated by the Elysium rise or included a very extensive region. This works constrains the crustal thickness, crustal density and loading ratio localized to section of Elysium Planitia hosting the proposed InSight landing site and excludes the Elysium rise and other surrounding terrains to the extent possible.

6.4. Methodology:

Building on previous tracking data from Mars Global Surveyor and Mars Odyssey, the tracking data from Mars Reconnaissance Orbiter has been incorporated to resolve the static gravity field of Mars to degree and order 110 (*Gravity model: jgmro_110b*; (*Konopliv et al.,* 2011)). The Mars Orbiter Laser Altimeter (MOLA) with an accuracy of 1 m, has resolved the Martian topography to degree and order 23040 (*Rexer & Hirt,* 2015), but we used the expansion of the topography to 2600 (*Topography model: MarsTopo2600.shape*; (M. Wieczorek, 2011); *http://www.ipgp.fr/~wieczor/SH/SH.html*). Although the gravity field is resolved to degree and order 110 for Mars, at spherical harmonic degrees greater than the 90, the data suffers from low signal-to-noise ratio (*Konopliv et al.,* 2011). Thus we truncate the gravity, geoid, and topography data at degree and order 90 (Figure 6.3).

6.4.1 Global Crustal Thickness Inversion:

Numerous work in the past has solved for the crustal thickness of Mars assuming uniform density for the crust and mantle (e.g. *Zuber et al.* 2000 and many others). In all cases, the density of crust (ρ_c = 2900 kg/m^3) and mantle (ρ_m = 3500 kg/m^3) were based on petrologic observation of the SNC meteorites (e.g. *Goettel,* 1981; *McSween,* 1985 and

many others). Assuming mantle density of 3500 kg/m^3, and crustal density in the range of 2700-2900 kg/m^3, we calculated the Bouguer gravity anomaly from the surface topography. We used the method of *Wieczorek & Phillips,* (1998) *t*o solve for the relief on the crust-mantle interface (i.e. Moho), required to explain the Bouguer gravity anomaly. The method involves computing potential anomalies due to finite amplitude relief on a sphere, and downward continuing the Bouger anomaly. The crustal thickness is then calculated by subtracting the relief on the Moho from surface topography. No assumption of isostasy is involved. We use our Bouguer solution to constrain the uncertainty in crustal thickness in Elysium Planitia from various methodologies (Figure 6.2).

6.4.2. Admittance

Admittance (Z), a transfer function between the topography and gravity examines their relation in the spectral domain and is sensitive to elastic and crustal thickness. Admittance of the landing site was generated by filtering spherical harmonic fields with axisymmetric windows of constant diameter (L_{win} = 5, 10 and 15 corresponding to the spatial diameter of 4000, 2000, and 1400 km) using SHTools (*M. Wieczorek, Meschede, & Oshchepkov,* 2015) . We conduct a series of forward-modeling exercises to attain synthetic-gravity fields of Mars based on topographic loading and a number of structural and density parameters. The model relies on a simple, thin elastic shell implementation for lithospheric flexure, analogous to that of *McGovern et al.,* (2002); the shell deforms elastically in response to surface and buried loads, with elastic displacements being dependent on the magnitude of the loads and the elastic thickness (T_e). We assume conventional values for Young's Modulus (E = 1 x 10^{11} Pa), Poisson's ratio (0.25), and mean surface gravity (g_{mars} = 3.71 m/s^2) for Mars. In addition to defining the lithosphere, the model comprises five

density interfaces: (i) topographic load surface, (ii) crustal surface, (iii) crust-mantle boundary, (iv)bottom-load upper relief, and (v) bottom-load reference surface. As such, there are four densities defined in the model: topographic (ρ_t), crustal (ρ_c), mantle (ρ_m) and bottom-load (ρ_b). The magnitude of the surface load derives from the amplitude of the equipotential topography, or height of surface above the areoid (e.g., *McGovern et al.,* 2002), and density ρ_t of the material. For the buried or bottom load, we assume it to be correlated with the surface topography and proportional to it via the bottom-to-top load ratio fbt, where the thickness of the bottom-load depends also on the density contrast ($\rho_b - \rho_m$) between this bottom-load and the surrounding mantle. The resulting elastic displacements are applied to all of the five interfaces, which, along with the assigned density values, are used as the input for the calculation of the synthetic gravity potential field.

Forward modeling of the potential anomalies relies on the finite amplitude algorithm of *Parker,* 1973; *Wieczorek & Phillips,* 1998 *a*nd takes place with aid of the SHTOOLS library of spherical harmonics routines (*Wieczorek et al.,* 2015). The finite amplitude algorithm produces potential anomalies on a sphere by raising the topographic field to an arbitrary power (n^{th}) and expanding it into spherical harmonics. The precision of the model solution is determined by the value of n, with the contribution to the solution becoming smaller with increasing n. As with *Wieczorek et al.,* 2015, we find that truncating the solution at n=7 yields a precision on the order of few mGals. Another strength of this method is that it is robust in cases where the topographic amplitude is large with respect to the lateral scale of the features being studied, which is a condition amply abundant on Mars, but much less so in our study area. Contribution from each of the five interfaces, after

upward-continuation from their respective depths to the surface, add in the spectral domain to give the resulting synthetic potential field coefficients. Admittance based on the synthetic potential fields and observed topography are then generated and compared with the observed admittance. We calculate root-mean-square of the difference between the modeled and observed admittance to find the best fit.

6.4.3. Isostatic Anomalies and Apparent Depth of Compensation:

We calculated the isostatic anomaly assuming various thicknesses (or apparent depth of compensation (ADC)) for a crust of density ρ_c overlying a mantle with density ρ_m to remove the effect of an isostatic layer from Bouguer gravity. The apparent depth of compensation (ADC) is the depth at which the isostatic anomaly, assuming complete Airy compensation is minimized (i.e. hydrostatic equilibrium). We calculated isostatic anomalies as a function of various ADC to explore the variability in the subsurface structure. Specifically, we calculated the isostatic anomaly as a difference between the Bouguer gravity and the gravity predicted for a given ADC in the spectral domain

$$\Delta g_{iso} = g_{boug}(1 - e^{-k*ADC}) .$$

Here, $\Delta g_{iso}$is the isostatic anomaly, Δg_{boug} is the Bouguer gravity anomaly, k is the wavenumber, and ADC is the apparent depth of compensation. The exponential term corresponds to the downward continuation of the Bouguer gravity anomaly to the level of the ADC.

6.4.4. Bouguer Reduction and Modeling:

The Bouguer gravity anomaly at the InSight landing site was calculated from the free-air gravity data by removing the gravitational attraction due to the topography. Given the widespread volcanism in this region, one interpretation is that the anomaly is the result of intrusive volcanism. The source of the Bouguer anomaly can be modeled as a simple intrusion body (e.g. sphere or cylinder) to complex geometries, but based on profile of the Bouguer anomaly, we modeled it a result of displacement by an intrusion of a denser material (Figure 6.4). The gravity anomaly (Δg_z) resulting from this scenario can be approximated by:

$$\Delta g_z = 2G\Delta\rho h\left[\frac{\pi}{2} + tan^{-1}\left(\frac{x}{z_0}\right)\right]$$

where G is the universal gravitational constant, Δρ is the density difference between the top layer and underlying basement materials, h is the vertical step displacement, x is the distance along the surface and z_0 is the vertical distance to the mid-point of the fault (*Lowrie*, 2007).

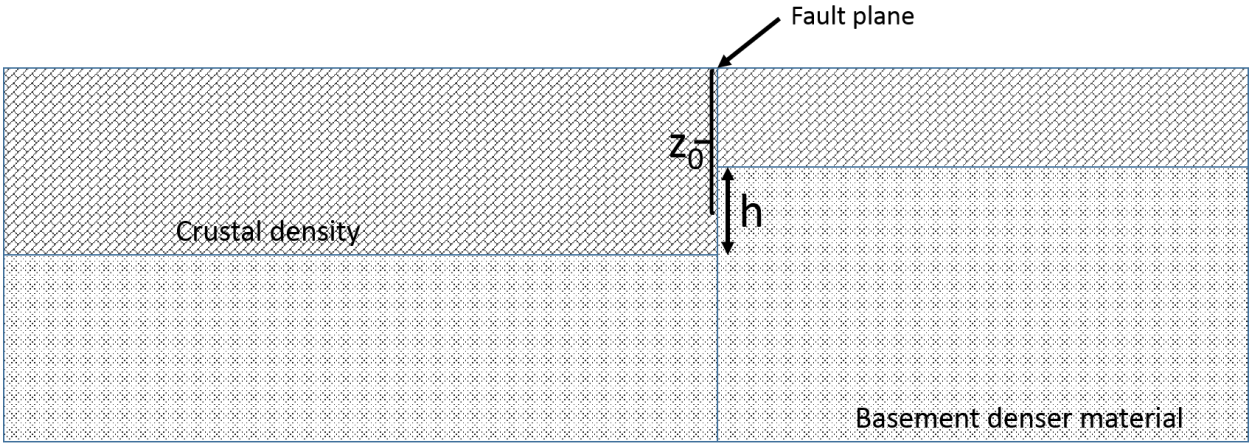

Figure 6.4: Schematic for the equation 1. Here, z_0 is the distance to the mid-point of the fault and h is the vertical displacement due to the intrusion.

6.4.5. Geometry of Horizontal Density Interface and Heat-Flow Prediction

We used the Parker-Oldenburg algorithm for computing the geometry of a density interface (i.e. moho). The inversion approach was originally formulated to calculate the gravity anomaly due to an uneven, uniform layer of material by means of a series of Fourier transforms (*Parker*, 1973). Parker's equation can be rearranged to compute the depth to the undulating interface from the gravity anomaly by means of an iterative process. This scheme allows one to determine the topography of the interface density by means of an iterative inversion procedure, assuming a mean depth of the interface, z_0, and the density associated with the two surfaces. (*Gómez-Ortiz & Agarwal*, 2005).

The shape of the density interface can be combined with elemental data to model heat-flow at the Elysium Planitia. The distribution of radiogenic isotopes of K, Th, and U can be calculated from elemental maps provided by the GRS instrument (*Boynton et al.*, 2007). GRS maps show lateral heterogeneity in the distribution of K and Th at a 5 x 5 per pixel resolution. We calculated the radiogenic 232Th, 235U, 238U, and 40K, assuming that 232Th is 100% of total Th abundance, 235U and 238U are 0.7204% and 99.2742% of total U abundance respectively, and 40K is 0.012% of total K abundance following previous work by (*Hahn et al.*, 2011) Uranium abundances were calculated using an assumed cosmological constant Th/U ratio of 3.8 (*Hahn et al.*, 2011). GRS measurement is sensitive to the top tens of centimeters of the Martian surface and is, therefore, representative of near-surface regolith, ice and dust deposits. For the GRS measurement to represent the bulk chemistry of the Martian upper crust, it must be normalized to a volatile-free basis (*Taylor & McLennan*, 2009), and which equates to a 7-14% increase in the K, Th and U abundances (Hahn et al., 2011). The heat release constants of all the radiogenic

isotopes discussed here are based on *Hahn et al.,* 2011. We used these values along with our estimate of crustal thickness heterogeneity in the landing site to produce heat flow maps.

6.5. Results

6.5.1. Global Crustal Thickness Inversion

The crustal thickness at Elysium landing site was estimated using global crustal thickness inversion technique (see Section 2.1) as a function of crustal density. Figure 6.5 shows the crustal thickness as a function of longitude (InSight landing region ~135°E), for 1-degree latitudinal bands between 2°N and 7°N. Crustal thickness increased with increasing crustal density, but regardless of the crustal density value used, the thickness was found to be in the range of 17 to 27 km, similar to low values inferred in other studies (e.g. *Neumann et al.,* 2004; *Zuber et al.,* 2000).

6.5.2. Gravity and Topography Admittance

The admittance of the landing site has a relatively low amplitude (<100 mgals/km), and the coherence between gravity and topography is adequate (>0.5) (e.g. *Hoogenboom & Smrekar*, 2006) for admittance analysis (Figure 6.6). Synthetic forward models computed from the assumption of elastic parameters were compared against the observed admittance (Section 2.3). The variables used to model the synthetic gravity admittance are listed in Table 6.1. We solved for T_{cr} and T_e by assuming few end-member scenarios; (a) high top-load density and (b) low top-load density (Figure 6.7).

We observe that synthetic spectra generated assuming low top-load density values better matched the observed admittance spectra (Figure 6.7). We also observe that higher

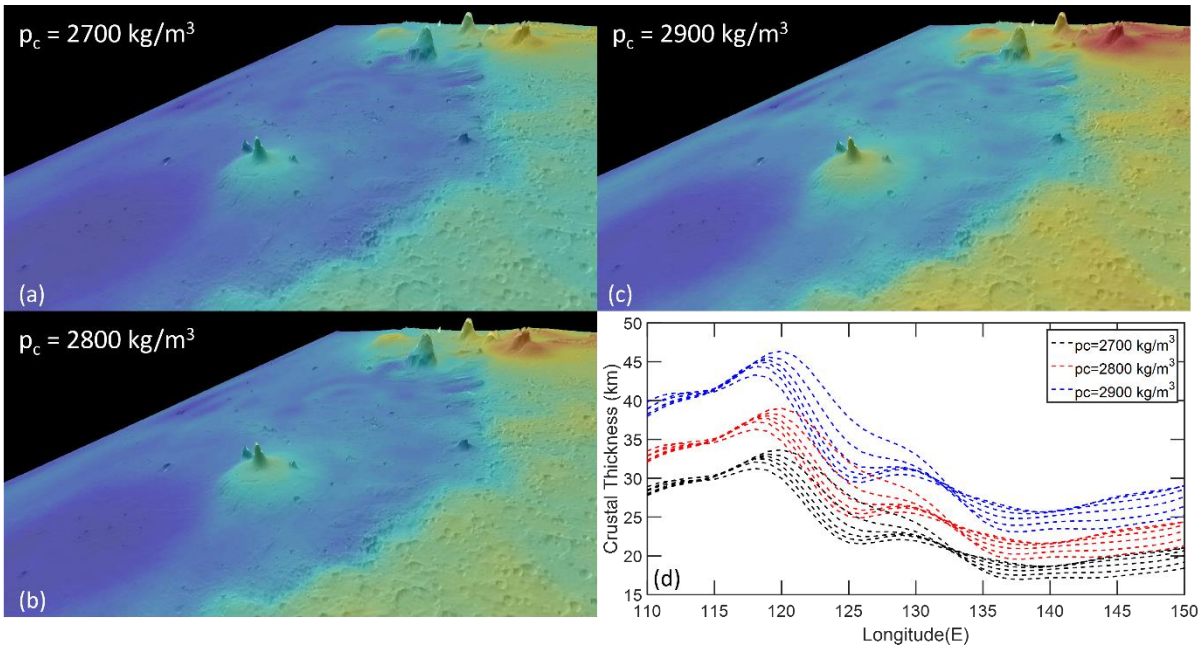

Figure 6.5: Results for global crustal thickness inversion. **(a)-(c)** Crustal thickness at the InSight landing region as a function of the crustal density. **(d)** Crustal thickness as a function of longitude (2N-7N in various lines) assuming different values for crustal density.

fbt, or a greater bottom-load contribution, provided a much better fit with the observed data (Figure 6.7). Assuming the top-load density to be 2900 kg/m^3 and fbt of 0.8, the lowest RMS corresponds to crustal and elastic thickness to be between 10-20 km and 10-80 km (Figure 6.7). However, the lowest RMS between the observed and synthetic admittance spectra was found using fbt of 0.8 and low top-load density (~2400 kg/m^3) and assuming other elastic parameters constant (see Table 6.1). In this scenario, the best matching crustal and elastic thickness are 10-20 km and 10-55 km, respectively (Figure 6.7).

6.5.3. Isostatic Anomalies and Apparent Depth of Compensation

We calculated the average isostatic gravity anomaly for the latitudinal bands of 2°N-7°N, as a function of longitude and assuming two values (one high and one low) for crustal density (Figure 6.8). We reiterated this process for various depths of compensation

(i.e. ADC). Lower isostatic anomaly is observed for ADC with lower values (Figure 6.8). At the approximate InSight landing region (~135°E), the lowest isostatic gravity anomaly is observed for 10 km, with ADC up to 30 km yielding mean isostatic anomaly under 50 mgals (Figure 6.10). Furthermore, even lower isostatic gravity anomaly is observed when the calculation is repeated using a crustal density value of 2400 kg/m^3 (Figure 6.8).

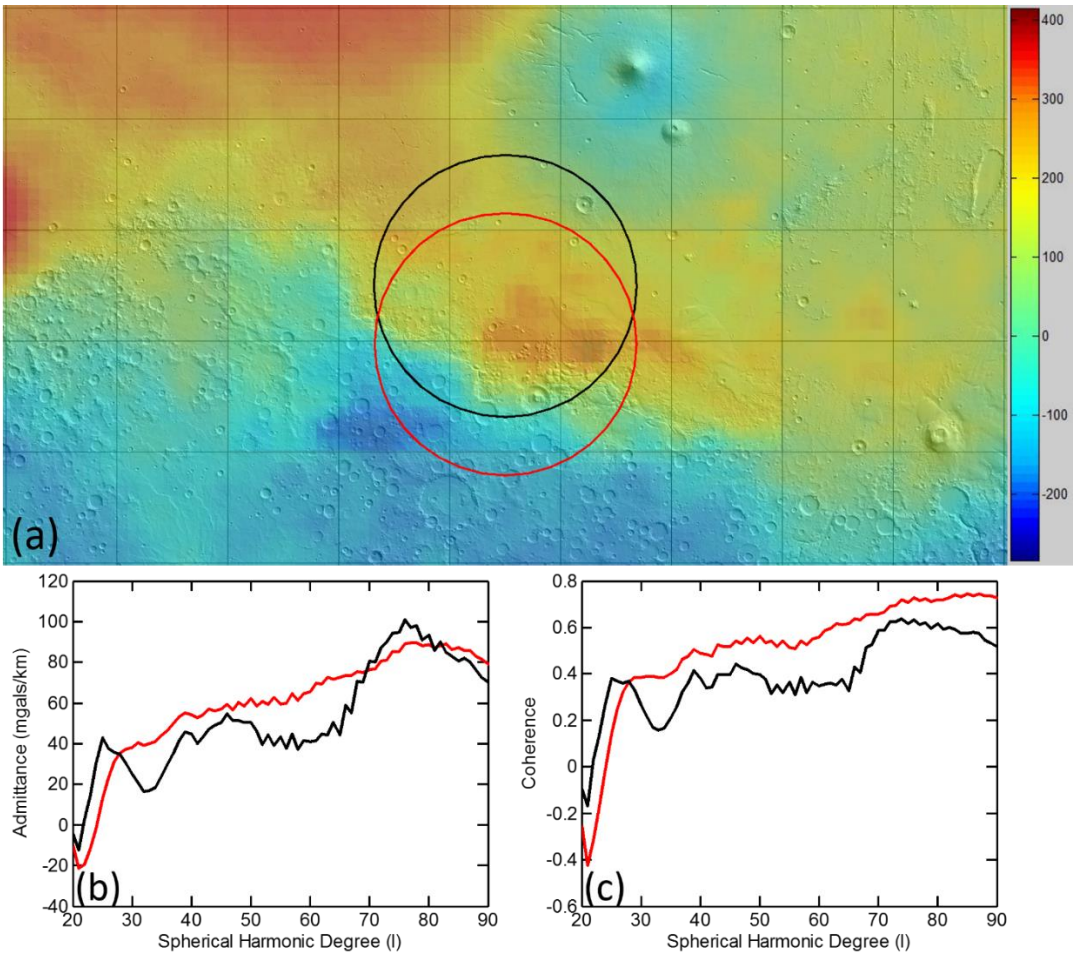

Figure 6.6: (a) Bouguer anomaly map of Mars around InSight landing site. The two circles show two locations chosen for the spherical cap (l_{win} = 15) used to truncate the admittance spectra. **(b)** Observed dmittance as a function of spherical harmonic degree (*l*) for the two circles shown in (a). **(c)** Same as (b) showing observed coherence between gravity and topography.

6.5.4. Bouguer anomaly

A high Bouguer anomaly (~350 mgals) is observed around the InSight landing region (Figure 6.6 & Figure 6.9). The longitudinal profile shows an increase in the amplitude of Bouguer anomaly from west to east (Figure 6.9). We modeled the anomaly as a result of an intrusion (Figure 6.4). We considered cases with density difference between mantle and crust from 500 kg/m^3 to 300 kg/m^3 at a depth of 30 km and 50 km (maximum crustal thickness value from global inversion and the mean crustal thickness of Mars). Regardless of case, we find that a crustal thickness difference greater than 10-15 km is necessary to match the observed Bouguer profile (Figure 6.9). Geoid-to-topography ratio (GTR), which can be used as a proxy for the depth of compensation, also shows similar profile, where GTR is relative high in the western portion (110°-135°E) than in the eastern portion (135°-160°E) (Figure 6.10).

6.5.5. Geometry of the Horizontal Density Interface and Heat Flow

We generated various models of the crust-mantle interface using Parker-Oldenburg algorithm for the heat-flow prediction model (Figure 6.11). The image of the sub-surface derived from this algorithm is consistent with previous work that has ascribed thicker crust in southern highlands and thin crust in the northern lowlands (e.g. *Zuber et al.,* 2000 and many others). GRS elemental abundance data was combined with the crustal thickness model to derive the heat flow map (Figure 6.12). The crustal heat flow at the InSight landing region was consistently lower than average heat flow reported in the past for Elysium rise (e.g *McGovern et al.,* 2002; *Nimmo*, 2002). We found the crustal heat flow to be in the range of 4-6 mW/m^2 for a 30 km thick crust, however if the crust is significantly thinner, then heat-flow as low as 1 mW/m^2 can be expected (Figure 6.12). In addition to

this crustal heat flow value, there will be heat flow coming from the mantle which is not accounted for in our models.

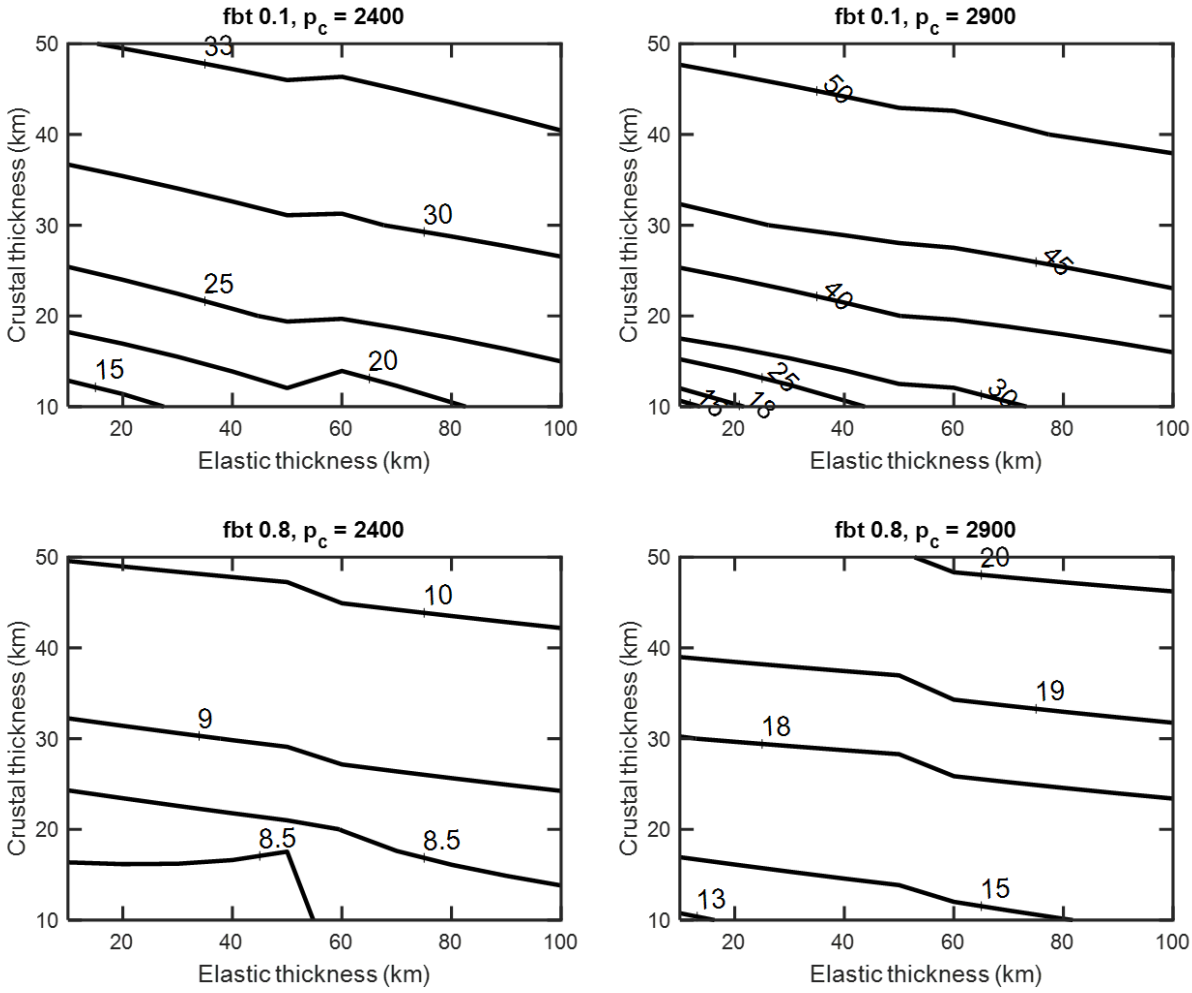

Figure 6.7: Root-mean-square between the observed and synthetic admittance spectra as a function of crustal thickness and elastic thickness, assuming mostly top-loading (fbt = 0.1) and mostly bottom loading (fbt = 0.8), and assuming top load density of 2400 kg/m^3 and 2900 kg/m^3.

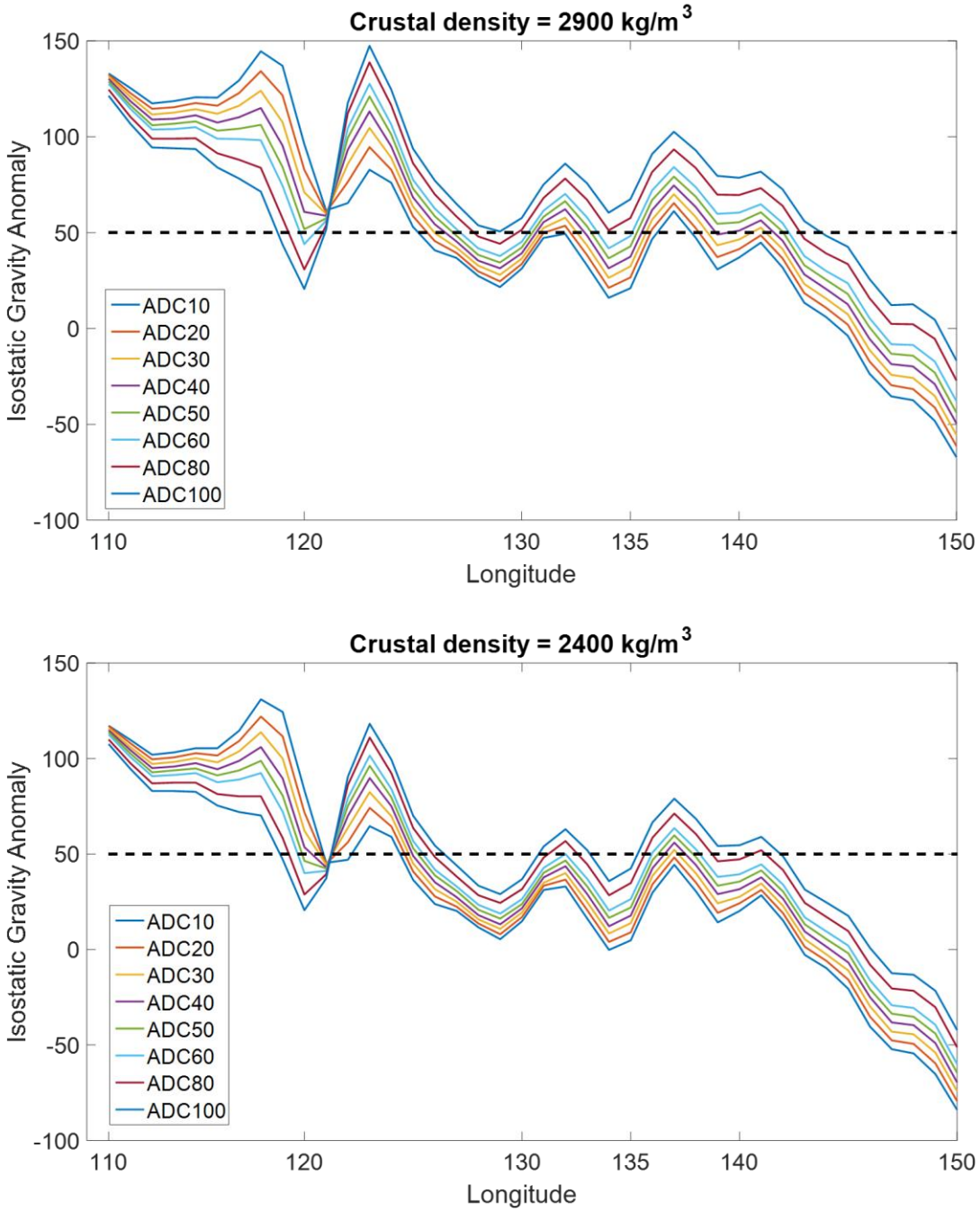

Figure 6.8: Average isostatic anomaly (2°N-7°N) as a function of longitude and the value of ADC (km) assuming two different crustal density values. For a higher value of ADC, a higher residual anomaly is observed. Anomaly under 50 mGal at 135°E is observed for depth corresponding to under 30 km (red-line).

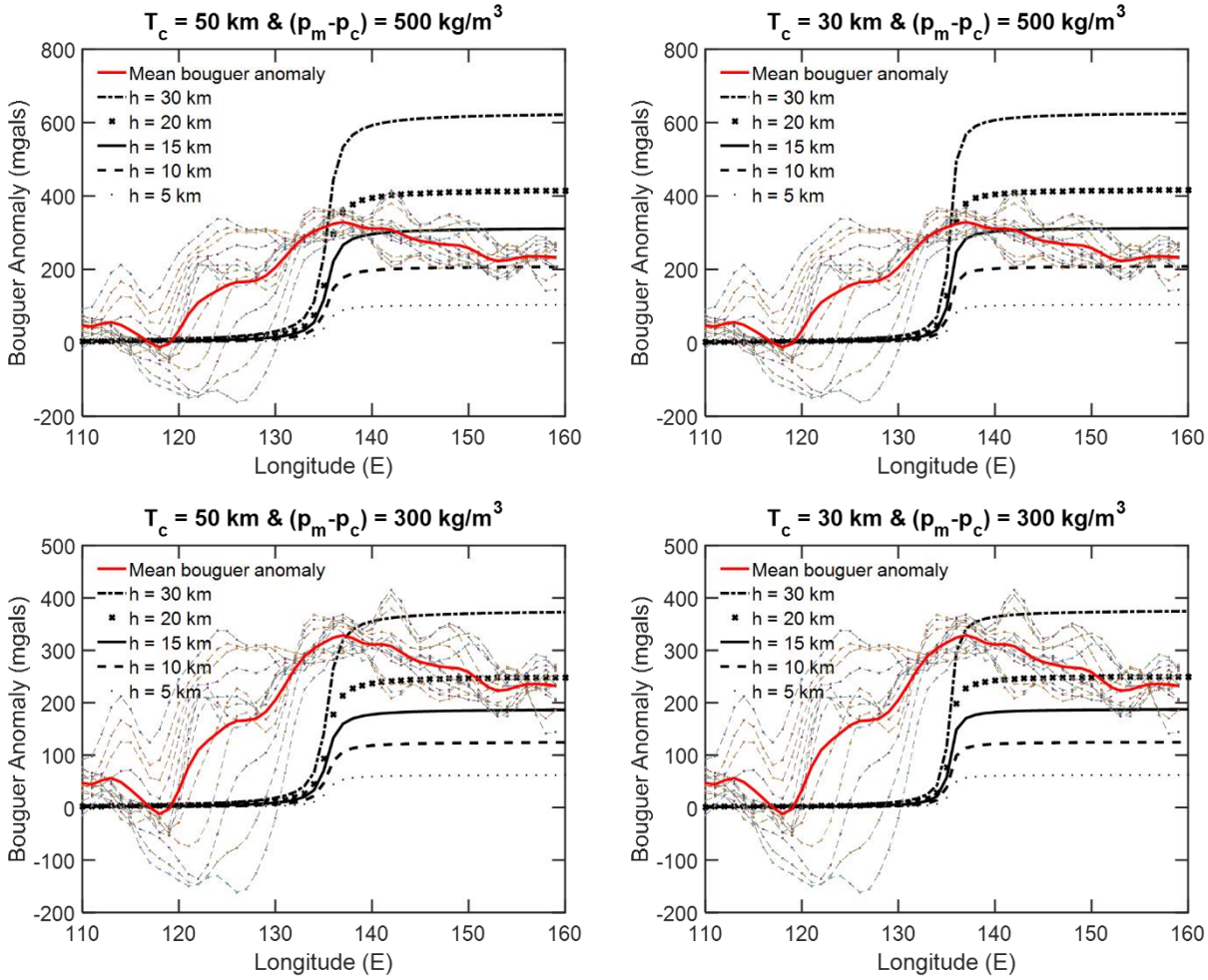

Figure 6.9: Bouguer anomaly as a function of longitude for (-2°N to 10°N in colored dotted lines), and their mean in red solid line. The result of the model assuming the schematic presented in Figure 6.4 is shown in the black line. Different values of h correspond to the crustal thickness difference.

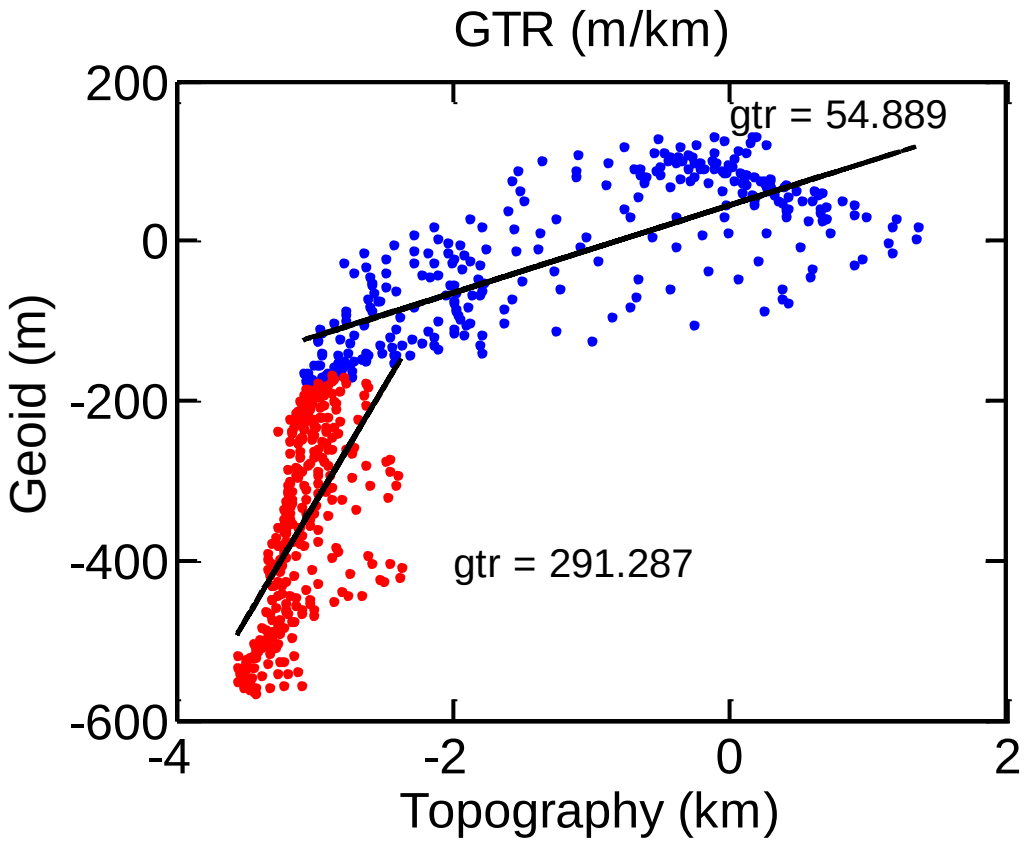

Figure 6.10: GTR for the InSight landing region; western section (2°S-10°N, 110°-135°E) in red and eastern section (2°S-10°N, 135°-160°E) in blue.

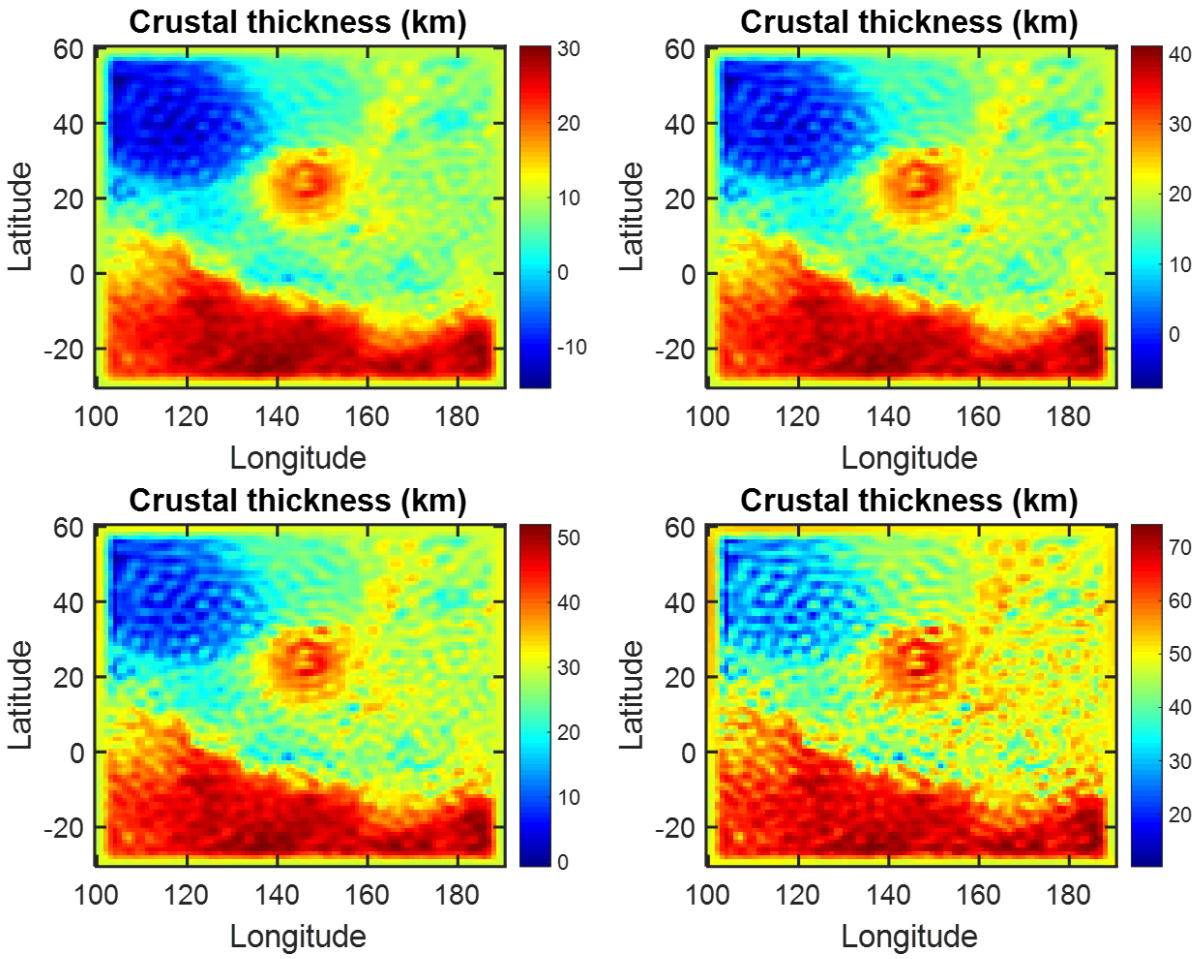

Figure 6.11: Crustal thickness estimate at for 30°S-60°N and 100°-190°E using the Parker-Oldenburg model, and assuming (from top-left to bottom right) average crustal thickness of 10 km, 20 km, 30 km and 50 km.

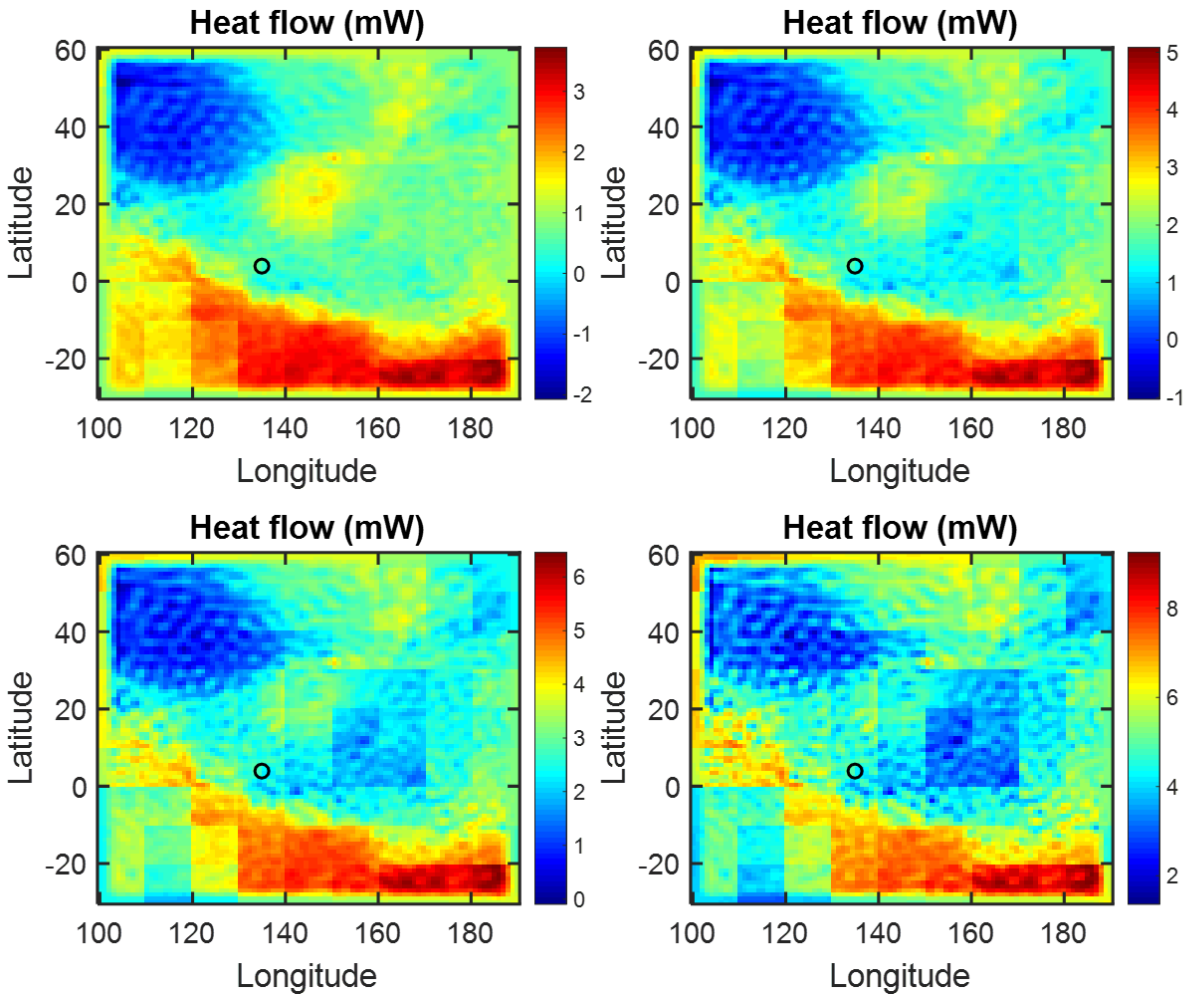

Figure 6.12: Heat flow estimate at for 30S-60N and 100-190E using 5 degree spacing GRS data and crustal thickness model derived from the Parker-Oldenburg model. In this specific model, we used the maximum value of the crustal thickness 30 km. The black circle is the location of InSight landing site.

6.6. Discussion

Various gravity/topography techniques were employed to constrain the crustal thickness at the InSight landing region and quantify the uncertainty. We find that the crust in this area is relatively thin (<30 km) compared to the average Martian crustal value of 50 km (e.g. *Zuber et al.,* 2000). The crustal thickness was found to be in the range of 17 to 27 km using global crustal thickness inversion technique assuming a single layer of crust with

density ρ_c overlying a mantle with density ρ_m. We varied the crustal density to observe the effect on the resulting crustal thickness, and observed that as the crustal density increased, the thickness increased as well (Figure 6.5). Based on the density contrast between the crust and the mantle, the moho topography changes so that the misfit between observed and modeled gravity is less than 1 mgal (*Wieczorek and Phillips* 1998), so without a more robust constraint on the crustal density of Mars each of the crustal thickness models presented here is equally likely.

The admittance spectra of the InSight landing region was compared with synthetic admittance spectra to explore the range of crustal thickness, top-load density, and loading bottom-to-top ratio. We observe that the synthetic admittance spectra corresponding to low top-load density (2400 kg/m3) and high fbt (0.8) gave lowest RMS when compared with the observed admittance spectra (Figure 6.7) and adopting a crustal thickness in the range of 10-30 km. At short wavelengths ($65<l<90$), no isostatic compensation occurs, and the admittance is a linear function of the crustal density (i.e. $Z = 2\pi G\rho_c$), where Z is admittance (*McKenzie et al.,* 2002). In this spectral range, the maximum value of the admittance spectra is ~100 mGal/km (Figure 6.6), which gives a value of ~2400 kg/m^3 for ρ_c and is consistent with our results from the forward model. Friable materials from nearby Medusa Fossae Formation or significant mantled regolith deposit could be the source of the low top-load density.

The range in crustal thickness of this region was also approximated by investigating the likely depth of compensation and isostatic anomaly. Assuming, a crustal density of 2900 kg/m^3 the isostatic anomaly was consistently under 50 mgal for ADC less than 30 km, and we found the same range of ADC to have even lower RMS when using a crustal

density of 2400 kg/m^3 (Figure 6.8) In summary, regardless of the techniques employed, the average crustal thickness in Elysium Planitia is found to be 10- to 30-km thick.

The landing site is also characterized by relatively high fbt. The best fit between synthetic admittance spectra and observed admittance spectra is for a model with fbt of 0.8. The high fbt observed here is also consistent with high Bouguer anomaly and high GTR (Figs. 9 and 10). Modeling of the Bouguer anomaly suggests that the source could likely be an intrusion of denser material at certain depth (Figure 6.6), that leads to an upward displacement (*h*) of at least 10-15 km (Figure 6.9). This could be the source of high bottom loading observed at the landing site. If this area had a significant magmatic intrusion in the past, then it may also have an additional effect on the heat flow measurement (*Kiefer*, 2004). Additionally, crustal thinning associated with rifting and subsequent inflow of mantle materials could be responsible for the Bouguer anomaly and the high bottom load. Other possible tectonic processes including metamorphism or phase change can also be responsible for the Bouguer anomaly and high bottom loading.

Nimmo (2002) found the crustal thickness of the Elysium area to be 27 km which is consistent with our results. The northern lowlands crust is estimated to be ~25 km thinner than the southern highlands (e.g. *Zuber et al.,* 2000; *Neumann et al.,* 2004). The relatively thin crustal thickness observed at Elysium Planitia implies that this region likely experienced similar geological processes as the rest of the northern lowlands of Mars. Internal processes such as mantle convection and external processes such as single or multiple large impacts could be a source of the thin crust (e.g. *Mutch et al.,* 1976; *Wise et al.,* 1979*; Wilhelms & Squyres,* 1984; *Frey & Schultz,* 1988; *Andrews-Hanna et al.* 2012). Our estimate for T_e is non-unique since a range of values shows RMS less than 10 when

we consider a high fbt and low top-load density (Figure 6.7). However, in all other cases, a low RMS is observed for T_e less than 80 km (Figure 6.7). Our limit for the T_e (10-100 km) is within the range of the low (~27 km) estimates from *McKenzie et al.,* 2002 and (~50-80 km) from *McGovern et al*., 2002, even though our area of study is much smaller and excludes Elysium Mons.

Previous studies have found that the Martian lithosphere has thickened as the planet aged and have found similarly low T_e for the northern lowlands ascribing significant heating in the past as a possible reason for the low estimate(*Breuer et al.,* 1998; *Hoogenboom & Smrekar,* 2006; *Zhong & Zuber,* 2001). The high fbt and Bouguer anomaly observed at InSight landing site could be due to significant heating of the crust in the past by a rising plume consistent with the young volcanism hypothesis usually ascribed to this region (e.g. *Platz & Michael,* 2011). However, the landing site also possesses remnant magnetization (NRM), which implies presence of an ancient crust that withstood heating beyond its Curie temperature (*Langlais et al.,* 2004). The Martian dynamo shut down ~3.8 Ga, so the presence of NRM in the crust means that all the crust cannot have been recycled or affected by heating temperature above the Curie point. The presence of NRM at this location means the presence of some ancient crust at depth. However, based on the low crustal thickness observed at this site, it is likely that massive erosion or melting must have occurred since the cessation of the internal dynamo.

The heat flow estimate based on our crustal thickness model and GRS elemental data suggests a value lower in this region than the average global heat flow on Mars (*Hahn et al.,* 2012; *McGovern et al.,* 2002) Our estimate of crustal heat flow, however, is likely a minimum estimate since the GRS instrument is only sensitive to shallow depth, and does

not include the abundance of the elemental distribution of the crust at depth. However, comparison of the heat flow measurement from InSight with our prediction will allow gross extrapolation to the rest of the planet, especially when compounded with heat-flow estimates using lithospheric loading models. If HP^3 finds that the heat flow at the InSight landing region is radically different than our (4-6 mW/m^2) or previous estimates based on T_e models (e.g. *McGovern et al.,* 2002, *Nimmo.* 2002, *McKenzie et al.,* 2002) then that suggests an additional source of heat, e.g. recent magmatic intrusion or multiple episodes of young volcanism that has enriched the crust in radiogenic elements. Additionally, a crust thicker than our estimates can also generate higher heat flow. The SEIS instrument onboard InSight will give us precise value for the crustal thickness and help resolve the additional source of heat flow if such is the situation. If the measured heat-flow from InSight is lower than our estimate, then it can likely mean that our assumption of constant distribution of radiogenic element as a function of crustal depth is likely untrue. On Earth, the distribution of radiogenic elements roughly follow an exponential decay function where the shallow surface is enriched in radiogenic elements and as depth increases the amount of radiogenic elements decrease.

6.7. Conclusion

In summary, we can make several predictions about the interior of the InSight landing region from this study. The comparison of our prediction using orbital data with *in-situ* data will allow extrapolation and refinements of our estimate of geophysical properties of the crust for the rest of the planet. Several predictions based on this paper are presented below:

(1) The crust is relatively thin (17-25 km). SEIS onboard InSight will be able to further refine the uncertainty in our estimate of the crustal thickness. The data from SEIS will not only complement our understanding of the crustal thickness, but will allow us to extrapolate and fine tune our estimate of crustal thickness for the rest of Mars.

(2) Magmatic intrusion of unknown age is likely present in the InSight landing region, based on the presence of a pronounced Bouguer anomaly and high fbt.

(3) Our heat flow estimate of the InSight landing region based on crustal thickness model and GRS elemental abundance data is ~4-6 mW/m2. HP^3 onboard InSight will provide an *in-situ* measurement of the heat flow.

(4) Based on the low-amplitude of the admittance spectra at higher spherical harmonic degree, the top-load is composed of low-density materials (~2400 kg/m^3). Friable materials from nearby Medusa Fossae Formation or significant mantled regolith deposit could be the source of the low top-load density.

CHAPTER 7

CONCLUSIONS & OUTLOOK

7.1. Conclusions

The preceding chapters have demonstrated the huge role water plays in the formation of life and evolution of the planets. High-resolution images from MRO's HiRISE and CRISM cameras have provided evidence for present day brines on Mars. The spectral detection of oxychlorine salts from present day brines on Mars raises several important questions regarding the potential habitability of these regions. While hygroscopic salts provide the only known refuge for life in the hyperarid core of the Atacama Desert, it is unknown if the water activity in the perchlorate brines on Mars may be able to support terrestrial life (*Rummel et al.,* 2014). The water-ice-rich ejecta from recent impact craters on Mars also shows spectral evidence for oxychlorine salts. The source of the oxychlorine salts is unknown, but regardless, their presence helps explain the widespread distribution and stability of ice on Mars. Further work focused on constraining the concentration of the oxychlorine brine will be an important step towards the astrobiological characterization of these unique sites on Mars.

HiRISE has only imaged ~2% of the Martian surface, so it is likely that RSL are much more widespread than currently observed. If such is the case, then it raises several important questions about the source and the total volume of water. Furthermore, numerical modeling suggests a much higher amount of water in the sub-surface (*Huber et al.,* submitted). If such is the case, the sub-surface of Mars would be much more conducive to sustaining life. Higher volume of water in the subsurface may also lead to slope failure, and some of the topographic slumps may be explained this way (see chapter 7.2.2.).

To date, NASA's *Kepler* spacecraft (*Borucki et al.,* 2010) has found nearly 5000 exoplanets out of which 21 are known to resemble the terrestrial planets in terms of their density, size and position in the habitable zone (e.g. *Burke et al.,* 2013). Water-ice and complex carbon molecules have been observed in the interstellar clouds (e.g. *Ehrefreund et al.,* 2000), so it is possible that some of the exoplanets in their habitability zone contain both these volatiles. If such is the case, did life ever arise in those planets? Do the exoplanets still retain these volatiles? Or are the exoplanets more similar to Venus where a rapid runaway greenhouse effect has led the planet to be bone dry? A complete understanding of planetary evolution and the water cycle on our terrestrial planets is imperative for assessing the habitability of these exoplanets. In the early days of solar system formation, Venus, Earth and Mars likely formed through similar accretionary processes, but they have clearly evolved differently. The three planets most likely had a similar inventory of water and other volatiles, but only one of these planets currently harbors life. While it is abundantly clear that the terrestrial planets once had a huge amount of water on their surfaces in the past, the loss mechanism for Venus and Mars is not completely understood. One proposed mechanism for the loss of water from the Martian surface is higher heat flow during the Noachian period (e.g. *Schubert et al.,* 1979). HP^3 onboard InSight will be able to shed new light on the possibility of this water loss mechanism.

7.2. Ongoing & Future Work:

7.2.1. Distribution of oxychlorine salts on Mars:

Oxychlorine salts have been found in Noachian sedimentary rocks which suggest their involvement in the Martian water cycle more than 3.8 Gy ago (*Ming et al.,*

2014). Oxychlorine salts were also discovered at the Phoenix landing site, and were thought to play a major role in the water cycle (*Zent et al., 2010*). Chapter 4 describes the spectral characteristics of RSL, which suggest that oxychlorine salts also play a huge role in the formation of modern day brines on Mars. The discovery of oxychlorine salts near impact excavated ice in chapter 5 also suggests the possibility that the mid-latitude ice is not pure water ice, but rather a frozen brine. The presence of oxychlorine salts in the contemporaneous and paleo water cycle may have huge implications for habitability. While a liquid medium is necessary for life, brines composed of oxychlorine salts can be toxic (*Rummel et al.,* 2014). A detailed study focused on the concentration, distribution and diversity of oxychlorine salts on the present-day Martian surface will be crucial towards understanding the contemporaneous habitability on Mars.

The distribution of oxychlorine salts on the Martian surface can be studied by examining CRISM images in the IR region. Oxychlorine salts are much easier to detect in their hydrated phases, so a focused search for oxychlorine salts near known ice deposits may lead to new understanding about their diversity. Application of the "band-detection" algorithm described in chapter 4 would aid in the search for oxychlorine salts on the CRISM images. This automatic detection program has led to the detection of oxychlorine salts on RSL slopes (*Ojha et al.,* 2015) and in the icy ejecta from impact events on Mars (*Ojha et al.,* submitted), and has been utilized to provide spectral evidence for mud volcanoes on Mars (*Komatsu et al.,* 2016). In fact, application of this automated algorithm have already produced some of the best spectra of oxychlorine salts on Mars (Figure 7.1.). Utilization of this automated program to further characterize the distribution of other

minerals such as carbonates on Mars is a natural next step after the completion of the global search of oxychlorine species.

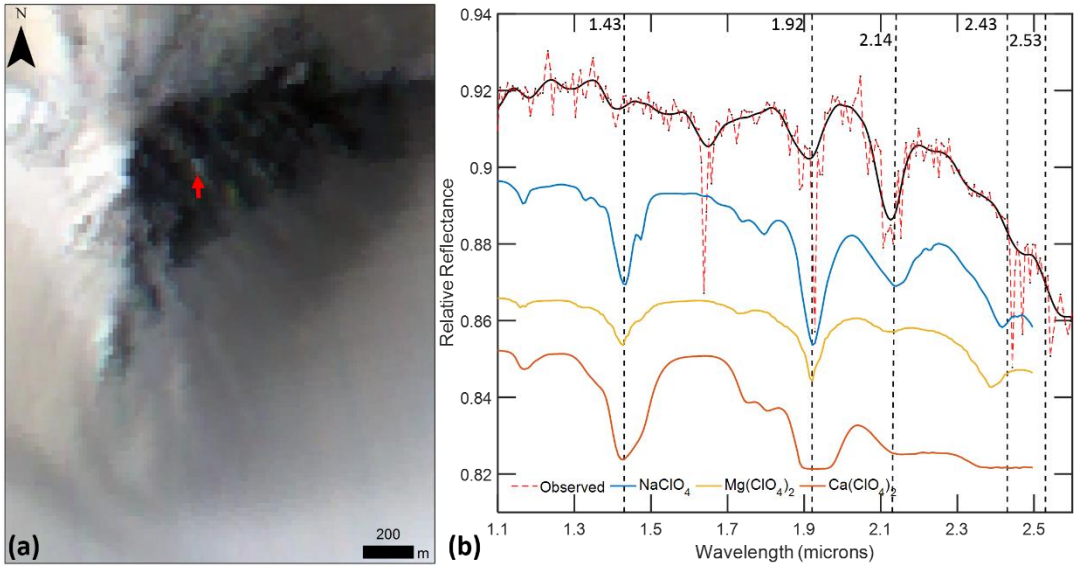

Figure 7.1. CRISM observation of a hill in Juventae Chasma. **(a)** Map-projected view of the hill in FRS00031402. The colored arrow points to the location of the observed spectrum shown in (b). **(b)** Normalized reflectance spectrum from the point denoted by the red arrow in (a). Laboratory spectra of various monohydrate oxychlorine salts are also plotted. The absorption-like feature at ~1.6 μm is an artifact due to a detector filter boundary.

7.2.2. Surface Erosion on Mars due to liquid water activity:

The slopes of Valles Marineris (VM) host hundreds of thousands of RSL (*McEwen et al.*, 2014). Atmospheric hazes have also been observed in the low-lying areas of equatorial Valles Marineris, since early images of Mars in the 1970s. In one instance, MRO observed atmospheric haze in the low-lying areas of Juventae chasma (Figure 7.2). Spectroscopic analysis of the hazes provides evidence for the presence of water ice in the form of near-surface fog. High-resolution images taken after 43 sols indicate a dark topographic slump formed during that time (Figure 7.3); the fading rate of the slump is consistent with the fading rate of recurring slope lineae on Mars, implying a possible role

of volatiles in its formation. Prior to the fog event, spectroscopic evidence for deliquescent salts is also observed on these slopes (Figure 7.1), which may provide a pathway for a viable water recharge mechanism. Based on the temporal and spatial proximity between the atmospheric water ice, deliquescent salts, and the topographic slump, it is likely that water may have played a role in the slump's formation.

There are also numerous pre-existing topographic slumps in proximity to the one we observed here (Figure 7.4.). Based on the similar scale and morphology of the older slumps, it is likely that the same processes were responsible for their formation. If indeed these slumps are created by the action of water on Mars, then water seems to not only be present on Mars, but also seems to play an active role in contemporary landscape erosion, fundamentally changing our view of the present day mass wasting processes on Mars.

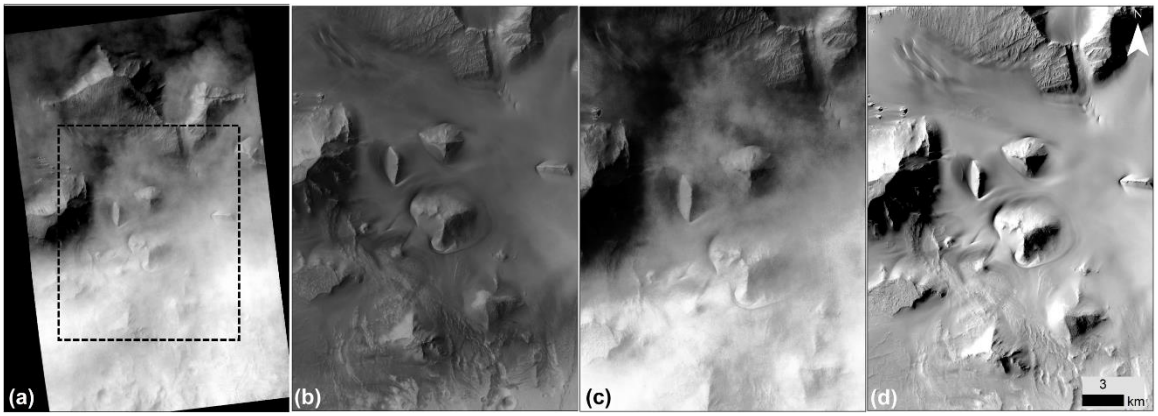

Figure 7.2. Context camera (CTX) view of the low-altitude fog in Juventae chasma. **(a)** CTX image F19_043309_1753_XN_04S061W of a portion of Juventae chasma (4.7°S, 61.4°W), showing the hills in the center and bright haze that is obscuring the view. Black rectangle shows the zoomed view presented in (b)-(d). **(b)-(d)** F17_042597_1758, F19_043309_1753, and F21_043876_1744 respectively showing the same place as the location of the black box in (a). The acquisition times for (b) to (d) are L_s/Sol: 34/69, 58/123, and 78/166. (b) and (d) show the sand-encircled hills under haze-free conditions.

Further seasonal monitoring of this activity in the canyons of Valles Marineris may allow quantitative estimates of the yearly water-driven erosion rate in this region. HiRISE and CRISM investigation of other sites with low-lying haze will be able to provide more evidence of water-ice clouds on Mars and if they play any role in the formation of RSL and other slumps alike.

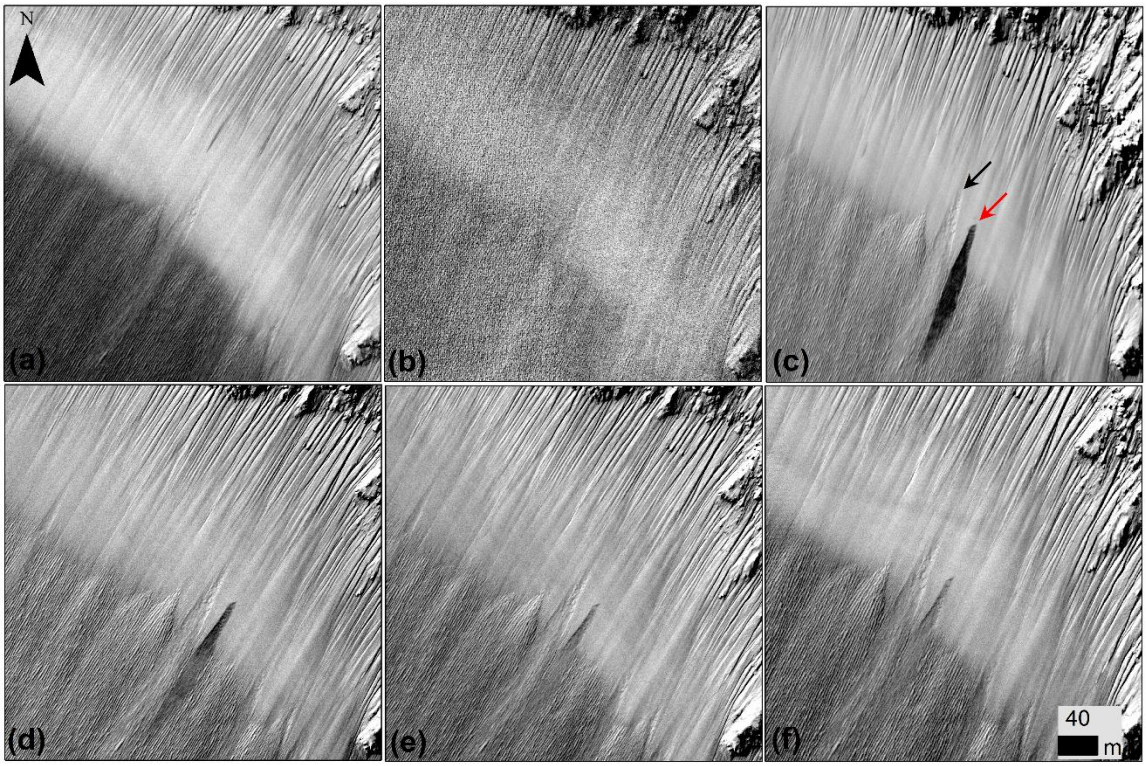

Figure 7.3. Repeat imaging of the region in Juventae chasma by HiRISE. **(a) - (f)** HiRISE view of ESP_042597_1755 (sol: 69 of Mars Year 33), ESP_043309_1755 (sol: 123), ESP_043876_1755 (sol: 166), ESP_044153_1755 (sol: 187), ESP_044364_1755 (sol: 203), ESP_044997_1755 (sol: 251). The fog is observed in (b) at sol 123, and a new topographic slump is observed in the next image acquired by HiRISE (c), after 43 sols (red arrow). The black arrow shows a faded slump with similar morphology.

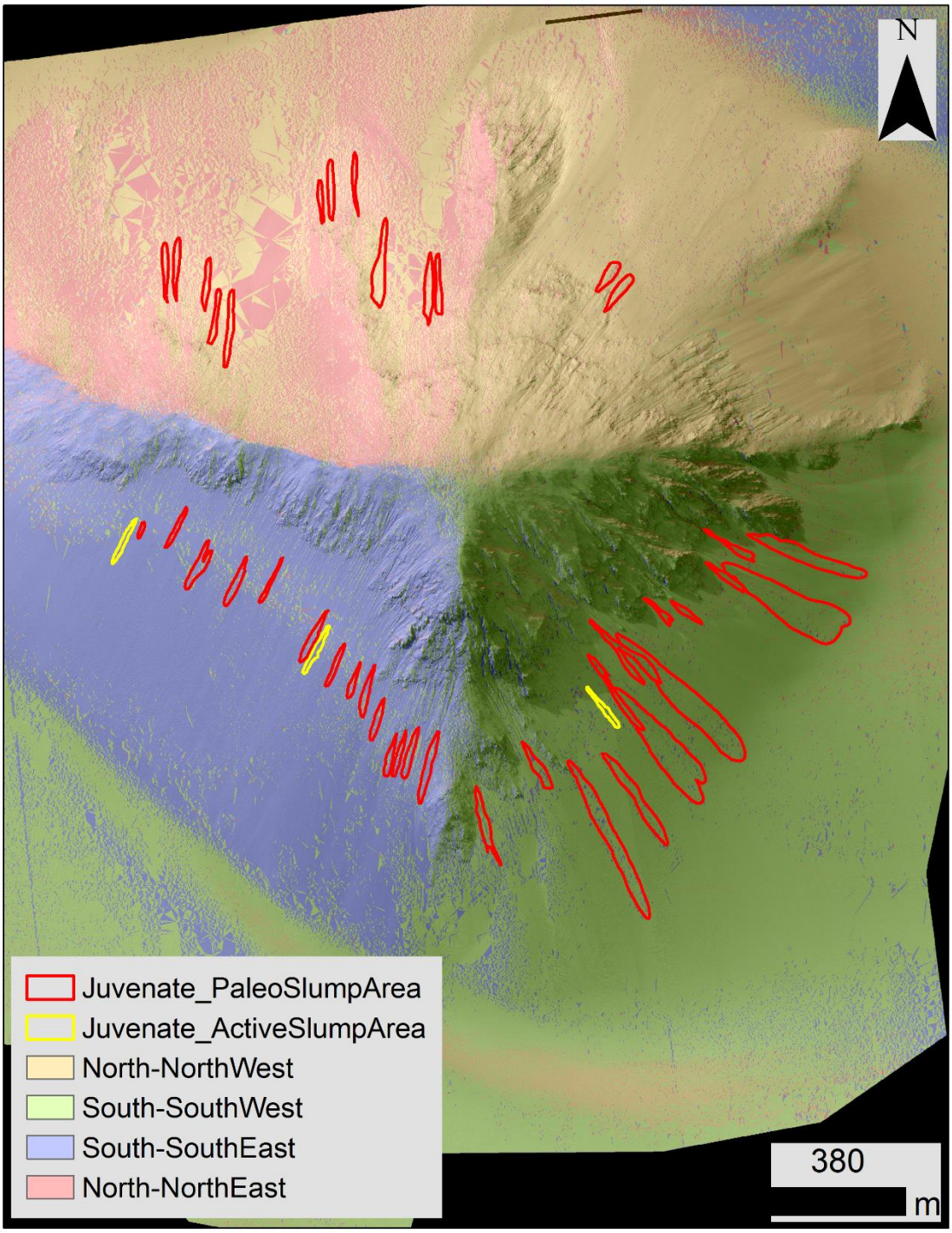

Figure 7.4. Slumps observed on a hill in Juventae chasma and their spatial distribution. Slope aspect map in color, overlaid by mapped paleo and active slumps in Juventae chasma.

Table. 3.1. Location and CRISM ID of locations surveyed for RSL mineralogy

Palikir Crater (Confirmed)	**Lat(S) 41.6**	**Lon(E) 202**	**Notes**		
CRISM Image	**Ls**	**Sensor**		**Numerator_ROI(Lat(S)/Lon(E)/No. of pixels)**	**Denominator_ROI(Lat(S)/Lon(E)/No. of pixels)**
0001D179 0001DECC 0002038F 0001F66E 0001E50D 0001E24D	247 282 359 336 302 292	S S S, L S S S, L	Both 530 and 950 nm absorption present. Band depth and reflectance fluctuation with season.	41.63/-157.71/86	41.59/-157.73/107
Tivat Crater (Confirmed)	**Lat(S) 45.9**	**Lon(E) 9.5**	**Notes**		
CRISM Image	**Ls**	**Sensor**			
0001F2DF 0001F854 0002096C 0001Ef22 000127AE 0001DD81	331 339 10 324 259 278	S, S S, S S,L S	Changing reflectance and band depth of the 530 and 950 nm	45.94/9.55/84	45.8/9.51/112
Raga Crater (Confirmed)	**Lat(S) 48.1**	**Lon(E) 242.5**	**Notes**		
CRISM Image	**Ls**	**Sensor**			
000202F3 0001CEEB 00013E58 0001F002	358 217 308 326	S, S, L, S	Concave profile for the 530nm absorption and 950 nm. Changing band depth and reflectance with season.	48.12/117.56/224	48.1/117.54/333

Table 3.1. Continued

Corozal Crater (Confirmed)	**Lat(S) 38.8**	**Lon(E) 159.5**	**Notes**		
CRISM Image	**Ls**	**Sensor**			
0001D81A 000200D4 0001E44C 0001F015 00024D78	263 355 300 325 107	S S S S S	24D78 has much higher reflectance. Small 530 nm absorption observed, but no definite absorption at 950 nm.	38.82/159.51/367	38.85/159.54/568
Asimov Crater_1 (Confirmed)	**Lat(S) 47.6**	**Lon(E) 4.6**	**Notes**		
CRISM Image	**Ls**	**Sensor**			
0009216 0002158b	11 30	S S, L	530 nm absorption observed Changing band depth and reflectance. Pattern unclear. No absorption at 950 nm.	47.74/4.61/76	47.80/4.61/118
Central Hills on a crater (Confirmed)	**Lat(S) 43.2**	**Lon(E) 343.2**	**Notes**		
CRISM Image	**Ls**	**Sensor**			
0001E53E 0001EA13 00207F1	302 312 8	S S S	No definite 530 nm in two of the three VNIR. No 950 nm absorption in any of the three. Reflectance increases with season.	43.31/-16.78/175	43.37/-16.75/266
Asimov Crater_2 (Confirmed)	**Lat(S) 46.9**	**Lon(E) 5.1**	**Notes**		
CRISM Image	**Ls**	**Sensor**			
0002091C 00012C49	10 269	S S, L	530 nm and 950 nm present in both images. 2100 nm absorption also observed.	46.90/5.05/200	46.86/5.09/267

			Table 3.1. Continued		
Unnamed Crater (Confirmed)	**Lat(S) 38.1**	**Lon(E) 224**	**Notes**		
CRISM Image	**Ls**	**Sensor**			
0001FF2E 0001F9D9 0001E7E6	353 341 308	S S S	530 nm absorption and 950 nm. L_s 353 has the deepest band depth for 530nm.	38.18/-136.01/344	38.08/-136.02/348
Hellas Floor (Partially Confirmed)	**Lat(S) 38.1**	**Lon(E) 224**	**Notes**		
CRISM Image	**Ls**	**Sensor**			
0001F0D1 000201BF	327 356	S S	No definite 530 nm or 950 nm absorption.	39.60/-88.1/84	39.65/-88.04/104
Horowitz Crater (Confirmed)	**Lat(S) 32**	**Lon(E) 140.8**	**Notes**		
CRISM Image	**Ls**	**Sensor**			
0001D45D 0001F9EB 00008573	254 342 334	S S S, L	Concave 530 nm absorption. Changing band depth. 950 nm absorption unclear. Changing reflectance.	32.05/140.83/48	32.08/140.82/56
High Latitude Crater (Confirmed)	**Lat(S) 52.3**	**Lon(E) 157.7**	**Notes**		
CRISM Image	**Ls**	**Sensor**			
000140E3 0001E708 0001ED8D 0001C17E	314 306 322 187	S S S S	530 nm absorptions	52.34/157.67/100	52.31/157.45/167
Rabe Crater (Confirmed)	**Lat(S) 43.7**	**Lon(E) 34.1**	**Notes**		

			Table 3.1. Continued		
CRISM Image	**Ls**	**Sensor**			
00012527 0001E811 0001E4F4	256 308 302	S, L S S	530 nm absorption observed. 950 nm absorption unclear.	-43.85/32.23/35	-43.72/34.2/46
Hale Crater (Confirmed)	**Lat(S) 35.7**	**Lon(E) 323.5**	**Notes**		
CRISM Image	**Ls**	**Sensor**			
000204FE 00028DC4 000117BC 000209F8	3 278 223 11	S S, L S, L S	530 nm and 950 nm absorption observed. No hydration signature observed in the IR portion.	Multiple images cover wide area. No one consistent ROI.	Multiple images cover wide area. No one consistent ROI.
Well Preserved Crater (Confirmed)	**Lat(S) 37.1**	**Lon(E) 192.1**	**Notes**		
CRISM Image	**Ls**	**Sensor**			
0001E79A 0001F986 00020340 00022389 00008FA4 00011106	307 341 358 52 8 210	S S S S S, L S, L	Spatial Extent of RSL too small here, but the slopes are still dominated by 530 and 950 nm	ROIs different for different images. RSL spatial extent too small.	ROIs different for different images. RSL spatial extent too small.
Crater on Coprates Floor (Confirmed)	**Lat(S) 14.1**	**Lon(E) 296.9**	**Notes**		

			Table 3.1. Continued		
CRISM Image	**Ls**	**Sensor**			
00027159 00028ED2 00024F86 00028DE9	192 281 110 278	S S, L S L, S	VNIR show 530 nm absorption and a slight 950 nm absorption.	-11.52/-69.66/128	-11.52/-69.62/144
Coprates Slopes and Dunes (Confirmed)	**Lat(S) 13.9**	**Lon(E) 296.8**	**Notes**		
CRISM Image	**Ls**	**Sensor**			
00027D93 000285FF 00028CA7 00029258	226 254 271 288	S S S S	530 nm and 950 nm absorption observed on some RSL slopes. RSL too small here.	Multiple ROIs including some in dunes.	Multiple ROIs including some in dunes.
S of Large Impact in Coprates (Confirmed)	**Lat(S) 12.6**	**Lon(E) 294.7**	**Notes**		
CRISM Image	**Ls**	**Sensor**			
00027C4A 0002953A 000298D0 00029D33	222 318 327 336	S S S S	530 nm and 950 nm absorption observed.	-12.69/-66.72/144	-12.65/-66.75/162
Elorza Crater Central Pit (Confirmed)	**Lat(S) 8.8**	**Lon(E) 304.8**	**Notes**		
CRISM Image	**Ls**	**Sensor**			
00008236 00016849 0001D162 0001FF7A 0002195C 000227AB	328 52 247 353 31 58	L, S L, S L, S S S S	530 nm absorption observed in some CRISM images. Spectra otherwise flat at this location. Weak 2100 nm absorption in few spectra.	8.79/-55.19/27	8.73/-55.14/27

			Table 3.1. Continued		
Juventae Chasma (Confirmed)	**Lat(S) 4.7**	**Lon(E) 298.6**	**Notes**		
CRISM Image	**Ls**	**Sensor**			
00028B7A 00028D56 0002955D 00029904	268 275 318 327	S L, S S S	530 nm and 950 nm absorption observed on multiple RSL slopes. No hydration signature found in IR.	Multiple ROIs. Active RSL on all slope aspects.	Multiple ROIs. Active RSL on all slope aspects.

Table 4.1. CRISM ID and locations for hydrated salts on RSL slopes

HiRISE_ID	**CRISM_ID**	**L_s^o**	**Approximate co-ordinates of RSL in CRISM (Samples/Lines)**
Palikir Crater (-41.6^{o}N, 202.3^{o}E)			
G11_022478_1382_XN_41S157W*	FRT0000E24D	292	N/A
ESP_024034_1380	FRT0002038F	359	335/218, 335/226, 335/232, 336/218, 336/242, 336/247
ESP_030891_1380	FRT00028CEB	273	N/A
ESP_031102_1380	FRT00028FE2	283	N/A
ESP_032381_1380	FRS00029F0C	340	312, 58
Horowitz Crater (-32.0^{o}N, 140.8^{o}E)			
PSP_005787_1475 (Fig 2.a)	FRT00008573	334	379,233
PSP_005787_1475 (Fig 2.b)	FRT00008573	334	339,73
Coprates Chasma (-14.7^{o}N, 304.6^{o}E)			
ESP_031019_1650	FRS00028E0A	279	Multiple location with 1.9 absorption in the fan. See Fig. 4.
Hale Crater (-35.7^{o}N, 323.5^{o}E)			
ESP_032416_1440	FRS00029F84	342	335,96-98

Table 4.2. CRISM ID and location of non-RSL slopes.

HiRISE_ID	**CRISM_ID**	**L_s^o**	**Approximate co-ordinates of denominator and non-RSL region (in italics) in CRISM un-projected (Samples/Lines)**
Palikir Crater (-41.6^{o}N, 202.3^{o}E)			
ESP_024034_1380	FRT0002038F	359	*317/221, 316/216, 316/210, 315/209, 345/291, 345/285 345/278, 345/276* 336/30-54 335/30-54
ESP_032381_1380	FRS00029F0C	340	312, 5-20
Horowitz Crater (-32.0^{o}N, 140.8^{o}E)			
PSP_005787_1475 (Fig. 2a)	FRT00008573	334	379/352-358
PSP_005787_1475 (Fig. 2b)	FRT00008573	334	339/37-43
Coprates Chasma (-14.7^{o}N, 304.6^{o}E)			
ESP_031019_1650	FRS00028E0A	279	Multiple location with 1.9 absorption in the fan. Multiple denominators used.
Hale Crater (-35.7^{o}N, 323.5^{o}E)			
ESP_032416_1440	FRS00029F84	342	335/54-60

Table 5.1. List of craters that excavated ice in the mid-latitudes of Mars.

	Latitude (Planetocentric)	Longitude (East)	Visible Ice?
Site N1	-50.59	305.98	No
Site N2	-50.16	70.09	No
Site N3	40.37	136.58	No
Site N4	37.48	222.26	No
Site N5	38.94	123.71	No
Site N6	40.32	221.22	No
Site N7	39.57	190.05	No
Site N8	39.38	149.37	No
Site N9	38.43	293.8	No
Site N10	43.78	203.31	No
Site N11	36.92	148.3	No
Site N12	35.52	36.35	No
Site N13	39.3	293.79	No
Site N14	38.65	280.24	No
Site N15	40.34	185.5	No
Site N16	54.77	196.85	No
Site N17	46.61	133.71	No
Site N18	36.01	282.01	No
Site N19	37.34	182.19	No
Site N20	49.35	189.67	No
Site N21	40.42	77.6	No
Site N22	35.32	201.37	No
Site N23	-74.51	157.89	No
Site N24	40.9	222.71	No
Site N25	38.68	210.41	No
Site N26	45.02	203.23	No
Site N27	46.8	149.51	No
Site N28	50.93	221.94	No
Site N29	39.12	21.38	No
Site N30	50.36	232.9	No
Site N31	37.24	36.01	No
Site N32	42.06	205.24	No
Site N33	41.4	206.81	No
Site N34	44.34	172.3	No
Site N35	44.75	232.11	No
Site N36	55.57	240.52	No
Site N37	43.13	204.81	No

Table 5.1. Continued

Site N38	54.36	228.54	No
Site N39	42.77	204.27	No
Site N40	42.46	151.01	No
Site N41	-55.87	264.76	No
Site N42	49.91	270.24	No
Site N43	35.27	191.2	No
Site N44	100	37.39	No
Site N45	43.05	164.78	No
Site N46	37.17	104.53	No
Site N47	43.94	173.75	No
Site N48	37.41	56.26	No
Site M1	41.02	126.3	Unlikely
Site M2	47.72	225.13	Unlikely
Site M3	40.12	157.93	Possible
Site M4	53.58	228.3	Possible
Site M5	52.95	50.87	Likely
Site M6	46.62	171.88	Likely
Site M7	57.24	358.02	Likely
Site M8	39.56	202.42	Possible
Site 1	46.35	176.89	Yes
Site 2	43.3	164.21	Yes
Site 3	55.58	150.6	Yes
Site 4	45.07	164.7	Yes
Site 5	46.18	188.5	Yes
Site 6	50.67	278.4	Yes (CTX)
Site 7	44.22	164.2	Yes
Site 8	44.35	152.92	Yes
Site 9	63.92	44.88	Yes
Site 10	53.27	46.26	Yes
Site 11	50.51	265.2	Yes
Site 12	64.29	231.5	Yes
Site 13	60.99	238.72	Yes
Site 14	43.9	204.35	Yes
Site 15	50.78	208.76	Yes
Site 16	50.37	219.71	Yes
Site 17	52.01	214.7	Yes
Site 18	39.11	190.25	Yes
Site 19	-71.51	191.53	Yes
Site 20	-73.69	250.62	Yes
Site 21	68.54	358.53	Yes

Table 5.1. Continued			
Site 22	65.06	220.5	Yes
Site 23	57.33	234.2	Yes
Site 24	69.47	80.44	Yes
Site 25	74.64	49.56	Yes
Site 26	55.62	241.24	Yes
Site 27	63.68	251.45	Yes
Site 28	-62.54	76	Yes (CTX)
Site 29	-57.36	125.17	Yes
Site 30	-65	329.84	Yes
Site 31	42.58	189.02	Yes

"Yes (CTX)" implies bright CTX pixel interpreted as ice, but not definite bright ice by the time of HiRISE imaging.

Table 5.2. CRISM ID of icy sites investigated in Chapter 5

CRISM ID	**HiRISE ID**	**MY**	**Ls**	**Sol**
Site–I (55.6N, 150.6E)				
FRT0000D2F7	PSP_010625_2360	29	151	319
FRT00010274	ESP_011337_2360	29	180	372
FRT000107CF	ESP_011548_2360	29	190	389
Site-II (44.2N, 164.2E)				
FRT0001719F	ESP_016954_2245	30	62	130
HRS00018E54	ESP_017877_2245	30	92	200
FRT00021F8C	ESP_025314_2245	31	46	96
Site-III (39.1.2N, 190.3.2E)				
FRS0002755E	ESP_029256_2195	31	193	395
FRT00030271	ESP_036772_2195	32	138	296

REFERENCES

Aharon O., Bardavid R. E., Mana L. Perchlorate and halophilic prokaryotes: implications for possible halophilic life on Mars. *Extremophiles* **18**, 75-80 (2014).

Altheide T., Cheverier V. F., Nicholson C., Denson J. Experimental investigation of the stability and evaporation of sulfate and chloride brines on Mars. *EPSL* **282**, 69-78, (2009).

Andreas, Edgar L. "New estimates for the sublimation rate for ice on the Moon." *Icarus* 186.1 (2007): 24-30.

Andrews-Hanna, J. C. (2012). The formation of Valles Marineris: 2. Stress focusing along the buried dichotomy boundary. *Journal of Geophysical Research: Planets*, *117*(E4), http://doi.org/10.1029/2011JE003954

Baker, V. R., et al. "Ancient oceans, ice sheets and the hydrological cycle on Mars." *Nature* 589-594: (1991).

Baker, Victor R. "The channels of Mars." *University of Texas Press, 1982. 204 p.* (1982).

Bibring, Jean-Pierre, et al. "Global mineralogical and aqueous Mars history derived from OMEGA/Mars Express data." *Science* 312.5772 (2006): 400-404.

Bills, B. G., & Ferrari, A. J. (1978). Mars topography harmonics and geophysical implications. *Journal of Geophysical Research*, *83*(B7), 3497. http://doi.org/10.1029/JB083iB07p03497

Bills, B. G., & Nerem, R. S. (1995). A harmonic analysis of Martian topography. *Journal of Geophysical Research*, *100*(E12), 26317. http://doi.org/10.1029/95JE03101

Bishop J. L., Quinn R., and Darby Dyar M.. Spectral and thermal properties of perchlorate salts and implications for Mars. *American Mineralogists* **99,** 1580-1592 (2014).

Borucki, W. J., Koch, D., Basri, G., Batalha, N., Brown, T., Caldwell, D., … Prsa, A. (2010). Kepler Planet-Detection Mission: Introduction and First Results. *Science*, *327*(5968), 977–980. http://doi.org/10.1126/science.1185402

Boynton, W. V *et al.* Distribution of hydrogen in the near surface of Mars: evidence for subsurface ice deposits. *Science* 297, 81–85 (2002).

Boynton, W. V., Feldman, W. C., Mitrofanov, I. G., Evans, L. G., Reedy, R. C., Squyres, S. W.,Ton'chev, A. K. (2004). The Mars Odyssey Gamma-Ray Spectrometer Instrument Suite. *Space Science Reviews*, *110*, 37–83. http://doi.org/10.1023/B:SPAC.0000021007.76126.15

Boynton, W. V., Taylor, G. J., Evans, L. G., Reedy, R. C., Starr, R., Janes, D. M., … Hamara, D. K. (2007). Concentration of H, Si, Cl, K, Fe, and Th in the low- and mid-latitude regions of Mars. *Journal of Geophysical Research E: Planets*, *112*(12). http://doi.org/10.1029/2007JE002887

Brack, André. "L'exobiologie ou l'origine chimique de la vie." *Formation planétaire et exoplanètes* (2006): 309-332.

Breuer, D., Yuen, D. A., Spohn, T., & Zhang, S. X. (1998). Three dimensional models of Martian mantle convection with phase transitions. *Geophysical Research Letters*, *25*(3), 229–232. http://doi.org/10.1029/97GL03767

Brown, Peter G., et al. "The fall, recovery, orbit, and composition of the Tagish Lake meteorite: A new type of carbonaceous chondrite." *Science*290.5490 (2000): 320-325.

Burke, C. J., Bryson, S. T., Mullally, F., Rowe, J. F., Christiansen, J. L., Thompson, S. E., & Coughlin, J. L. (2013). Planetary candidates observed by Kepler IV: Planet sample from Q1-Q8 (22 months). *The Astrophysical Journal Supplement*, *210*(2), A19. http://doi.org/10.1088/0067-0049/210/2/19

Butler, Bryan J., Duane O. Muhleman, and Martin A. Slade. "Mercury: full-disk radar images and the detection and stability of ice at the North Pole."*Journal of Geophysical Research: Planets* 98.E8 (1993): 15003-15023.

Byrne, S. *et al.* Distribution of mid-latitude ground ice on Mars from new impact craters. *Science* 325, 1674–1676 (2009).

Cabrol, Nathalie A., and Edmond A. Grin. "Distribution, classification, and ages of Martian impact crater lakes." *Icarus* 142.1 (1999): 160-172.

Cabrol, Nathalie A., Edmond A. Grin, and Gilles Dawidowicz. "Ma'adim Vallis revisited through new topographic data: Evidence for an ancient intravalley lake." *Icarus* 123.2 (1996): 269-283.

Campbell, Donald B., et al. "Galilean satellites: 1976 radar results." *Icarus*34.2 (1978): 254-267.

Carr, M.H., 1974. The role of lava erosion in the formation of lunar rilles and Martian channels. *Icarus* 22, 1-23.

Carr, Michael H. "The Martian drainage system and the origin of valley networks and fretted channels." *Journal of Geophysical Research: Planets*100.E4 (1995): 7479-7507.

Carr, Michael H., and Gary D. Clow. "Martian channels and valleys: Their characteristics, distribution, and age." *Icarus* 48.1 (1981): 91-117.

Carr, Michael H., and Gary D. Clow. "Martian channels and valleys: Their characteristics, distribution, and age." *Icarus* 48.1 (1981): 91-117.

Carr, Michael H., and James W. Head. "Oceans on Mars: An assessment of the observational evidence and possible fate." *Journal of Geophysical Research: Planets* 108.E5 (2003).

Carter, J., et al. "Hydrous minerals on Mars as seen by the CRISM and OMEGA imaging spectrometers: Updated global view." *Journal of Geophysical Research: Planets* 118.4 (2013): 831-858.

Chapman, Clark R., and Kenneth L. Jones. "Cratering and obliteration history of Mars." *Annual Review of Earth and Planetary Sciences* 5 (1977): 515-540.

Chevrier V. F., Hanley J., Altheide T. S. Stability of perchlorate hydrates and their liquid solutions at the Phoenix landing site, Mars. *Geophys Res Lett* **36,** L10202, (2009).

Chevrier V.F. and Rivera-Valentin E.G., Formation of recurring slope lineae by liquid brines on present-day Mars. *Geophys Res Lett* **39**, L21202 (2012).

Christensen, Philip R., et al. "Detection of crystalline hematite mineralization on Mars by the Thermal Emission Spectrometer: Evidence for near-surface water." *Journal of Geophysical Research: Planets* 105.E4 (2000): 9623-9642.

Clark, R. N., Chapter 1: Spectroscopy of Rocks and Minerals, and Principles of Spectroscopy, in *Manual of Remote Sensing, Volume 3, Remote Sensing for the Earth Sciences*, (A.N. Rencz, ed.) John Wiley and Sons, New York, p 3- 58, 1999.

Cleeves, L. Ilsedore, et al. "The ancient heritage of water ice in the solar system." *Science* 345.6204 (2014): 1590-1593.

Clifford, Stephen M., and Timothy J. Parker. "The evolution of the Martian hydrosphere: Implications for the fate of a primordial ocean and the current state of the northern plains." *Icarus* 154.1 (2001): 40-79.

Clow, Gary D. "Generation of liquid water on Mars through the melting of a dusty snowpack." *Icarus* 72.1 (1987): 95-127.

Colaprete, Anthony, et al. "Detection of water in the LCROSS ejecta plume."*science* 330.6003 (2010): 463-468.

Connerney, J. E. P., et al. "The global magnetic field of Mars and implications for crustal evolution." *Geophysical Research Letters* 28.21 (2001): 4015-4018.

Craddock, Robert A., and Alan D. Howard. "The case for rainfall on a warm, wet early Mars." *Journal of Geophysical Research: Planets* 107.E11 (2002).

Crowley, J.K. Visible and near-infrared (0.4-2.5 μm) reflectance spectra of Playa evaporite minerals. *JGR* **96(B10)**, 16231-16240 (1991).

Cull S. C. *et al.* Concentrated perchlorate at the Mars Phoenix landing site: Evidence for thin film liquid water on Mars. *Geophys Res Lett* **37**, L22203, (2010).

Cutts, J. A., and K. R. Blasius. "Martian outflow channels: Quantitative comparison of erosive capacities for eolian and fluvial models." *Lunar and Planetary Science Conference*. Vol. 10. 1979.

Daubar, I. J., McEwen, A. S., Byrne, S., Kennedy, M. R. & Ivanov, B. The current martian cratering rate. *Icarus* 225, 506–516 (2013).

Daubar, I. J. *et al.* Changes in blast zone albedo patterns around new martian impact craters. *Icarus* 267, 86–105 (2016).

Davila, Alfonso F., et al. "Facilitation of endolithic microbial survival in the hyperarid core of the Atacama Desert by mineral deliquescence." *Journal of Geophysical Research: Biogeosciences* 113.G1 (2008).

Davila A. F., Hawes I., Ascaso C., and Wierzchos J. Salt deliquescence drives photosynthesis in the hyperarid Atacama Desert. *Environmental Microbio. Rep* **5(4)**, 583-587, (2013).

De Bergh, C., et al. "Water in the deep atmosphere of Venus from high-resolution spectra of the night side." *Advances in Space Research* 15.4 (1995): 79-88.

Dehouck, E., et al. "Ismenius Cavus, Mars: A deep paleolake with phyllosilicate deposits." *Planetary and Space Science* 58.6 (2010): 941-946.

Donahue, T. M., et al. "Ion/neutral escape of hydrogen and deuterium: Evolution of water." *Venus II* (1997): 385-414.

Donahue, T. M., et al. "Venus was wet: a measurement of the ratio of deuterium to hydrogen." *Science* 216.4546 (1982): 630-633.

Dundas, C. & Byrne, S. HiRISE observations of new impact craters exposing Martian ground ice. *J. Geophys. Res. Planets* 109–127 (2014). doi:10.1002/2013JE004482.

Dupire, C., Menn, E. Le, Grasset, O. & Mou, S. Le. In situ infrared studies of water and CO 2 frost between 1 and 5 μ m : from. *Lunar Planet. Sci. Conf* 40, (2009).

Ehlmann, Bethany L., et al. "Orbital identification of carbonate-bearing rocks on Mars." *Science* 322.5909 (2008): 1828-1832.

Ehlmann, B.L. and Edwards, C.S. Mineralogy of the Martian Surface. *Ann. Rev. Earth Planet. Sci.* **42**; doi: 10.1146/annurev-earth-060313-055024 (2015).

Ehrenfreund, Pascale, and Steven B. Charnley. "Organic molecules in the interstellar medium, comets, and meteorites: a voyage from dark clouds to the early Earth." *Annual Review of Astronomy and Astrophysics* 38.1 (2000): 427-483.

Elsenousy A., Hanley J., Chevrier V. F., Effect of evaporation and freezing on the salt paragensis and habitability of brines at the Phoenix landing site. *EPSL* **421**, 39-46, (2015).

Farley, K. a. *et al.* In Situ Radiometric and Exposure Age Dating of the Martian Surface. *Science (80-.).* 1247166 (2013). doi:10.1126/science.1247166

Feldman, W. C., et al. "Fluxes of fast and epithermal neutrons from Lunar Prospector: Evidence for water ice at the lunar poles." *Science* 281.5382 (1998): 1496-1500.

Frey, H., & Schultz, R. A. (1988). Large impact basins and the mega-impact origin for the crustal dichotomy on Mars. *Geophysical Research Letters*, *15*(3), 229–232. http://doi.org/10.1029/GL015i003p00229

Frey, H. V. (2002). Ancient lowlands on Mars. *Geophysical Research Letters*, *29*(10), 0–3. http://doi.org/10.1029/2001GL013832

Glavin,D. P. *et al.* Evidence for perchlorates and the origin of chlorinated hydrocarbons detected by SAM at the Rocknest aeolian deposit in Gale Crater. *J. Geophys. Res. Planets* 118, 1955–1973 (2013).

Goettel, K. A. (1981). Density of the mantle of Mars. *Geophysical Research Letters*, *8*(5), 497–500.

Gómez-Ortiz, D., & Agarwal, B. N. P. (2005). 3DINVER.M: A MATLAB program to invert the gravity anomaly over a 3D horizontal density interface by Parker-Oldenburg's algorithm. *Computers and Geosciences*, *31*(4), 513–520. http://doi.org/10.1016/j.cageo.2004.11.004

Gough, R. V., Chevrier, V. F. & Tolbert, M. A. Formation of aqueous solutions on Mars via deliquescence of chloride-perchlorate binary mixtures. *Earth Planet. Sci. Lett.* 393, 73–82 (2014).

Greeley R and Guest JE (1987) *US Geological Survey Miscellaneous Investigation Series, I-1802-B: Geologic Map of the Eastern Equatorial Region of Mars*. Flagstaff, AZ: US Geological Survey.

Grott, M., Baratoux, D., Hauber, E., Sautter, V., Mustard, J., Gasnault, O., … Toplis, M. J. (2013). Long-term evolution of the martian crust-mantle system. *Space Science Reviews*, *174*(1-4), 49–111. http://doi.org/10.1007/s11214-012-9948-3

Grotzinger, John P., et al. "A habitable fluvio-lacustrine environment at Yellowknife Bay, Gale Crater, Mars." *Science* 343.6169 (2014): 1242777.

Grotzinger, John P., et al. "Stratigraphy and sedimentology of a dry to wet eolian depositional system, Burns formation, Meridiani Planum, Mars." *Earth and Planetary Science Letters* 240.1 (2005): 11-72.

Guest, A., & Smrekar, S. E. (2007). New constraints on the thermal and volatile evolution of Mars. *Physics of the Earth and Planetary Interiors*, *164*(3-4), 161–176. http://doi.org/10.1016/j.pepi.2007.06.010

Gulick, Virginia C. "Origin of the valley networks on Mars: A hydrological perspective." *Geomorphology* 37.3 (2001): 241-268.

Gulick, Virginia C., and Victor R. Baker. "Origin and evolution of valleys on Martian volcanoes." *Journal of Geophysical Research: Solid Earth* 95.B9 (1990): 14325-14344.

Haberle, Robert M., et al. "On the possibility of liquid water on present-day Mars." *Journal of Geophysical Research: Planets* 106.E10 (2001): 23317-23326.

Hahn, B. C., McLennan, S. M., & Klein, E. C. (2011). Martian surface heat production and crustal heat flow from Mars Odyssey Gamma-Ray spectrometry. *Geophysical Research Letters*, *38*(14). http://doi.org/10.1029/2011GL047435

Hanley J., Chevrier V. F., Berget D. J., and Adams R. D. Chlorate salts and solutions on Mars. *Geophys Res Lett* **39,** L08201, (2012).

Hanley, J. *et al.* Reflectance spectra of hydrated chlorine salts: The effect of temperature with implications for Europa. *JGR: Planets* **119**, 2370-2377 (2014).

Hanley, J., V. F. Chevrier, R. S. Barrows, C. Swaffer, and T. S. Altheide. Near- and mid-infrared reflectance spectra of hydrated oxychlorine salts with implications for Mars. *JGR: Planets*, **120**, (2015).

Harmon, J. K., and M. A. Slade. "Radar mapping of Mercury: Full-disk images and polar anomalies." *Science* 258.5082 (1992): 640-643.

Head, J. W., Mustard, J. F., Kreslavsky, M. a, Milliken, R. E. & Marchant, D. R. Recent ice ages on Mars. *Nature* 426, 797–802 (2003).

Hecht, M. H. *et al.* Detection of perchlorate and the soluble chemistry of martian soil at the Phoenix lander site. *Science* 325, 64–67 (2009).

Helbert, J., E. Hauber, and D. Reiss. "Water on the terrestrial planets."*Planets and Moons: Treatise on Geophysics* (2007): 371-420.

Hoogenboom, T., & Smrekar, S. E. (2006). Elastic thickness estimates for the northern lowlands of Mars. *Earth and Planetary Science Letters*, *248*(3-4), 830–839. http://doi.org/10.1016/j.epsl.2006.06.035

Hudson, T. L. *et al.* Water vapor diffusion in Mars subsurface environments. *J. Geophys. Res.* 112, E05016 (2007).

Hudson, T. L. & Aharonson, O. Diffusion barriers at Mars surface conditions: Salt crusts, particle size mixtures, and dust. *J. Geophys. Res.* 113, E09008 (2008).

Hynek, Brian M., Michael Beach, and Monica RT Hoke. "Updated global map of Martian valley networks and implications for climate and hydrologic processes." *Journal of Geophysical Research: Planets* 115.E9 (2010).

Ingersoll, Andrew P., Tomas Svitek, and Bruce C. Murray. "Stability of polar frosts in spherical bowl-shaped craters on the Moon, Mercury, and Mars."*Icarus* 100.1 (1992): 40-47.

Kasting, James F., Daniel P. Whitmire, and Ray T. Reynolds. "Habitable zones around main sequence stars." *Icarus* 101.1 (1993): 108-128.

Kiefer, W. S. (2004). Gravity evidence for an extinct magma chamber beneath Syrtis Major, Mars: A look at the magmatic plumbing system. *Earth and Planetary Science Letters*, *222*(2), 349–361.

Komatsu, Goro, et al. "Small edifice features in Chryse Planitia, Mars: Assessment of a mud volcano hypothesis." *Icarus* 268 (2016): 56-75.

Konopliv, A. S., Asmar, S. W., Folkner, W. M., Karatekin, Ö., Nunes, D. C., Smrekar, S. E., … Zuber, M. T. (2011). Mars high resolution gravity fields from MRO, Mars seasonal gravity, and other dynamical parameters. *Icarus*, *211*(1), 401–428. http://doi.org/10.1016/j.icarus.2010.10.004

Kounaves S., Carrier B. L., O'Neil G. D., Stroble S. T., Claire M. W. Evidence of Martian perchlorate, chlorate and nitrate in Mars meteorite EETA79001: Implications for oxidants and organics. *Icarus* **229**, 206-213, (2014).

Langlais, B., Purucker, M. ~E., & Mandea, M. (2004). Crustal magnetic field of Mars. *J. Geophys. Res.*, *109*(E2), 2008. http://doi.org/10.1029/2003JE002048

Lawrence, David J., et al. "Evidence for water ice near Mercury's north pole from MESSENGER Neutron Spectrometer measurements." *Science*339.6117 (2013): 292-296.

Lewis, John S. "Low temperature condensation from the solar nebula."*Icarus* 16.2 (1972): 241-252.

Lowrie, W. (2007). *Fundamentals of geophysics*. Cambridge University Press.

Lunine, Jonathan I. "Origin of water ice in the solar system." *Meteorites and the early solar system II* 1 (2006): 309-319.

Malin, Michael C., and Kenneth S. Edgett. "Evidence for recent groundwater seepage and surface runoff on Mars." *Science* 288.5475 (2000): 2330-2335.

Malin, Michael C., and Kenneth S. Edgett. "Evidence for persistent flow and aqueous sedimentation on early Mars." *Science* 302.5652 (2003): 1931-1934.

Martín-Torres, F. J. *et al.* Transient liquid water and water activity at Gale crater on Mars. *Nat. Geosci.* 8, 1–5 (2015).

Massé, M. *et al.* Martian polar and circum-polar sulfate-bearing deposits: Sublimation tills derived from the North Polar Cap. *Icarus* 209, 434–451 (2010).

Massé, M. *et al.* Wide distribution and glacial origin of polar gypsum on Mars. *Earth Planet. Sci. Lett.* 317-318, 44–55 (2012).

Massé M. *et al.* Spectroscopy and detectability of liquid brines on Mars. *Planetary and Space Science* **92**, 136-149 (2014).

Masursky, Harold. "An overview of geological results from Mariner 9."*Journal of Geophysical Research* 78.20 (1973): 4009-4030.

McEwen, A. S. *et al*. Mars reconnaissance orbiter's high resolution imaging science experiment (HiRISE). *JGR: Planets* **112**, 1991–2012 (2007).

McEwen, A. S. *et al.* Seasonal flows on warm Martian slopes. *Science* 333, 740–3 (2011).

McEwen, A. S. *et al.* Recurring slope lineae in equatorial regions of Mars. *Nat. Geosci.* 7, 53–58 (2013).

McGovern, P. J., Solomon, S. C., Smith, D. E., Zuber, M. T., Simons, M., Wieczorek, M. A., … Head, J. W. (2002). Localized gravity/topography admittance and correlation spectra on Mars: Implications for regional and global evolution. *Journal of Geophysical Research (Planets)*, *107*(July), 5136. http://doi.org/10.1029/2002JE001854

McKenzie, D., Barnett, D. N., & Yuan, D. N. (2002). The relationship between Martian gravity and topography. *Earth and Planetary Science Letters*, *195*(1-2), 1–16. http://doi.org/10.1016/S0012-821X(01)00555-6

McLennan, S. M. (2001). Crustal heat production and the thermal evolution of Mars. *Geophysical Research Letters*, *28*(21), 4019–4022. http://doi.org/10.1029/2001GL013743

McSween, H. Y. (1985). SNC meteorites - Clues to Martian petrologic evolution? *Reviews of Geophysics*, *23*(4), 391–416. http://doi.org/10.1029/RG024i001p00141

Mellon, M. T., Feldman, W. C. & Prettyman, T. H. The presence and stability of ground ice in the southern hemisphere of Mars. *Icarus* 169, 324–340 (2004).

Milliken, R. E. *et al.* Opaline silica in young deposits on Mars. *Geology* 36, 847–850 (2008).

Ming, D. W. *et al.* Volatile and organic compositions of sedimentary rocks in Yellowknife Bay, Gale crater, Mars. *Science (80-.).* 343, 1245267 (2014).

Mojzsis, Stephen J., T. Mark Harrison, and Robert T. Pidgeon. "Oxygen-isotope evidence from ancient zircons for liquid water at the Earth's surface 4,300 Myr ago." *Nature* 409.6817 (2001): 178-181.

Morbidelli, A., et al. "Source regions and timescales for the delivery of water to the Earth." *Meteoritics & Planetary Science* 35.6 (2000): 1309-1320.

Moses, Julianne I., et al. "External sources of water for Mercury's putative ice deposits." *Icarus* 137.2 (1999): 197-221.

Murchie, S. *et al.* Compact Connaissance Imaging Spectrometer for Mars (CRISM) on Mars Reconnaissance Orbiter (MRO). *J. Geophys. Res. E Planets* 112, E05S03 (2007).

Murphy, D. M., and Thomas Koop. "Review of the vapour pressures of ice and supercooled water for atmospheric applications." *Quarterly Journal of the Royal Meteorological Society* 131.608 (2005): 1539-1565.

Mustard, J. F., Cooper, C. D. & Rifkin, M. K. Evidence for recent climate change on Mars from the identification of youthful near-surface ground ice. *Nature* 1128, 411–414 (2001).

Mutch, T. A., Arvidson, R. E., Head III, J. W., Jones, K. L., & Saunders, R. S. (1976). *The geology of Mars*. Princeton, NJ: Princeton University Press.

Navarro-González, R., Vargas, E., de la Rosa, J., Raga, A. C. & McKay, C. P. Reanalysis of the Viking results suggests perchlorate and organics at midlatitudes on Mars. *J. Geophys. Res.* 115, E12010 (2010).

Neukum, Gerhard, and Konrad Hiller. "Martian ages." *Journal of Geophysical Research* 86.15 (1981): 3097-3121.

Neumann, G. A., Zuber, M. T., Wieczorek, M. A., McGovern, P. J., Lemoine, F. G., & Smith, D. E. (2004). Crustal structure of Mars from gravity and topography. *Journal of Geophysical Research E: Planets*, *109*(8). http://doi.org/10.1029/2004JE002262

Nimmo, F. (2002). Admittance estimates of mean crustal thickness and density at the Martian hemispheric dichotomy. *Journal of Geophysical Research: Planets*, *107*(E11), 27–1–27–6. http://doi.org/10.1029/2000JE001488

Nozette, Stewart, et al. "Integration of lunar polar remote-sensing data sets- Evidence for ice at the lunar south pole." *Journal of Geophysical Research*106.E10 (2001): 23253-23266.

Nuding, D. L. *et al.* Deliquescence and efflorescence of calcium perchlorate: An investigation of stable aqueous solutions relevant to mars. *Icarus* 243, 420–428 (2014).

Nummedal, Dag, and David B. Prior. "Generation of Martian chaos and channels by debris flows." *Icarus* 45.1 (1981): 77-86.

Ojha, L. *et al.* Spectral constraints on the formation mechanism of recurring slope lineae. *Geophys Res Lett* **40**, 5621-5626 (2013).

Ojha, L. *et al.* HiRISE observations of Recurring Slope Lineae (RSL) during southern summer on Mars. *Icarus* 231, 365–376 (2014).

Ojha, L. et al. "TEMPORAL VARIATIONS OBSERVED IN SPECTRA OF ACTIVE FEATURES ON MARS." *2014 GSA Annual Meeting in Vancouver, British Columbia*. 2014.

Ojha, L. *et al.* Spectral evidence for hydrated salts in recurring slope lineae on Mars. (2015). doi:10.1038/NGEO2546

Paige, David A., Stephen E. Wood, and Ashwin Ft Vasavada. "The Thermal Stability of Water ice at the Poles of Mercury." *SCIENCE* 258 (1992): 23.

Parker, R. L. (1973). The Rapid Calculation of Potential Anomalies. *Geophysical Journal International*, *31*(4), 447–455. http://doi.org/10.1111/j.1365-246X.1973.tb06513.x

Pepin, Robert O. "On the origin and early evolution of terrestrial planet atmospheres and meteoritic volatiles." *Icarus* 92.1 (1991): 2-79.

Pestova O.N., Myund L.A., Khripun M.K., and Prigaro A.V. Polythermal study of the systems $M(ClO_4)_2$-H_2O (M^{2+} = Mg^{2+}, Ca^{2+}, Sr^{2+}, Ba^{2+}). *Russian Journal of Applied Chemistry* **78**, 409–413 (2005).

Phillips, R. J., & Saunders, R. S. (1975). The isostatic state of Martian topography. *Journal of Geophysical Research*, *80*(20), 2893–2898. http://doi.org/10.1029/JB080i020p02893

Pieri, David. "Distribution of small channels on the Martian surface." *Icarus*27.1 (1976): 25-50.

Platz, T., & Michael, G. (2011). Eruption history of the Elysium Volcanic Province, Mars. *Earth and Planetary Science Letters*, *312*(1-2), 140–151. http://doi.org/10.1016/j.epsl.2011.10.001

Pohorille, A. "Protocells as universal ancestors of living systems."*Protocells: bridging nonliving and living matter. MIT Press, Cambridge*(2008): 563-582.

Poulet, F., et al. "Phyllosilicates on Mars and implications for early Martian climate." *Nature* 438.7068 (2005): 623-627.

Prinn, R. G., and B. Fegley Jr. "Solar nebula chemistry: Origin of planetary, satellite, and cometary volatiles." *Origin and evolution of planetary and satellite atmospheres* (1989): 78-136.

Raymond, Sean N., Thomas Quinn, and Jonathan I. Lunine. "Making other earths: dynamical simulations of terrestrial planet formation and water delivery." *Icarus* 168.1 (2004): 1-17.

Rexer, M., & Hirt, C. (2015). Ultra-high-Degree Surface Spherical Harmonic Analysis Using the Gauss–Legendre and the Driscoll/Healy Quadrature Theorem and Application to Planetary Topography Models of Earth, Mars and Moon. *Surveys in Geophysics*, *36*(6), 803–830. http://doi.org/10.1007/s10712-015-9345-z

Robert, Francois. "The origin of water on Earth." *Science* 293.5532 (2001): 1056-1058.

Rummel J. D. *et al.* A New Analysis of Mars "Special Regions": Findings of the Second MEPAG Special Regions Science Analysis Group (SR-SAG2). *Astrobiology* **14**, 887-968 (2014).

Sagan, Carl, O. B. Toon, and P. J. Gierasch. "Climatic change on Mars."*Science* 181.4104 (1973): 1045-1049.

Sasselov, D. D., and M. Lecar. "On the snow line in dusty protoplanetary disks." *The Astrophysical Journal* 528.2 (2000): 995.

Schumm, S. A. "Structural origin of large Martian channels." *Icarus* 22.3 (1974): 371-384.

Scott, D. H., and J. M. Dohm. "Mars highland channels: An age reassessment." *Lunar and Planetary Science Conference*. Vol. 23. 1992.

Sjorgren, W. (1981). Mars: Hellas Planitia gravity analysis. *Icarus*, *45*(2), 331–338. http://doi.org/10.1016/0019-1035(81)90038-5

Slade, Martin A., Bryan J. Butler, and Duane O. Muhleman. "Mercury radar imaging: Evidence for polar ice." *Science* 258.5082 (1992): 635-640.

Smith, M. D. "The annual cycle of water vapor on Mars as observed by the Thermal Emission Spectrometer." *J. Geophys. Res* 107: 5115.

Sohl, F., & Spohn, T. (1997). The interior structure of Mars: Implications from SNC meteorites. *Journal of Geophysical Research*, *102*, 1613. http://doi.org/10.1029/96JE03419

Southam, G., F. Westall, and T. Spohn. "Geology, life and habitability."*Planets and Moons* 10 (2015): 473-486.

Squyres, S. W., et al. "In situ evidence for an ancient aqueous environment at Meridiani Planum, Mars." *Science* 306.5702 (2004): 1709-1714.

Squyres, Steven W., and James F. Kasting. "Early Mars: How warm and how wet?." *Science* 265.5173 (1994): 744-749.

Squyres, Steven W., and James F. Kasting. "Early Mars: How warm and how wet?." *Science* 265.5173 (1994): 744-749.

Stevenson, David J., Tilman Spohn, and Gerald Schubert. "Magnetism and thermal evolution of the terrestrial planets." *Icarus* 54.3 (1983): 466-489.

Tanaka, K. L., Robbins, S. J., Fortezzo, C. M., Skinner, J. A., & Hare, T. M. (2013). The digital global geologic map of Mars: Chronostratigraphic ages, topographic and crater morphologic characteristics, and updated resurfacing history. *Planetary and Space Science*. http://doi.org/10.1016/j.pss.2013.03.006

Taylor, G. J., Boynton, W. V., Br??ckner, J., W??nke, H., Dreibus, G., Kerry, K. E., … Drake, D. (2007). Bulk composition and early differentiation of Mars. *Journal of Geophysical Research E: Planets*, *112*(3). http://doi.org/10.1029/2005JE002645

Taylor, S. R., & McLennan, S. (2009). *Planetary crusts: their composition, origin and evolution* (Vol. 10). Cambridge University Press.

Urey HC (1967). “Water on the Moon.” *Nature* 216: 1094.

Valley, J. W., et al. "4.4 billion years of crustal maturation: oxygen isotope ratios of magmatic zircon." *Contributions to Mineralogy and Petrology* 150.6 (2005): 561-580.

Valley, John W., et al. "A cool early Earth." *Geology* 30.4 (2002): 351-354.

Vaniman, D. T., et al. "Mineralogy of a mudstone at Yellowknife Bay, Gale crater, Mars." *Science* 343.6169 (2014): 1243480.

Viola, D., McEwen, A. S., Dundas, C. M. & Byrne, S. Expanded secondary craters in the Arcadia Planitia region, Mars: Evidence for tens of Myr-old shallow subsurface ice. *Icarus* 248, 190–204 (2015).

Werner, S. C. (2009). The global martian volcanic evolutionary history. *Icarus*, *201*(1), 44–68. http://doi.org/10.1016/j.icarus.2008.12.019

Wieczorek, M. (2011). Shtools: Tools for working with spherical harmonics. *Astrophysics Source Code Library*, *1*, 10004.

Wieczorek, M. A., & Phillips, R. J. (1998). Potential anomalies on a sphere: Applications to the thickness of the lunar crust. *Journal of Geophysical Research*, *103*(E1), 1715–1724. http://doi.org/10.1029/97JE03136

Wieczorek, M., Meschede, M., & Oshchepkov, I. (2015, July). SHTOOLS: Version 3.1. http://doi.org/10.5281/zenodo.20920

Wilde, Simon A., et al. "Evidence from detrital zircons for the existence of continental crust and oceans on the Earth 4.4 Gyr ago." *Nature* 409.6817 (2001): 175-178.

Wilhelms, D., & Squyres, S. (1984). The martion hemispheric dichotomy may be due to a giant impact. *Nature*, *309*, 138–140. http://doi.org/10.1038/309138a0

Williams, Q. "Water, the solid Earth, and the atmosphere: the genesis and effects of a wet surface on a mostly dry planet." *Treatise on Geophysics* 9 (2010): 121-144.

Wise, D. U., Golombek, M. P., & McGill, G. E. (1979). Tharsis province of Mars: Geologic sequence, geometry, and a deformation mechanism. *Icarus*, *38*(3), 456–472. http://doi.org/10.1016/0019-1035(79)90200-8

Wray, J. J., et al. "Columbus crater and other possible groundwater-fed paleolakes of Terra Sirenum, Mars." *Journal of Geophysical Research: Planets* 116.E1 (2011).

Wray, James J., et al. "Diverse aqueous environments on ancient Mars revealed in the southern highlands." *Geology* 37.11 (2009): 1043-1046.

Wray, James J., et al. "Identification of the Ca-sulfate bassanite in Mawrth Vallis, Mars." *Icarus* 209.2 (2010): 416-421.

Yuan, D.-N., Sjogren, W. L., Konopliv, A. S., & Kucinskas, A. B. (2001). Gravity field of Mars: A 75th Degree and Order Model. *Journal of Geophysical Research: Planets*, *106*(E10), 23377–23401. http://doi.org/10.1029/2000JE001302

Yung, Y. L., and J. P. Pinto. "Primitive atmosphere and implications for the formation of channels on Mars." *Nature* 273.5665 (1978): 730-732.

Zahnle, Kevin, James F. Kasting, and James B. Pollack. "Mass fractionation of noble gases in diffusion-limited hydrodynamic hydrogen escape." *Icarus*84.2 (1990): 502-527.

Zent, A. P. "An open, snow-based, hydrologic system as an analog for Noachian Mars." *Lunar and Planetary Science Conference*. Vol. 30. 1999.

Zent, A. P. *et al.* Initial results from the thermal and electrical conductivity probe (TECP) on Phoenix. *J. Geophys. Res.* 115, 1–23 (2010).

Zhong, S., & Zuber, M. T. (2001). Degree-1 mantle convection and the crustal dichotomy on Mars. *Earth and Planetary Science Letters*, *189*(1-2), 75–84. http://doi.org/10.1016/S0012-821X(01)00345-4

Zuber, M. T., & Smith, D. E. (1997). Mars without Tharsis. In *Lunar and Planetary Science Conference* (p. 1583).

Zuber, M. T., Solomon, S. C., Phillips, R. J., Smith, D. E., Tyler, G. L., Aharonson, O., Zhong, S. (2000). Internal structure and early thermal evolution of Mars from Mars Global Surveyor topography and gravity. *Science (New York, N.Y.)*, *287*(5459), 1788–1793. http://doi.org/10.1126/science.287.5459.1788